PRECLINICAL DEVELOPMENT OF GENETIC NORMALIZATION STRATEGIES TO TREAT PITT-HOPKINS SYNDROME

Hyojin Kim

A thesis submitted to the faculty at the University of North Carolina at Chapel Hill in Partial fulfillment of the requirements for the degree of Doctor of Philosophy in the Neuroscience Curriculum in the School of Medicine.

Chapel Hill
2021

Approved by:

Benjamin Philpot

Paul Manis

Serena Dudek

Flavio Fröhlich

Hiroyuki Kato

ABSTRACT

Hyojin Kim: Preclinical Development of Genetic Normalization Strategies to Treat Pitt-Hopkins Syndrome
(Under the direction of Dr. Benjamin Philpot)

Neurodevelopmental disorders (NDDs) are defined as a group of conditions with onset in the developmental period, including intellectual or language impairments, attention-deficit disorders, and autism spectrum disorder. The United States' National Health Interview Survey has shown that 1 in 6 children have a developmental disability. The current guidelines for NDDs recommend undergoing an evaluation for genetic etiology and receiving general developmental interventions. Despite no approved treatments for NDDs, development of precision treatment strategies for NDDs has been on the rise.

Pitt-Hopkins syndrome (PTHS) is a rare neurodevelopmental disorder caused by monoallelic mutations or deletions of *Transcription Factor 4* (*TCF4*). A decade of basic research has led to an increased understanding of TCF4, including genetic variants and functional roles in brain development. The development of PTHS mouse models has expanded knowledge in molecular and pathophysiological mechanisms underlying PTHS, underpinning the potential therapeutic opportunities to treat the disorder. However, effective therapeutic approaches for PTHS have not been developed yet. The absence of a validated preclinical pipeline has ultimately impeded successful therapeutic development. Here I propose a genetic normalization strategy to treat PTHS and experimentally demonstrate the feasibility of treating PTHS by normalizing *TCF4*

expression. Furthermore, I address the challenges faced in developing a rational preclinical pipeline by characterizing the cell type-specific distribution of TCF4 and identifying a feasible intervention window. The studies comprising this dissertation provide an important framework for future rational design of genetic normalization clinical treatments for PTHS.

To my parents, who taught me success comes to those who embrace challenge

ACKNOWLEDGEMENTS

Completing my Ph.D. journey would not be possible without a tremendous support from my advisor, Ben Philpot. He provided the best research environment, clear directions of my project, and an unforgettable experience in science through the MBL neural systems and behavior course. I wish to thank Ben for his willingness to have me as an undergraduate student, technician, and graduate student in his lab, allowing me to fulfill many science experiences over the years. I have no doubt that one of my best decisions of my scientific careers will be always joining Ben's lab. I also would like to thank current lab members: Matt Judson, Alain Burette, Hanna Vihma, Brittany Williams, Mason Riley, Siddhi Ozarkar, Nick Ringelberg, Luke James, Marie Rougie, Eric Gao, Noah Miller, Patrick Lang, Audrey Smith, Courtney Davis, and Adam Draper, as well as former lab members: Portia Kunz, Janet Berrios, Angie Mabb, Megumi Williamson, Hanji Han, Kelly Jones, Courtney Thaxton, Alex Kloth, Rebekah Nash, Ralf Schmid, Ellen Clark, Bram Kuijer, HM Lee, Kiran Bettadapur, Sajeth Dinakaran, Mike Sidorov, and Bin Gu. I would like to give a special thanks to Matt Judson, who provided his vast scientific knowledge and critical interpretation of my data, and Mason Riley, who provided feedback on this dissertation. In addition, I wish to thank my undergraduate student, Noah Berens, and rotation students, Madigan Lavery and Nicole Ochandarena, for their contributions to my project. I must thank my committee members, Paul Manis, Serena Dudek, Flavio Fröhlich, and Hiroyuki Kato. They always

provided expertise so that I can do the best experiments. I am so appreciative and thankful to have such a supportive and constructive committee.

I wish to thank my family, and in particular, my parents, who always let me pursue my dream. They were supportive of my many years spent being a student in the U.S. Lastly, I am always appreciative for my husband, Bill Yeung, who witnessed my joy, struggles, and frustration since day one of the graduate school. I am so grateful that Bill was with me every step of the way and looking forward to the next chapter of my life with him.

TABLE OF CONTENTS

LIST OF TABLES

LIST OF FIGURES

LIST OF ABBREVIATIONS

AAV, Adeno-associated virus

AD, Activation domains

ASCL1, Achaete-scute complex homolog 1

ASO, Antisense oligonucleotides

ATOH1, Atonal homolog 1

BBB, Blood-brain barrier

bHLH, Basic helix-loop-helix

Bmp7, Bone morphogenetic protein 7

CE, Conserved element

ChAT, Choline acetyltransferase

ChIP-seq, Chromatin immunoprecipitation sequencing

CNS, Central nervous system

E-box, Ephrussi box

EEG, Electroencephalography

HDAC, Histone deacetylase

hiPSC, Human induced pluripotent stem cell

hSyn, Human synapsin promoter

ICV, Intracerebroventricular delivery

ID, Intellectual disability

IPa, Intraparenchymal delivery

ISH, *in situ* hybridization

IT, Intrathecal delivery

ITRs, Inverted terminal repeats

IV, Intravenous delivery

IZ, Intermediate zone

LFP, Local field potential

LTP, Long-term potentiation

NEUROD1, Neurogenic differentiation factor 1

NLS, Nuclear localization signal

NMDAR, N-Methyl-D-aspartic acid receptor

NPCs, Neuronal progenitor cells

NSCs, Neural stem cells

NT, Neurotypical

P, Postnatal day

P2A, Porcine teschovirus-1 2A

PTHS, Pitt-Hopkins syndrome

PV, Parvalbumin

REP, Repression domain

scAAV, Self-complementary AAV

SOM, Somatostatin

ssAAV. Single-stranded AAV

SVZ, Subventricular zone

SZ, Schizophrenia

TCF4, Transcription factor 4

VIP, Vasoactive intestinal peptide

Vg, Vector genomes

VZ, Ventricular zone

CHAPTER 1: TRANSCRIPTION FACTOR 4 IN NEURAL DEVELOPMENT AND ITS ASSOCIATION WITH PITT-HOPKINS SYNDROME

1.1 Introduction

Neurogenesis from embryonic brain throughout adulthood is promoted by a well-regulated interaction of cues and secreted signals that guide the development of neural stem cells (NSCs). For NSCs to transition into properly functioning neurons, they must go through complex processes to proliferate, differentiate, migrate, and integrate properly. Each step is guided by the timely activation of transcription factors that promote the transcription of the genes that define the specialization and maturation of a particular cell (1-3). Basic-Helix-Loop-Helix (bHLH) family members of transcription factors are essential regulators of each step, ensuring that appropriate numbers of specific neuronal and glial cell types are produced. bHLH transcription factors are named after their major protein structure, the bHLH domain, which is responsible for DNA binding. They are grouped into different classes based on the types of dimers they form, their patterns of expression and their specificity of DNA binding (4, 5). Transcription factor 4 (TCF4) is a member of the class I bHLH group that binds as homodimers or heterodimers with some bHLH transcription factors (6). *TCF4* gene expression is detected during embryonic development and found in different embryonic tissues, including the brain, gut, kidney, lung, and stomach, with the highest expression level detected in the brain (7, 8).

TCF4 gene dosage regulation is extremely important, as disease can arise from either too much or too little TCF4 expression. Monoallelic mutations and deletions of *TCF4* that result in haploinsufficiency can cause a neurodevelopmental disorder and non-syndromic intellectual disability (9-13). *TCF4* noncoding polymorphisms that result in overexpression appear to be linked with schizophrenia (SZ) (14-17). Moreover, *TCF4* is identified as a risk gene for bipolar disorder, post-traumatic stress disorder, and major depressive disorder (17, 18). The association of TCF4 with brain disorders implicates TCF4 as a dosage-sensitive protein which subtle dosage alterations are detrimental to brain development and function.

Pitt-Hopkins syndrome (PTHS) is a severe neurodevelopmental disorder caused by a pathogenic variant of the *TCF4* gene (9). Clinical features of PTHS include intellectual disability, lack of speech, severe motor impairment, sleep disorder, seizures, and high autism comorbidity (19). PTHS individuals need lifelong care because of the severity of their deficits, leading to an immense burden on the family, yet none of the available medications is effective to treat this disorder. Although there is no cure for PTHS, studies are underway to understand pathophysiology underlying PTHS and develop therapeutic interventions directed at the underlying molecular abnormality. Here I provide a comprehensive review of the *TCF4* gene and its protein product and function at the cellular level, as well as the description of pathophysiological mechanism associated with TCF4. Finally, I propose a novel therapeutic strategy that has the potential to treat PTHS.

1.2 Transcription factor 4

1.2.1 TCF4 gene structure and protein domains

The human *TCF4* gene is located on chromosome 18, spanning approximately 442 kb in chromosomal region 18q21.1, harboring 41 exons, of which 21 are alternative 5' exons (**Fig. 1.1**). The usage of alternative transcription start sites and splicing of internal exons produce protein isoforms with at least 18 distinct N'-termini (20). The bHLH domain is a highly conserved motif, consisting of a region of basic amino acids, followed by two amphipathic α-helices connected by a loop (**Fig. 1.1**). The basic region directly binds to Ephrussi box (E-box) with the core sequence of 5'-CANNTG-3' located in regulatory regions, while α-helices provide a dimerization interface (5). TCF4 can form homo-dimers or hetero-dimers with other bHLH proteins such as proneural proteins ASCL1 (achaete-scute complex homolog 1), ATOH1 (atonal homolog 1), and NEUROD1 (neurogenic differentiation factor 1) (8, 21, 22). TCF4 is ubiquitously distributed in different tissues, thus its functions depend on those dimerization partners that have a spatio-temporally restricted expression profile. Besides the bHLH domain, other domains are responsible for transcriptional regulation. Two conserved activation domains (AD1 and AD2) can modulate transcription through binding with co-activators or co-repressor. Conserved element (CE) represses AD1 activity, and repression domain (REP) represses the activity of AD1 or AD2. CE and REP are important domains that regulate AD1-mediated transcriptional activation or repression. Besides the domains directly involved in transcriptional regulation, TCF4 contains a nuclear localization signal (NLS) that allows the protein to be transported into the nucleus (20) (**Fig. 1.1**). Subcellular localization of TCF4 varies across different isoforms. TCF4

isoforms containing NLS sequences are exclusively found in the nucleus, whereas the isoforms that do not contain NLS are present either in the nucleus or cytoplasm (20, 23). This observation suggests that *TCF4* transcripts can be transported to the nucleus by piggybacking their dimerization partners. All TCF4 isoform proteins contain the bHLH domain and at least, one AD. It is still largely unknown how TCF4 isoform proteins differ from one another in terms of transcriptional regulation.

1.2.2 TCF4 expression pattern

The *TCF4* expression pattern is described as ubiquitous, being detected from multiple organs throughout development (7). While expression levels vary between different organs, the CNS has been known to have the most abundant expression level. Within the CNS, human TCF4 protein is distributed in the prosencephalon and ventricular zone during fetal development, and its expression remains sustained in the adult forebrain and cerebellum (8, 20). Mouse *Tcf4* is prominently expressed in the neocortex and hippocampus during early development, as well as in adulthood (24-26). Besides the brain, TCF4 protein is found in oligodendrocyte lineage cells in embryonic (~E18.5) and postnatally developing spinal cord. However, TCF4 protein is no longer detected in the adult spinal cord (27). Several studies reveal that human *TCF4* and rodent *Tcf4* expression in the brain increase considerably during the perinatal period, before subsequently declining to basal levels that are sustained throughout adulthood (24, 28, 29).

1.2.3 Transcriptional regulation by TCF4

TCF4 dimerizes with bHLH proteins and then binds to an E-box sequence in the DNA to regulate transcription (8, 20, 23, 30). There are several factors that contribute to the binding affinity of TCF4 dimer. The binding of TCF4 dimer to specific enhancers depends on a composition of the dimer itself and E-box internal and flanking DNA sequences (5). In addition, binding with transcriptional co-factors contributes to binding affinity (31). Finally, direct interaction of the bHLH region with Ca^{2+}-dependent proteins such as calmodulin and S100 regulates TCF4 protein binding specificity (32). In light of these factors contributing to the binding affinity of TCF4, several studies have revealed TCF4-regulated genes and networks. A recent chromatin immunoprecipitation sequencing (ChIP-seq) experiment conducted on SH-SY5Y neuroblastoma cells identified 10604 TCF4 binding sites that corresponded to 5437 genes. These genomic targets of TCF4 clustered into several signaling pathways that are involved in cation channel function, neurogenesis, and signal transduction (33). Another ChIP-seq experiment on neural-derived cells revealed 11322 TCF4 binding sites for 6528 candidate target genes, and these target genes were enriched in signaling pathways that contribute to axon/neuronal development and insulin signaling pathway (34). Microarray analyses after *TCF4* knockdown in SH-SY5Y neuroblastoma cells uncovered alterations in the pathways associated with transforming growth factor-beta signaling, epithelial to mesenchymal transition, apoptosis, and neuronal differentiation (35). Other similar knockdown experiments conducted in neural progenitor cells derived from human fetal brain cells revealed expression changes in the genes corresponding to cell differentiation and cell cycles (36, 37). The RNA sequencing experiment in

human induced pluripotent stem cell (hiPSC)-derived progenitor cells and glutamatergic neurons with reduced *TCF4* expression revealed a large set of differentially expressed genes. The top gene expression changes converged on focal adhesion, axon guidance, neurogenesis, and attractive and repulsive receptors, which guide neuronal growth and axon targeting (38). Although microarray and RNA sequencing experiments alone do not indicate direct TCF4 target genes, they highlight the roles of TCF4 in neurogenesis and provide a large-scale picture of the gene networks potentially influenced by TCF4.

1.3 TCF4 function

1.3.1 Roles of TCF4 in cortical development

During cortical development, projection neurons are generated in the proliferative ventricular zone (VZ) and the subventricular zone (SVZ) of the embryonic telencephalon (3). After cell division, these neurons migrate along radial glia fibers through the intermediate zone (IZ) to the cortical plate. Subsequently, properly positioned neurons undergo differentiation and synapse formation (39, 40). A number of studies have reported disruption in these processes of cortical development from the mice with TCF4 loss-of-function. Abnormal migration was first described from *Tcf4* knockdown mice in 2016. This study found accumulation of neurons in the IZ due to delayed migration. Interestingly, disrupted migration was rescued by downregulating *Bone morphogenetic protein 7* (*Bmp7*), suggesting that *Bmp7* might be a downstream target of TCF4, which is important for neuronal migration (24). In another study, increased number of progenitor cells was found in the VZ/SVZ of the TCF4 deficient embryonic brain, which resulted in delayed migration and impaired laminar formation in the neonatal cortex

(41). Conversely, increasing levels of *Tcf4* expression in the developing forebrain enhanced the rate of migration and resulted in aggregation of pyramidal neurons in L2/3 of the PFC, a finding that might be significant in the context of the causality between *TCF4* polymorphisms and SZ (42). Besides migration, cortical neurons displayed abnormally short dendrites and decreased density of synapses in heterozygous deletion of *Tcf4* (41). TCF4 loss-of-function also reduced the number of dendritic spines in the cortex (43). These previous studies support an important role of TCF4 during cortical development.

1.3.2 Roles of TCF4 beyond cortical development

During dentate gyrus development, radially migrating neuronal progenitor cells (NPCs) form a migratory stream from the neuroepithelium toward the hilus, where they are reorganized to build the subgranular zone. *Tcf4* knockout disturbed migration of NPCs, as these cells were stuck in the dentate migratory stream at postnatal day (P) 0, instead of migrating to the hilus. As a result of disrupted subgranular zone formation, the size of the dentate gyrus was dramatically reduced. Interestingly, this study showed that impairing migration could be due to reduced expression of *Wnt7b*, a TCF4 target responsible for neurite development (44).

The role of TCF4 in the developing brain is not restricted to the telencephalon. TCF4 dimerization with MATH1 (also called ATOH1) has been shown to be critical for normal pontine nuclei development. The absence of TCF4/MATH1 dimers failed to activate differentiation of the pontine neurons (22). Interestingly, such abnormal differentiation has been only detected in pontine nuclei, even though *Tcf4* and *Math1*

are both expressed throughout the rhombic lip. Taken together, these findings suggest that TCF4 has specialized roles during neurogenesis throughout the developing brain.

1.4 Aberrant functions of TCF4 in disease

1.4.1 Pitt-Hopkins syndrome

The developmental trajectory in patients with PTHS is slower than healthy neurotypical children and adolescents. Neurobehavioral features of PTHS include delay in motor function, lack of speech, stereotypies, sleep disorder, seizures, anxiety, and intellectual disability. Other commonly reported features include constipation and hyperventilation (19). Many PTHS individuals meet clinical diagnostic criteria for autism (45). MRI studies revealed brain structural changes, including bulging of caudate nuclei, ventricular asymmetry, hypoplasia of the corpus callosum, and atrophy of the frontal and parietal cortex (19, 46). The prevalence of PTHS suggests a population frequency of 1:34,000 to 1:41,000 (19).

PTHS is caused by monoallelic mutations or deletions of the *TCF4* gene. The subsequent findings delineate the TCF4 mutational spectrum among PTHS patients that consists of frameshift, missense, nonsense, splice-site, and stop mutations (8, 47). These PTHS-causing mutations can create hypomorphic, non-functional, and dominant-negative alleles (30, 48). Mutation and partial deletion of *TCF4* are found in the patients with non-syndromic intellectual disability as well (11, 12, 49). The divergent clinical phenotypes range from mild to severe intellectual disability with PTHS features, which depend on the impairment of different protein domains. For instance, mutations or deletions within AD2 or bHLH domain, thus affecting the functions of all isoforms, cause

typical PTHS. Mutations or deletions within AD1 or NLS domain, affecting a subset of isoforms, give rise to mild intellectual disability without a full spectrum of PTHS (50).

Current treatments for PTHS focus on symptomatic management of the disease. Amantadine, the noncompetitive NMDAR antagonist, has been used to treat anxiety and aggression (19). This is anecdotal information, and its effect has not been systematically evaluated yet. A short-term use of antipsychotics has been reported to have a positive effect on behavioral problems. Aripiprazole is a partial agonist of dopamine D2 and 5-HT_{1A} receptor and an antagonist of 5-HT_2 receptor, and risperidone is an antagonist of dopamine D2 receptor and 5-HT_2 receptor (51). Administering doses of these drugs provided positive effects on irritability, social withdrawal, hyperactivity, and stereotyped behavior (52). Valproate and acetazolamide have been used to reduce the frequency and severity of hyperventilation and apnea (19, 53).

1.4.2 Mouse models of PTHS

Several PTHS mouse models, carrying distinct types of *Tcf4* mutation or deletion in heterozygosity, exhibit abnormal cognitive and behavioral deficits. Previously validated PTHS mouse models, including *Tcf4*$^{+/-}$ and *Actin-Cre::Tcf4*$^{flox/+}$ mice, harbor a deletion of the exon that encodes for the bHLH domain (54-56). Assessment of behavior in these mouse models showed that *Tcf4*$^{+/-}$ mice exhibited alterations in balance and motor coordination, preference for social isolation over interaction, spatial memory and learning deficits, hyperactivity, and repetitive behaviors shown by increased grooming. Communication deficits were also observed in the form of reduced ultrasonic vocalizations from *Tcf4*$^{+/-}$ pups (54). *Actin-Cre::Tcf4*$^{flox/+}$ mice also exhibited

hyperactivity, abnormal learning and memory function, dysregulation in sensorimotor gating, and reduced anxiety-like behavior (56). The clinical study shows that approximately 60% of PTHS individuals have deletions of *TCF4*; the remaining 40% of individuals with PTHS have point mutations (47). Such mutations could perturb not only the function of wildtype TCF4, but other bHLH transcription factors by disturbing formation of dimers. Therefore, the therapeutic effects on loss-of-function mutations may not be identical to the effects on dominant-negative mutations. In order to strengthen the confidence in the therapeutic potential of a new mechanism of action, *Tcf4*$^{R579W/+}$ and *Tcf4*$^{\Delta 574\text{-}579}$ mice were generated. *Tcf4*$^{R579W/+}$ mimics the most common pathogenic *TCF4* point mutation, and *Tcf4*$^{\Delta 574\text{-}579}$ has a small in-frame deletion. The R579W and Δ574-579 mutations produce TCF4 variants that act in a dominant-negative fashion. *Tcf4*$^{R579W/+}$ and *Tcf4*$^{\Delta 574\text{-}579}$ mice exhibited hyperactivity, abnormal learning function, dysregulation in sensorimotor gating, and reduced anxiety-like behavior, which are similar to those aforementioned for the *Actin-Cre::Tcf4*$^{flox/+}$ mice. These data suggest that convergent neurobiological features in PTHS mouse models and providing a foundation for potential treatments to be validated (56).

1.4.3 Molecular pathophysiology mechanisms

Basic research on the function of TCF4 has led to the characterization of molecular mechanisms that may underlie PTHS. *Tcf4* haploinsufficiency enhanced hippocampal long-term potentiation (LTP) (54, 56). Hippocampal LTP can be induced by high frequency stimulation that drives rapid influx of Ca^{2+}. Therefore, LTP enhancement shown in PTHS model mice was possibly mediated through NMDA

receptor (NMDAR) signaling pathway (57). Indeed, NMDAR-mediated current was increased in *Tcf4* haploinsufficient mice, suggesting enhanced NMDAR-mediated LTP (56). There is a complex association between LTP and cognitive performance, as evidenced by other studies showing that LTP enhancement is accompanied by learning and memory deficits in mouse models with genetic alterations in *Psd95*, *Limk1*, and *Fmr2* (58-60). Given that PTHS model mice exhibit hippocampal-dependent memory and learning deficits (56), these findings suggest that *Tcf4* disruption may broadly perturb the molecular mechanisms underlying LTP induction, which negatively affects cognitive function. Although the mechanistic insight needs to be further validated, restoring normal synaptic plasticity by modulating NMDAR function could provide a therapeutic opportunity for PTHS.

Tcf4 knockdown altered intrinsic neuronal excitability of excitatory neurons in the medial prefrontal cortex (28). Intrinsic excitability is regulated by modifying the expression, localization, or biophysical properties of voltage- and calcium-gated ion channels. Evidence shows that expression levels of *sodium voltage-gated channel alpha subunit 10a* (*Scn10a*) and *potassium voltage-gated channel subfamily Q member 1* (*Kcnq1*) were upregulated in mice with *Tcf4* haploinsufficiency (28). Therefore, overexpression of those voltage-gated channels might have altered intrinsic excitability. Indeed, this study showed that blocking SCN10a in *Tcf4* heterozygous cells was effective at rescuing action potential output (28), suggesting that correcting the function of sodium voltage-gated channels could be another potential therapeutic target for PTHS.

1.5 Discussion

TCF4 is ubiquitously distributed across the CNS and regulates hundreds to thousands of genes that are involved in a number of signaling pathways that are crucial for brain development. Loss of TCF4 function causes PTHS, which is a lifelong disease that affects multiple organ systems and results in functional limitations and high health care need. While there is no effective treatment for PTHS, the knowledge of the genetic and molecular disruptions resulting from *TCF4* haploinsufficiency shed light on developing novel therapeutic opportunities for PTHS. In the past years, multiple therapeutic approaches have been preclinically tested on PTHS model mice. The first approach was to broadly modify transcriptional levels. Histone deacetylase (HDAC) inhibitors are compounds that inhibit histone deacetylases and have a long history of use to improve memory and learning function (61). Administering SAHA, a HDAC inhibitor, improved learning function and memory in adult PTHS model mice, suggesting a potential for HDAC inhibitors as therapeutics for improving cognition and memory recall in PTHS (54). However, efforts to modify transcription using HDAC inhibitors are inherently broad, and because of their diffuse focus, such therapeutic outcomes are likely to provide only modest recovery at the cost of substantial toxicity arising from off-target transcriptional effects (62). The second approach was to target sodium voltage-gated channel, specifically NaV1.8 (encoded by *SCN10a*). Orally dosing Nicardipine, shown to inhibit $Na_V1.8$, improved social behavior, innate and repetitive behavior, memory, and activity level in PTHS model mice (63), supporting Nicardipine as the therapeutic potential to treat PTHS. However, whether a long-term use of the drug is safe for the patient's life needs to be validated.

While present therapeutic approaches may not provide satisfactory therapeutic outcomes due to their off-target effects and inability for long-term usage, the genetic biology of PTHS suggests a novel therapeutic opportunity; loss-of-function in one *TCF4* copy is sufficient to cause PTHS in humans, so conversely, restoring TCF4 function could treat PTHS. Convergent lines of evidence support the idea that the disorder can be treated, at least to a degree, throughout life. First, studies in animal models of other single-gene neurodevelopmental disorders, including Rett syndrome and Angelman syndrome (AS), showed that normalizing the expression of the disease-causing gene in postnatal life can provide therapeutic benefits (64, 65), raising the possibility that the same might be true for PTHS. While synaptic defects have been observed in mouse models of PTHS, there is no evidence for disease-related neurodegeneration in PTHS individuals or mouse models (28, 56), further supporting the possibility that the observed synaptic defects might be reversible. In support of this idea, upregulating *Tcf4* expression has been shown to partially rescue learning function and memory in adult PTHS model mice (54). Collectively, these observations indicate that PTHS can be treated with genetic normalization approaches to upregulate *TCF4* expression to compensate for loss-of-function of TCF4 (**Fig. 1.2**). Several approaches to normalize protein concentration have been clinically validated. Antisense oligonucleotides (ASOs) are 15-30 nucleotides in length that can selectively hybridize with RNA sequences to reduce, restore, or modify protein expression. A recently developed ASO to treat spinal muscular atrophy binds to the *survival motor neuron 2* (*SMN2*) pre-mRNA and alters its splicing to allow the inclusion of exon 7 in mRNA, therefore increasing the expression of a stable SMN protein (66). This ASO treatment has been shown to improve motor

function in affected children. Adeno-associated virus (AAV)-mediated gene therapy is another potential therapeutic intervention by targeting the root cause of single-gene disorder to address loss-of-function and gain-of-function mutations (67, 68). An AAV-based gene therapy, designed to deliver a functional copy of the human *SMN* gene, is available for patients with spinal muscular atrophy, which is the first gene therapy to be approved by the US Food and Drug Administration (69).

AAV-mediated gene therapy has several advantages over pharmacological interventions and ASOs. AAV vectors transduce in nondividing cells and can confer a long-term stable gene expression without associated inflammatory toxicity (70). This ‘one-and-done’ approach is attractive as a therapeutic intervention, particularly with PTHS that may require permanent correction of diseased state. Also, AAV-mediated gene therapy can target discrete cell types by promoter choice, providing a capacity to adjust *Tcf4* expression in a cell-type specific manner (68). Lastly, the gene therapy approach requires little understanding of the gene function, as it directly targets the root cause of the disorder. In principle, disorders linked to the loss of TCF4 function such as PTHS should be amenable to correction following treatment with viral vectors coding for TCF4. Accordingly, I performed a proof-of-concept experiment to test the feasibility of AAV-mediated gene therapy to treat PTHS. The goal of the study is to determine whether augmenting TCF4 function can provide a viable therapeutic intervention for PTHS.

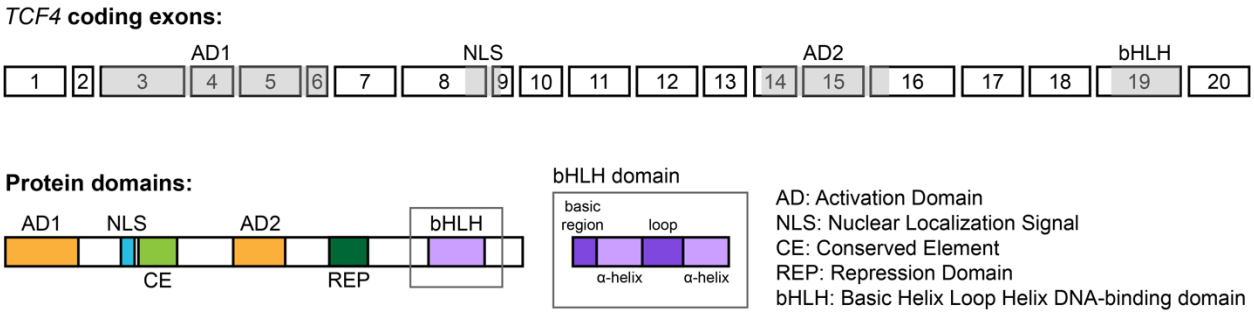

Figure 1. 1: Schematic representation of the TCF4 genomic organization with coding exons (exon 1-20) and TCF4 protein domain structure.

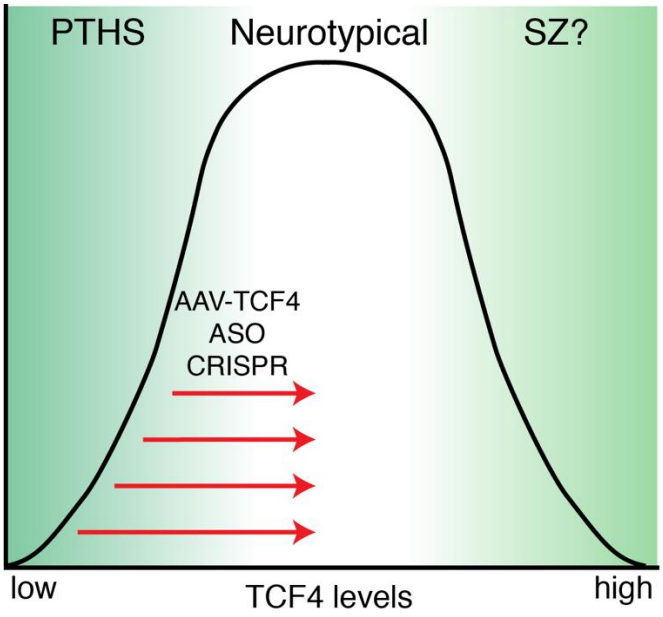

Figure 1. 2: Schematic depicting the genetic normalization strategy to treat PTHS. *TCF4* haploinsufficiency causes PTHS and non-syndromic intellectual disability (ID). NT = Neurotypical. *TCF4* overexpression appears to be linked to Schizophrenia (SZ). The genetic normalization strategy is boosting TCF4 protein to its normal level through gene therapy (AAV-TCF4), ASOs, and CRISPR approaches.

CHAPTER 2: A PROOF-OF-CONCEPT STUDY TO TEST THE FEASIBILITY OF TREATING PTHS WITH THE AAV-MEDIATED GENE THERAPY APPROACH

2.1 Introduction

Recent innovations in vector design and administration route allow neurodevelopmental disorders to become amenable to gene therapy approaches (71). Recombinant AAV can package any DNA cassette up to ~4.8 kb. The use of self-complementary (sc) AAV genomes provides faster gene expression and a 10- to 100-fold increase in transduction efficiency compared to single-stranded (ss) AAV (72). Different promoter choices provide options for gene expression to be cell-specific or ubiquitous, and for controlling the overall amount of transcript produced. Recently developed engineered AAV capsids overcome the limitations of naturally occurring capsid to enhance CNS transduction (71, 73). Several administration options have been evaluated preclinically for biodistribution of AAV vectors to the CNS. Intraparenchymal delivery (IPa) allows the distribution of AAV directly to the brain region and neurons of interest. Intrathecal delivery (IT) is a validated route to target motor and sensory neurons of the dorsal root ganglia, and intracerebroventricular delivery (ICV) can broadly target the CNS (74). Intravenous delivery (IV) has greater potential in clinical settings than IPa, IT, and ICV routes because IV route can provide broad biodistribution in a non-invasive manner (74, 75). Taking advantage of advances in vector design and alternative routes of administration, the feasibility of the gene therapy approach has been evaluated in neurodevelopmental disorders with single-gene defects, primarily

using mouse models. For example, ICV injection of AAV9/FMRP in Fragile X syndrome model mice rescued the social symptoms, anxiety, and motor behavior phenotypes (76). In Rett syndrome model mice, achieving a safe level of *MeCP2* expression through AAV vector improved survival and neurological symptoms (77, 78). In AS, delivering AAV vectors encoding for *Ube3a* directly to the brain improved motor learning and innate behaviors and rendered resilient to electrogenesis in AS model mice (Philpot lab unpublished results). These studies indicate that AAV gene therapy provides a viable strategy to treat these disorders. PTHS is caused by *TCF4* deficiency. Therefore, PTHS symptoms might be improved by normalizing *TCF4* expression through AAV-mediated gene therapy, but this possibility has never been explored in PTHS model mice. A general assumption for PTHS is that the earlier the age of intervention, the greater the opportunity for therapeutic benefit. Accordingly, I tested the therapeutic benefit of AAV-mediated gene therapy in PTHS model mice treated at P1, as this age allows for effective gene delivery in at least 20-40% of neurons and represents the earliest postnatal opportunity for intervention. This proof-of-concept experiment can provide the first insight into whether the gene therapy approach represents potential PTHS therapeutic intervention.

2.2 Results

2.2.1 Development and validation of AAV vectors expressing *TCF4*

To examine whether delivering human *TCF4* through AAV vector is effective at reversing behavioral phenotypes in a mouse model of PTHS, I produced a C-terminus Myc-tagged and codon-optimized version of the human *TCF4* gene (hTCF4opt).

Multiple isoforms of *TCF4* are expressed due to alternative promoters and variable splicing. Isoform A (also known as TCF4B+) was chosen to be packaged into the viral vector because it is the full-length isoform containing all the functional domains. hTCF4opt was packaged into scAAV9 plasmids, with a synthetic JeT promoter to drive moderate levels of expression ubiquitously (AAV9-JeT-hTCF4opt-Myc, **Fig. 2.1A**). A similar construct driving GFP was produced as a control AAV (**Fig. 2.1A**). To evaluate biodistribution of *hTCF4*, I bilaterally delivered AAV9/hTCF4 to the cerebral ventricles of neonates and then examined Myc expression, as Myc protein represents AAV9/hTCF4 distribution (**Fig. 2.1B-C**). I detected Myc-expressing cells from the pyramidal cell layer of the hippocampus, indicating successful transduction of AAV9/hTCF4 following neonatal ICV injection (**Fig. 2.1D-E**). However, Myc signals appeared to be weak in the hippocampus and barely detectable in the cortex. It is possible that the Myc antibody may not be sensitive enough to detect protein. Alternatively, the overall amount of protein produced by the JeT promoter may be undetectable. To distinguish these possibilities, I performed neonatal ICV injection of AAV9/GFP, which is the control virus for AAV9/hTCF4, and evaluated GFP immunofluorescence. I detected strong GFP signals particularly in the dorsal hippocampus and more widespread distribution of GFP-expressing cells in the cortex (**Fig. 2.1F**). These data indicate that failure to immunodetect Myc protein in the mouse brain might be due to either the limited sensitivity of the Myc antibody or the rapid degradation of virally-delivered hTCF4 protein.

2.2.2 Early postnatal AAV-mediated *hTCF4* gene transfer failed to rescue behavioral phenotypes in PTHS model mice

To address whether restoring TCF4 function is sufficient to ameliorate PTHS-associated behavioral phenotypes, I analyzed the behavioral performance of adult PTHS model mice and their littermate controls that were ICV-injected as neonates with either AAV9/GFP (control) or AAV9/hTCF4 (**Fig. 2.2A**). *Tcf4*$^{flox/+}$ mice contain loxP sites flanking exon 18-20 of a *Tcf4* allele such that Cre recombinase-mediated excision of the loxP sites heterozygously removes the bHLH region of *Tcf4*. To generate PTHS model mice, I crossed *Tcf4*$^{flox/+}$ mice with β-Actin transgenic mice (*Actin-Cre::Tcf4*$^{flox/+}$), which mimics pan-cellular heterozygous disruption of *Tcf4*. Their littermate controls are *Tcf4*$^{flox/+}$ mice whose bHLH domain is intact. A previous study has already established a behavioral test battery suitable for preclinical testing in *Actin-Cre::Tcf4*$^{flox/+}$ mice (56).

To assess anxiety-like behavior, I evaluated the time mice spent in the open or closed arms of the elevated plus maze. I found that control virus-treated *Actin-Cre::Tcf4*$^{flox/+}$ mice spent similar time in the closed and open arms, suggesting abnormally reduced anxiety. In contrast, control mice proportionally spent more time in the closed arms. Treating AAV9/hTCF4 to *Actin-Cre::Tcf4*$^{flox/+}$ mice did not correct the abnormally reduced anxiety phenotype (**Fig. 2.2B**). I assessed locomotor and exploration activity by the open field test and found that *Actin-Cre::Tcf4*$^{flox/+}$ mice showed increased activity and total distance travelled. Similarly, *Actin-Cre::Tcf4*$^{flox/+}$ mice treated with AAV9/hTCF4 still exhibited hyperactivity in this assay (**Fig. 2.2C**). Sensorimotor gating is often impaired in neurodevelopmental disorders and can be assessed in mice by the auditory prepulse inhibition task. Accordingly, I measured

sensorimotor gating using an acoustic startle task. *Actin-Cre::Tcf4*$^{flox/+}$ mice displayed significant decrease of the startle amplitude at 120 dB compared to their controls, but treating with AAV9/hTCF4 did not normalize startle amplitude in *Actin-Cre::Tcf4*$^{flox/+}$ mice (**Fig. 2.2D**). To determine whether hippocampal-dependent learning deficits could be prevented, I measured performance in the Morris water maze task. *Actin-Cre::Tcf4*$^{flox/+}$ mice were able to locate the visual platform and had similar swim speeds during all phases of testing compared to their control littermates, suggesting that they had sufficient visual and motor skills to perform the task (**Fig. 2.2E-F**). However, *Actin-Cre::Tcf4*$^{flox/+}$ mice took a significantly longer time to locate the hidden platform than controls (**Fig. 2.2G**). During the reversal phase, in which the hidden platform is relocated to the opposite quadrant, *Actin-Cre::Tcf4*$^{flox/+}$ mice did not meet criterion (15 seconds) for learning over the 9-day testing period (**Fig. 2.2H**). Treating *Actin-Cre::Tcf4*$^{flox/+}$ mice with AAV9/hTCF4 did not show improvement in spatial and reversal learning performance (**Fig. 2.2G-H**).

2.3 Discussion

In theory, delivery of a wildtype copy of the *hTCF4* gene to cells lacking functional TCF4 protein represents a therapeutic approach worth considering. However, my work showed, at a “proof-of-concept” level, that injecting AAV9/hTCF4 into the *Tcf4*-null mouse brains did not correct abnormal behavioral phenotypes. My results could indicate that AAV-mediated genetic therapy is not effective in relieving PTHS-associated phenotypes in a mouse model. Alternatively, my results could implicate that I did not generate appropriate vector constructs for effective therapeutic outcomes. I

propose four complications that might have contributed to the inability to rescue behavioral functions with this initial gene therapy attempt. First, the amount of virally-delivered *hTCF4* might not be sufficient to achieve a threshold that provides therapeutic benefits. Second, delivering more than one *hTCF4* isoform might be required to normalize transcription. Third, delivering *hTCF4* to the cells in which TCF4 is not endogenously present might impair transcriptional machineries of those cells not normally expressing *Tcf4*. Lastly, a critical time window for reversing behavioral deficits might be established much earlier than early postnatal life. Thus, PTHS should be intervened earlier than the postnatal period.

Unfortunately, I realized that there were no sufficient information and experimental control to be able to address these four issues. First, TCF4 is a dosage-sensitive protein: too little expression causes neurodevelopmental disorders, and too much expression leads to schizophrenia. Therapeutic threshold that must be achieved by the AAV-mediated gene therapy is unclear. The TCF4 gene produces at least 18 isoforms, some of which may be required to be expressed in the brain during the specific developmental stage. However, it is unknown which *TCF4* isoforms are expressed in the human mouse brain. More importantly, I lack information of cell types that express *Tcf4*, knowledge essential to establishing the cell types that should be targeted by any *TCF4* normalization approaches. Finally, the treatment window when *TCF4* normalization can rescue phenotypes has never been defined for PTHS. Insufficient knowledge of the precise molecular actions of TCF4 and the optimal treatment window impedes the development of the genetic therapy. To fill the gap in knowledge, I generated a novel *Tcf4* reporter/conditional PTHS mouse model to

address the following questions: 1) Which cell types express TCF4?; 2) which cell types, when rendered fully functional, have the largest impact on rescuing behavioral phenotypes in PTHS mouse model?; and 3) when should *Tcf4* expression be normalized for phenotypic recovery? Although my work does not yet address the key *Tcf4* isoforms that are required for a full functional recovery of neurons, Dr. Timmusk, who first identified human *TCF4* isoforms, has been rigorously performing experiments to provide the knowledge of isoform choice. His preliminary data will be discussed later in this thesis. My basic science investigations will inform the rational design of genetic normalization approaches such as AAV-mediated gene therapy, ASOs, as well as other pharmacological drugs for PTHS.

2.4 Materials and Methods

AAV vector construction and production

A codon-optimized human TCF4 cDNA, hTCF4opt, was designed using a commercially available algorithm tool (Atum, Newark, CA). hTCF4opt encodes hTCF4 isoform B. The hTCF4opt cDNA was subcloned into plasmid JeT. JeT-hTCF4opt was packaged into AAV9 capsids, using methods developed by the UNC Gene Therapy Center Vector Core facility. Purified AAV9 was dialyzed in Phosphate-buffered saline (PBS) supplemented with 5% D-Sorbitol and an additional 212 mM NaCl (350 mM NaCl total). Vector titers were determined by qPCR.

AAV delivery

P1-2 mouse pups were cryo-anesthetized on ice for 3 minutes, then transferred to a chilled stage equipped with a fiber optic light source for transillumination of the lateral ventricles. A 10 μl syringe fitted with a 32-gauge, 0.4-inch-long sterile syringe needle (7803-04, Hamilton) was used to bilaterally deliver 0.5 μl of AAV9/JeT-hTCF4-myc or AAV9/JeT-GFP to the ventricles. The addition of Fast Green dye (1 mg/mL) to the virus solution visualized injection area. Following injection, pups were warmed on an isothermal heating pad with home-cage nesting material before being returned to the home cage.

Tissue preparation

Perfusion: Mice were anesthetized with sodium pentobarbital (60 mg/kg i.p.) before transcranial perfusion with 25 ml of PBS immediately followed by phosphate-buffered 4% paraformaldehyde (pH 7.4). Brains were postfixed overnight at 4°C before 24-hour incubations in PBS with 30% sucrose. Brains were sectioned coronally or sagittally at 40 μm using a freezing sliding microtome (Thermo Scientific). Sections were stored at -20°C in a cryo-preservative solution (45% phosphate-buffered saline or PBS, 30% ethylene glycol, and 25% glycerol by volume).

Immunohistochemistry

Sections were rinsed several times with PBS (pH = 7.3) and PBS containing 0.2% Triton X-100 (PBST) before blocking with 5% normal goat serum in PBST (NGST) for 1 hour at room temperature. Sections were then incubated with primary antibodies

diluted in NGST at 4°C for 48 hours. Sections were rinsed several times with PBST and then incubated with secondary antibodies for 1 hour at room temperature. In all experiments, 4',6-diamidino-2-phenylindole (DAPI; Invitrogen D1306) was added during the secondary antibody incubation at a concentration of 700 ng/ml. Primary antibodies used included 1:1000 Myc (ab9106), 1:1000 rabbit anti-GFP (NB600-308), and 1:1000 guinea pig anti-NeuN (ABN90P). The following secondary antibodies from Invitrogen (Carlsbad, CA) were used at 1:1000 dilution: goat anti-mouse Alexa 647 (A21240), goat anti-rabbit Alexa 488 (A32731), goat anti-guinea pig Alexa 594 (A11076).

Imaging and figure production

Images of brain sections stained by using fluorophore-conjugated secondary antibodies were obtained with Zeiss LSM 710 Confocal Microscope, equipped with ZEN imaging software (Zeiss, Jena, Germany). Images compared within the same figures were taken within the same imaging session using identical imaging parameters. Images within figure panels went through identical modification for brightness and contrast by using Fiji Image J software.

Behavioral testing and analyses

All behavioral testing was performed through the UNC Mouse Phenotyping Core. Testing began when animals were between 10 and 12 weeks of age and ended when they were between 18 and 20 weeks of age.

Elevated plus maze. The elevated plus maze is constructed to have two open arms and two closed arms, all 20 cm in length; the height in the closed arms is 30 cm. The entire

maze is elevated 50 cm above the floor. Mice were given 5 min trial on the elevated plus maze. For testing, the mice were placed on the center section (8 x 8 cm) and allowed to explore the maze freely. Time and the number of entries into the open and closed arms were recorded.

Open field test. The mice were given a 60 min trial in an open-field chamber (41 x 41 x 30 cm) that was crossed by a grid of photobeams (VersaMax system; AccuScan Instruments). Counts were taken of the number of photobeams broken during the 60 min trial in 5 min intervals. Measures included locomotor activity (total distance traveled).

Acoustic startle. Mice were placed into individual small Plexiglas cylinders within larger, sound-attenuating chambers (San Diego Instruments SR-Lab system). Each cylinder was seated upon a piezoelectric transducer that quantified the vibrations. The chambers include a ceiling light, a fan, and a loudspeaker for the acoustic stimuli. Background sound levels (70 dB) and calibration of the acoustic stimuli was confirmed with a digital sound level meter (San Diego Instruments). Each session began with a 5 min habituation period, followed by 42 trials (seven of each type): nostimulus trials, acoustic startle stimulus alone (120 dB for 40 ms) trials, and prepulse stimulus (20 ms; 74, 78, and 82 dB) trials that occurred 100 ms before the onset of the acoustic startle stimulus. Measures were taken of the startle amplitude for each trial across a 65 ms sampling window. An overall analysis was performed for each subject's data for levels of prepulse inhibition at each prepulse sound level, calculated as 100 - [(response amplitude for prepulse stimulus and startle stimulus together/response amplitude for startle stimulus alone) x 100].

Morris water maze. The water maze consisted of a circular pool (diameter, 122 cm) partially filled with water (45 cm deep, 24 –26°C) located in a room with numerous visual cues. The procedure involved three different phases: (1) a visible platform test, (2) acquisition in the hidden platform task, and (3) a test for reversal learning. For the visible platform test, each mouse was given 4 trials/d for 2 d to swim to an escape platform cued by a patterned cylinder extending above the surface of the water. For each trial, the mouse was placed in the pool at one of four possible locations (randomly ordered) and then given 60 s to find the visible platform. If the mouse found the platform, the trial ended, and the animal was allowed to remain for 10 s on the platform before the next trial began. Measures were taken of latency to find the platform and swimming speed via an automated tracking system (Ethovision; Noldus). After the visible platform task, mice were tested for their ability to find a submerged, hidden escape platform (diameter, 12 cm). Each animal was given 4 trials per day with 1 min per trial to swim to the hidden platform. The criterion for learning was an average group latency of 15 s or less to locate the platform. Mice were tested until the group reached criterion, with a maximum of 9 d of testing. After the acquisition phase, mice were tested for reversal learning using the same procedure described above. In this phase, the hidden platform was relocated to the opposite quadrant in the pool. Measures were taken of latency to find the platform.

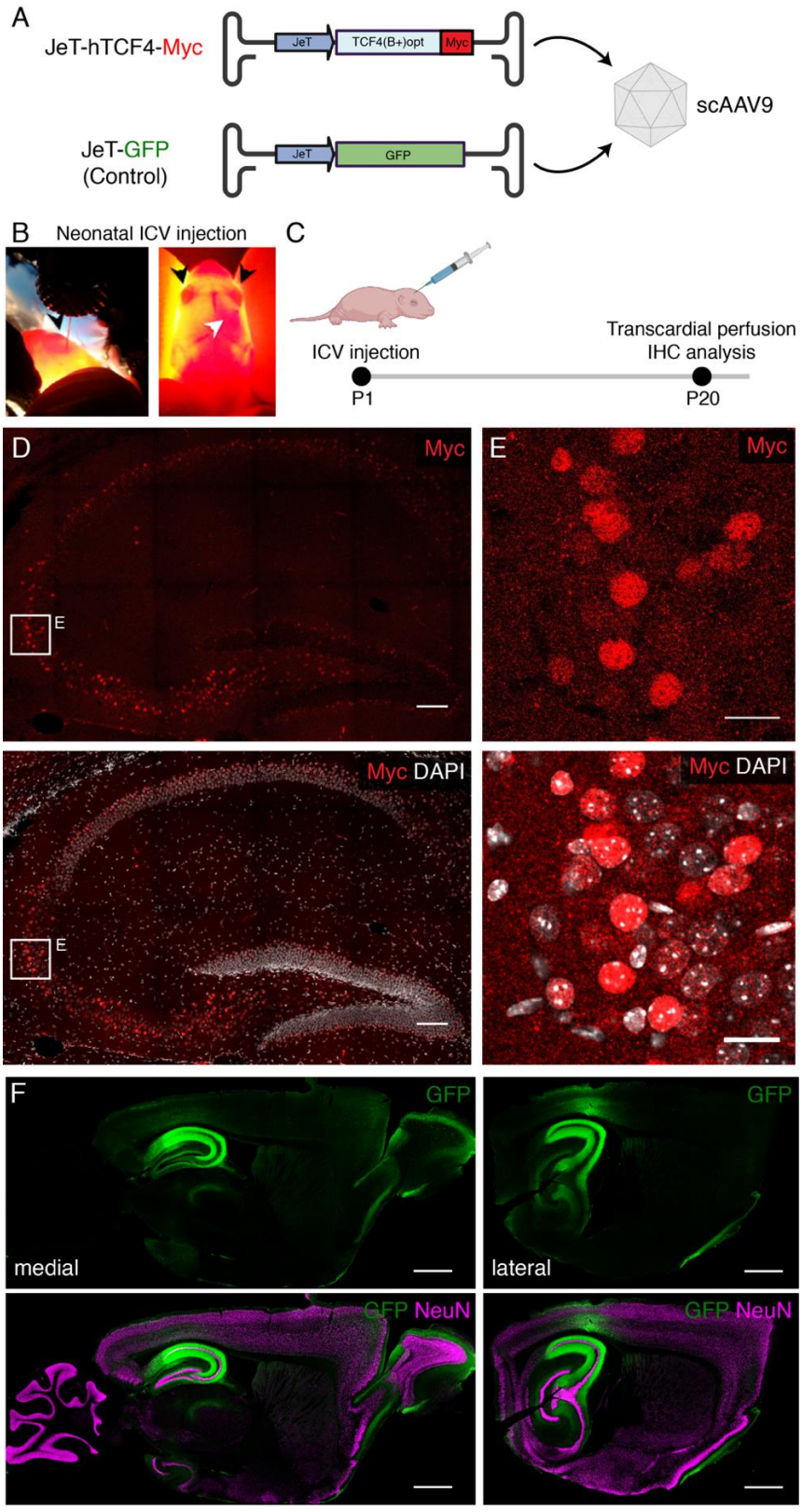
A
JeT-hTCF4-Myc
JeT
TCF4(B+)opt
Myc
scAAV9
JeT-GFP
(Control)
JeT
GFP
B
Neonatal ICV injection
C
ICV injection
Transcardial perfusion
IHC analysis
P1
P20
D
Myc
E
Myc DAPI
E
Myc
Myc DAPI
F
GFP
medial
GFP
lateral
GFP NeuN
GFP NeuN

Figure 2. 1: Validation of the viral construct *in vivo*

(**A**) Schematic describing the PTHS gene therapy construct for expressing human *TCF4* with a C-terminus Myc-tag under control of a synthetic promoter (JeT). (**B**) P1 mouse during (left panel) and after (middle and right panels) intraventricular injection of AAV9 virus with dye. Black arrows indicate the eyes. A white error indicates transilluminated ventricle filled with virus and dye solution. (**C**) Schematic of experiment to evaluate hTCF4-Myc and GFP biodistribution ~ 3 weeks after ICV injection of AAV9/hTCF4-Myc or AAV9/GFP to neonatal mice. (**D**) Myc expression from the hippocampus of a P20 mouse following AAV9/hTCF4-Myc treatment as shown in panel B and C. Scale bars = 100 µm. (**E**) Higher magnification images of boxed regions in panel D. Scale bars = 20 µm. (**F**) GFP expression in the sagittal sections from a P20 mouse following AAV9/GFP treatment. Scale bars = 1 mm.

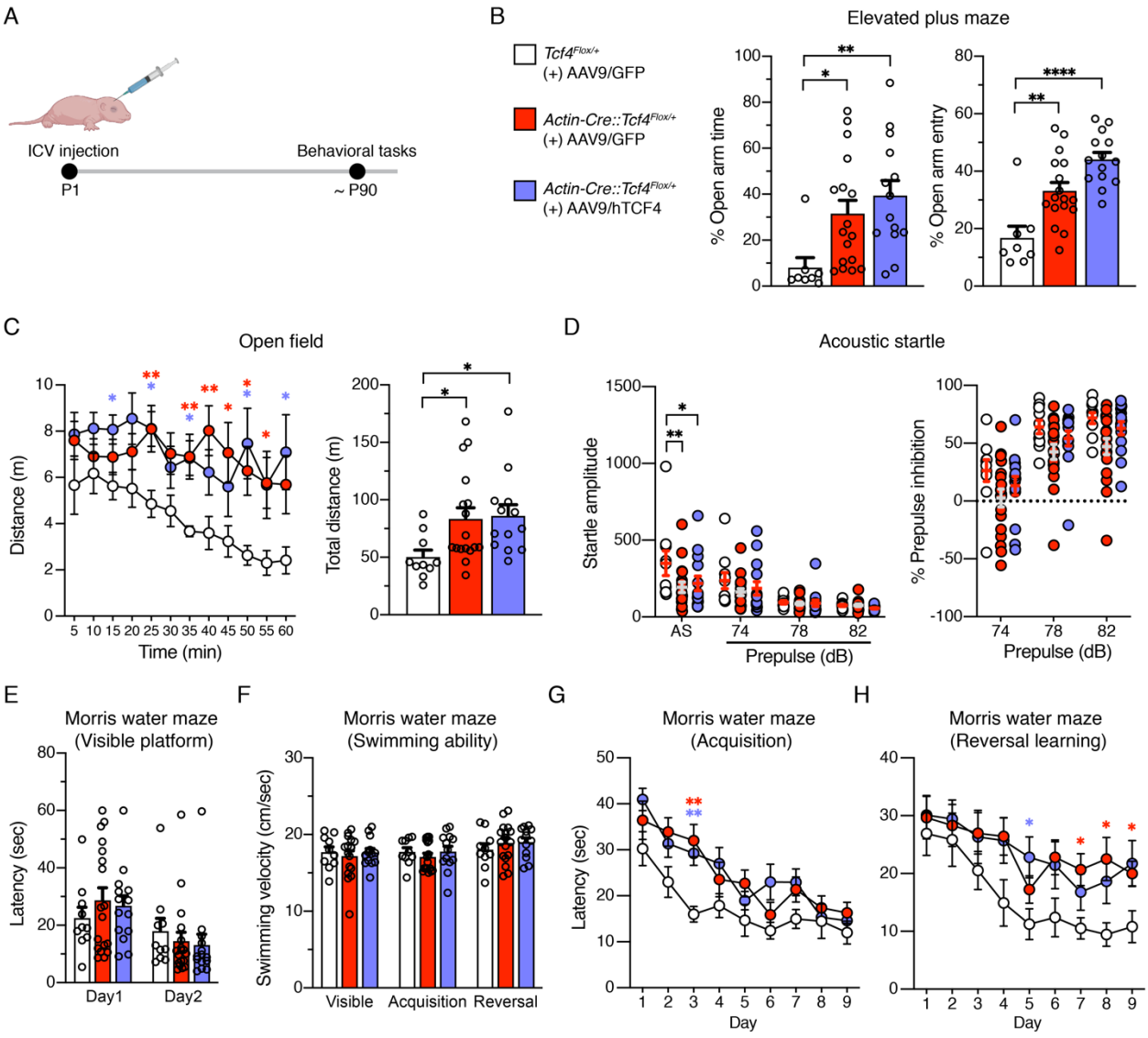

Figure 2. 2: Treating PTHS model mice with AAV9/hTCF4 did not rescue behavioral phenotypes.

(**A**) Schematic of experiment to examine the effect of AAV-mediated gene therapy approach on behavioral phenotypes in PTHS model mice. (**B**) Left panel: Percent time spent in the open arms of an elevated plus maze. Right panel: Percent of entries made into the open arms of the elevated plus maze. (**C**) Left panel: Distance traveled per 5 min. Right panel: Total distance traveled for the 1-hour testing period in the open field

arena. (**D**) Left panel: Response to acoustic startle (AS = 120 dB) alone or in combination with a prepulse sound level (74, 78, or 82 dB). Right panel: Percentage of prepulse inhibition. (**E**) Latency to find a visible platform in the Morris water maze task. (**F**) Swimming velocity during the visible platform, acquisition, and reversal test. (**G**) Latency to find a hidden platform during acquisition training. (**H**) Latency to find a hidden platform in a reversal learning task in which the platform is placed in a new location. All behavioral data were analyzed by Welch's ANOVA followed by Dunnett's *post hoc* or two-way ANOVA followed by Tukey's *post hoc*. Values are means ± SEM. *$p < 0.05$, **$p < 0.005$, ****$p < 0.0001$.

CHAPTER 3: REGION AND CELL TYPE DISTRIBUTION OF TCF4 IN THE POSTNATAL MOUSE BRAIN[1]

3.1 Introduction

Human *TCF4* is expressed in the prosencephalon and the ventricular zone of the central nervous system during fetal development, and its expression remains sustained in the adult forebrain (8). Similarly, mouse *Tcf4* is prominently expressed in the isocortex and hippocampus during development and in adulthood (24, 25). While these studies highlight broad regions in which TCF4 is particularly active, much less is known regarding the specific identity of cell types in which TCF4 is expressed. TCF4 expression has been reported in a subset of cortical neurons (25). However, it is not yet characterized which cortical neurons express TCF4, and whether brain regions outside the cortex contain TCF4-expressing cells. Moreover, TCF4-expressing hippocampal cell groups are largely unknown despite the prominent expression in the hippocampus.

Notwithstanding some basic information about the expression pattern of TCF4 in the mouse brain, effective TCF4 normalization strategies will require a deeper understanding of its regional and cell type-specific expression across development in both mouse and human brain. This is particularly true for gene therapy strategies that are attempting to address *TCF4* haploinsufficiency in PTHS by normalizing levels of gene expression. In order to facilitate these therapeutic efforts and further contextualize

[1] This chapter previously appeared as an article in the Frontiers in Neuroanatomy. The original citation is as follows: Kim H. "Region and Cell Type Distribution of TCF4 in the Postnatal Mouse Brain," *Front. in Neuroanat.* 14:42. (July 2020).

roles for TCF4 in brain development, I developed and validated a novel mouse model incorporating a Cre-dependent TCF4-GFP reporter. Using this line, I track TCF4-expressing brain regions and cell groups throughout postnatal development, with greater reliability and resolution than could previously be achieved using available antibodies (25).

3.2 Results

3.2.1 Validation of Tcf4-LGSL mouse model

To investigate the spatiotemporal profile of TCF4-expressing cells, I engineered mice with a LoxP-GFP-STOP-LoxP (LGSL) cassette introduced into intron 17 of the *Tcf4* allele (**Fig. 3.1A**). An adenovirus splicing acceptor was included in the cassette to avoid alternative splicing of intron 17 (**Fig. 3.1A**). This design allowed us to examine TCF4-expressing cells with high confidence, as GFP can be detected by commercial antibodies. Moreover, the insertion of a 2A self-cleaving peptide (P2A) enables GFP molecules to freely diffuse throughout the cytoplasm, making it possible to track axonal projections from TCF4-expressing neurons, though at the cost of not being able to use it to identify the subcellular localization of TCF4. The GFP and STOP cassette is flanked by LoxP sites, enabling their Cre-mediated deletion, and in turn, reinstating the capacity to express full-length, functional TCF4 from the locus.

As predicted from my design, brain lysates from $Tcf4^{+/+}$ (WT) mice produced a single full-length TCF4 band by Western blot, whereas lysates from $Tcf4^{LGSL/+}$ (Het) mice produced both the full-length and truncated TCF4 protein, and lysates from $Tcf4^{LGSL/LGSL}$ (Homo) mice produced only a truncated TCF4 band (**Fig. 3.1B**). GFP was

present only in *Tcf4*$^{LGSL/+}$ and *Tcf4*$^{LGSL/LGSL}$ lysates (**Fig. 3.1B**). The band intensity of full-length TCF4 was reduced by approximately half in lysates from *Tcf4*$^{LGSL/+}$ compared to WT mice (**Fig. 3.1C**: WT: 1.00 ± 0.02, n = 5; Het: 0.54 ± 0.03, n = 11; Homo: 0.00 ± 0.00, n = 3). GFP levels were higher in lysates from *Tcf4*$^{LGSL/LGSL}$ compared to *Tcf4*$^{LGSL/+}$ mice (**Fig. 3.1C**: WT: 0.00 ± 0.00; n = 5, Het: 0.36 ± 0.01, n = 11; Homo: 1.00 ± 0.00, n = 3). These results validated that the LGSL cassette produced GFP and truncated TCF4 protein.

To verify that GFP faithfully reports TCF4 expression, I performed dual *in situ* hybridization (ISH) using probes specific to Tcf4 or GFP mRNA. GFP signals were detected in cells from adult *Tcf4*$^{LGSL/+}$ mice, but absent in cells from WT mice (**Fig. 3.1D**), proving the specificity of the GFP probe detection. Tcf4 signals were observed in both WT and *Tcf4*$^{LGSL/+}$ mice (**Fig. 3.1E-F**). Quantification of cells expressing both GFP and *Tcf4* revealed an approximate 97% overlap (**Fig. 3.1G-H**: prefrontal cortex (PFC): 97.56 ± 0.31 %; CA1: 97.58 ± 0.13 %), as only 2.4 % of *Tcf4*-expressing cells lacked detectable GFP mRNA (**Fig. 3.1F and H**: PFC: 2.44 ± 0.32 %; CA1, 2.42 ± 0.13 %). These results verify that the GFP expression in *Tcf4*$^{LGSL/+}$ mice faithfully reports *Tcf4* expression.

3.2.2 Comparison of GFP reporter and TCF4 antibodies

Of commercially available TCF4 antibodies, only one has been validated for immunostaining using homozygous *Tcf4* knock-out tissues (25). I used this antibody to visualize TCF4-expressing cells in WT brain. I observed weak protein signals in brain cell nuclei at P7 (**Fig. 3.2A**). Under identical experimental conditions, I failed to detect

appreciable TCF4 protein signals at P15 and P80 (**Fig. 3.2B-C**). TCF4 expression may dwindle to undetectable levels, or cease altogether, over the course of brain maturation. To distinguish between these possibilities, I performed ISH for *Tcf4* in age-matched WT brains. I observed comparable numbers of *Tcf4*-expressing cells between neonatal and adult brains (**Fig. 3.2D-F**), indicating expression of *Tcf4* transcript persisted in most cells across postnatal development, albeit likely at reduced levels. Thus, the limited sensitivity of the TCF4 antibody might impede immunodetection of TCF4 protein in adult brain. Alternatively, TCF4 protein levels produced in adulthood might be too low to be detected by the antibody.

To directly compare sensitivities of TCF4 and GFP antibodies, I performed double immunohistochemistry in brain sections of $Tcf4^{LGSL/+}$ mice, from birth into adulthood. GFP and TCF4 labeling patterns were similar across postnatal development, though GFP labeling was of visually greater intensity than TCF4 labeling (**Fig. 3.2G-I**). The disparity in labeling intensity was also apparent at P10 and was even more pronounced by adulthood when TCF4 labeling outside of the hippocampus was barely detectable (**Fig. 3.2H-I**). I also detected GFP labeling within axonal projections (**Fig. 3.2G**). These data highlight advantages of the GFP reporter — increased sensitivity and the capacity to track the axonal projections of TCF4-expressing neurons—for mapping TCF4 expression patterns across all postnatal ages.

3.2.3 TCF4 expression patterns of the adult mouse brain

To examine adult patterns of TCF4 expression, I stained for GFP across the rostral to caudal extent in coronal sections from $Tcf4^{LGSL/+}$ mice (**Fig. 3.3A-H**). I

observed the most prominent GFP labeling intensity in the pallial region, which contains the olfactory bulb, cortex, and hippocampus (**Fig. 3.3B-G**). Cells in the glomerular (gm), external plexiform (pl), and granule layers (gr) of the olfactory bulb (OLF) were strongly labeled with GFP (**Fig. 3.3A**). Throughout the entire cortex, intense GFP staining was seen in almost all areas and in every layer (**Fig. 3.3B-G and I**). Expression was strong in the hippocampus, especially in the pyramidal cell layer of Ammon's horn (**Fig. 3.3J**), and in the cerebellum, highlighted by concentrated GFP labeling in the molecular (mo) and granule cell (gl) layers (**Fig. 3.3H and M**).

While the entire pallial region and cerebellum stained intensely for GFP, subsets of other brain regions were lightly and sparsely labeled for GFP. In the pallial derivatives, cells in the basolateral amygdala nucleus (BLA) and claustrum (CLA) were stained for GFP. In the subpallial derivatives, I detected GFP-positive cells in the central amygdala nucleus (CEA) and medial amygdala nucleus (MEA) (**Fig. 3.3C-E**). I also noted GFP labeling of cells in the caudoputamen (CP), nucleus accumbens (ACB), lateral septal nucleus (LS), medial septal complex (MS), and nucleus of the diagonal band (NDB) (**Fig. 3.3B-C and K**), although this labeling was much lighter, and the stained cell density was much lower than what I observed in the pallial region. In the hypothalamus, I observed the highest density of GFP-expressing cells in posterior hypothalamic nucleus (PH) (**Fig. 3.3D-E**). In the diencephalic prosomeres, the medial habenula (MH) stood out for its strong GFP labeling intensity (**Fig. 3.3D**), contrasting sharply with other thalamic nuclei that were generally devoid of detectable GFP (**Fig. 3.3D-E and L**). In the prethalamic structure, I observed GFP-positive cells in zona incerta (ZI). In the midbrain, GFP labeled cells in periaqueductal gray (PAG) and

superior colliculus (SC) (**Fig. 3.3E-G**). In the hindbrain, I observed GFP-expressing cells in the superior central nucleus raphe (CS), pontine gray (PG), vestibular nuclei (VNC), nucleus prepositus (PRP), spinal nucleus of the trigeminal (SPV), and dorsal cochlear nucleus (**Fig. 3.3G-H**).

The contrast in labeling intensity of GFP detected in the pallial region along with cerebellum and the rest of the brain suggests differences in TCF4-expressing cell densities. To compare the expression across different brain regions, I fluorescently labeled *Tcf4* in adult WT tissues via ISH and quantified *Tcf4*-containing cells. I detected *Tcf4* signals in all examined brain regions, including CA1, visual cortex (VC), BLA, PFC, CP, and TH (**Fig. 3.4**). Consistent with my qualitative observations of GFP labeling intensity (**Fig. 3.3**), the percentage of cells expressing *Tcf4* transcript was dramatically higher in CA1, VC, BLA, and PFC compared to CP and TH (**Fig. 3.4**).

3.2.4 TCF4 expression patterns of the neonatal and juvenile mouse brain

I investigated the spatial dynamics of TCF4 expression during postnatal brain development by examining GFP reporter expression at P1, P10, P20, and P60. At P1, the pallial region stood out with the strongest GFP staining. Other derivatives from prosencephalon, mesencephalon, and rhombencephalon were also stained for GFP. Cell densities were lower in these derivatives than the pallial region. The lowest level of GFP expression was detected in the thalamus and inferior colliculus. Intensely labeled axonal projections were unique to the P1 timepoint. Most notably, some GFP-stained axons were extended from the cortical neurons into discrete thalamic nuclei. Other GFP-stained cortical axons were extended to invade the hypothalamus and pons (**Fig.**

3.5A). I also detected the cerebral peduncle intensely stained for GFP. These labeling patterns demonstrate that, at an early postnatal stage, corticothalamic and subcerebral projection neurons expressed TCF4. Additionally, axons coursing through the corpus collosum, fimbria, internal capsule, fornix, and anterior commissure were labeled strongly for GFP (**Fig. 3.5A and 3.2G**). GFP expression remained high in the pallial region and cerebellum at P10. I also detected GFP-expressing cells throughout the hypothalamus, midbrain, and hindbrain. Strikingly, GFP expression level was slightly increased in the thalamus at this age compared with P1 (**Fig. 3.5B**). This slight increase is potentially caused by axonal fibers spreading into the midline nuclei. A similar pattern of corticothalamic fibers was reported at this age in transgenic mice that drive GFP in early cortical preplate and subplate neurons (79). At P20, GFP expression level was reduced in the thalamus, hypothalamus, midbrain, and hindbrain. The pallial region, cerebellum, and some hindbrain and hypothalamic nuclei were intensely stained for GFP (**Fig. 3.5C**). The expression pattern observed in P20 brain was conserved in P60 brain, although the overall expression level of P60 brain was slightly decreased compared with P20 brain. My data show that high levels of GFP labeling were persistently detected in the pallial region and cerebellum in all ages (**Fig. 3.5**). These data suggest that TCF4 could be involved in early stages of neuronal development across the entire brain, but as the brain matures, TCF4 function becomes increasingly restricted to the pallial region and cerebellum.

3.2.5 Glutamatergic and GABAergic cells, astrocytes, and oligodendrocytes express TCF4 in the prefrontal cortex

I used the GFP reporter line to characterize the cell type-specific expression of TCF4 in the PFC. GABAergic and glutamatergic neurons represent two major neuronal classes that I could more easily distinguish upon reciprocal Cre deletion, which succeeded in eliminating expression of the GFP reporter one class at a time. I generated *LGSL::Gad2-Cre* mice to delete GFP expression from GABAergic neurons (80). I detected relatively light GFP staining in putative glutamatergic neurons throughout the cortical layers (**Fig. 3.6A**). I also generated *LGSL::Nex-Cre* mice to delete GFP selectively from forebrain glutamatergic neurons (81). I detected strong residual labeling in GABAergic cells (**Fig. 3.6B**). To confirm that *Tcf4* expression is ubiquitous in these neuronal classes, I performed double ISH in adult WT PFC for *Tcf4* in combination with either *vGlut1* or *vGat*, which encode the vesicular transporters for glutamate and GABA, respectively. I found almost all *vGlut1*- and *vGat*-expressing cells contained *Tcf4* (**Fig. 3.6C-E and F-H**). These findings suggested that TCF4 may be ubiquitously expressed in cortical glutamatergic and GABAergic cell populations. Nearly all cortical GABAergic interneurons belong to one of three groups defined by the expression of parvalbumin (PV), somatostatin (SOM), and the ionotropic serotonin receptor 5HT3a (5HT3aR) (82). Each group differs in its morphological and electrophysiological properties and plays unique roles in cortical circuit function (83-85). To determine whether TCF4 is expressed in specific GABAergic interneuron subtypes, I performed coimmunostaining for GFP and representative subgroup-specific markers in the juvenile and adult *LGSL::Nex-Cre* mice. There are currently no suitable antibodies

for staining 5HT3aR, so I chose vasoactive intestinal peptide (VIP) as an alternative marker, which is expressed by approximately half of all 5HT3aR-expressing neurons (82, 86). I found that nearly all SOM, PV, and VIP labeled interneurons were copositive with GFP in the PFC (**Fig. 3.6I-K**) at P20 and P80, suggesting that TCF4-expressing GABAergic cells consist of SOM, PV, and VIP interneurons.

Over the course of my study, I observed that a subset of GFP-stained cells did not stain positive for NeuN (data not shown), indicating that TCF4 may be expressed in glial cell populations. I costained for GFP and either the astrocyte marker glial fibrillary acid protein (GFAP), or the microglia marker ionized calcium binding adaptor molecule 1 (IBA1), in *LGSL::Nex-Cre* mice. GFP/GFAP copositive astrocytes were present throughout the PFC of both juvenile and adult mice (**Fig. 3.6L**). However, GFP-stained glia did not costain for IBA1 (**Fig. 3.6M**). Due to the recently established role for TCF4 in regulating the maturation of oligodendrocyte progenitors (29), I expected that TCF4 would be expressed in oligodendrocyte lineage cells. Olig2 marks all stages of oligodendrocyte lineage, and APC (or CC1) marks the maturational process (87). The majority of Olig2/APC positive cells, reflecting mature, myelinating oligodendrocytes, stained for GFP in the PFC and corpus callosum at P20 (**Fig. 3.6N**). Similarly, a subset of immature oligodendrocytes, labeled only by Olig2, stained for GFP (**Fig. 3.6N**). My results show that among major glial cell populations in the brain, astrocytes and both immature and mature oligodendrocytes express TCF4, while microglia appear to lack TCF4 expression.

3.2.6 Pyramidal cells, GABAergic interneurons, and astrocytes express TCF4 in the hippocampus

Tcf4 deficient mice exhibited deficits in the behavioral tasks that require proper hippocampal functions. Additionally, a form of hippocampal synaptic plasticity was altered in these mice (54, 56). Therefore, I characterized TCF4-expressing cell types in this brain region to reveal which cell types might contribute to these phenotypes. First, I examined glutamatergic and GABAergic cell populations by staining for GFP in *LGSL::Gad2-Cre* and *LGSL::Nex-Cre* mice. As expected from my ISH data (CA1, **Fig. 3.4**), glutamatergic pyramidal cells of the CA1 region exhibited strong GFP labeling (**Fig. 3.7A**). Moreover, I detected strong residual labeling in GABAergic cells across the layers (**Fig. 3.7B**). The hippocampal GABAergic inhibitory circuits consist of SOM-, PV-, VIP-, neuropeptide Y-, calretinin-, and cholecystokinin-expressing interneurons (88). I tested whether some of these inhibitory interneurons expressed TCF4 by performing coimmunostaining in *LGSL::Nex-Cre* brain. I found that SOM-, PV- and VIP-positive neurons stained for GFP at P20 and P80 (**Fig. 3.7C-E**). GFP staining in *LGSL::Nex-Cre* mice revealed clearly identifiable star-shaped cells (rad. layer, **Fig. 3.7B**). The coimmunostaining result showed that GFAP-positive astrocytes stained for GFP (**Fig. 3.7F**). However, IBA-positive microglial cells were devoid of GFP (**Fig. 3.7G**). My results demonstrated that TCF4-expressing hippocampal cell groups consist of astrocytes, pyramidal cells, and SOM-, PV-, and VIP-containing interneurons.

3.2.7 SOM and PV interneurons and astrocytes express TCF4 in the striatum

The vast majority of striatal neurons signal through GABA to inhibit their target cells (89, 90). Because I observed that only ~19% of striatal cells express *Tcf4* (STR, **Fig. 3.4**), I speculated that these would comprise specific subgroups of GABAergic neurons. Using double ISH, I detected *Tcf4* signals in a subset of *vGat*-expressing cells (**Fig. 3.8A-C**). I subsequently employed a double immunostaining approach in juvenile and adult *Tcf4*$^{LGSL/+}$ mice to further define TCF4-expressing GABAergic population. I found that the GFP-labeled cells were not colocalized with medium spiny neurons (MSNs), marked by DARPP32 (**Fig. 3.8D**), indicating that GABAergic MSNs do not express TCF4. Cholinergic interneurons, marked by choline acetyltransferase (ChAT), represent another major cell GABAergic class in the striatum in which GFP was not expressed (**Fig. 3.8E**). SOM and PV expression characterizes other GABAergic interneuron types in the striatum (91). I detected GFP in SOM- and PV-positive interneurons at P20, and this colocalization persisted in the adult striatum (**Fig. 3.8F-G**). Interestingly, a few SOM or PV positive cells did not stain for GFP, raising the possibility that TCF4 expression could confer unique functional properties to subsets of PV and SOM interneurons. I showed earlier in this study that TCF4 was expressed in astrocytes, but not microglial cells, in the cortex and hippocampus. Thus, I asked whether this expression pattern also applied to the striatum. I detected GFP in GFAP-positive cells, but not in IBA1-positive cells (**Fig. 3.8F-G**). Collectively, these data suggest that TCF4 expression in the striatum is restricted to PV and SOM interneurons and astrocytes, but not to medium spiny, cholinergic neurons, and microglial cells.

3.2.8 TCF4 is enriched in the molecular and granule cell layer of the cerebellar cortex

I consistently observed strong GFP immunoreactivity in the cerebellum across postnatal development. Thus, I further characterized TCF4 distribution in this structure, focusing on the molecular, Purkinje cell, and granule cell layers. At P10, a timepoint of ongoing cerebellar histogenesis (92), I found that GFP was enriched in the molecular layer (ml) and inner granule layer (igl), but absent in the external granule layer (egl) and Purkinje cell layer (**Fig. 3.9A-D**). NeuN staining clearly marked neurons with a multipolar morphology, presumably traversing the molecular layer toward the inner granule layer (**Fig. 3.9B**). These cells were negative for GFP (**Fig. 3.9A-C**), suggesting that migrating granule cells do not express TCF4. In the inner granule layer, where post-migratory granule cells undergo maturation, I infrequently found NeuN-positive cells that costained with GFP (**Fig. 3.9A-C**). By adulthood, however, nearly all NeuN-positive neurons in the granule layer costained for GFP (**Fig. 3.9E-G**), leading us to surmise that cerebellar granule cells only upregulate TCF4 expression as they mature. Regardless of age, GABAergic Purkinje cell bodies, labeled by calbindin, lacked GFP staining (**Fig. 3.9D and H**). Consistent with my GFP immunostaining results, ISH for *Tcf4* in adult wildtype cerebellum confirmed that most granule cells expressed *Tcf4*, while GABAergic Purkinje cells did not (**Fig. 3.9I-K**). I also detected *Tcf4*-expressing cells in most GABAergic interneurons of the molecular layer (**Fig. 3.9I-K**).

3.3 Discussion

It is imperative to understand the cellular distribution of TCF4 during postnatal development in order to guide the delivery of therapeutics for TCF4-linked disorders. Towards this goal, I developed a mouse with a TCF4-GFP reporter that conferred greater sensitivity for detecting TCF4 expression than existing antibody detection methods. I validated the TCF4-GFP reporter mouse model by using double *in situ* labeling to show that about 98% of *Tcf4*-containing cells express GFP, proving the mouse model as a faithful reporter for TCF4. While the GFP reporter was designed to diffuse freely through the cytoplasm, and thus is not a marker of TCF4 subcellular localization, the reporter offers the advantage that it can label dendritic arborizations and axonal projections of TCF4-expressing neurons. To improve the ability to observe TCF4-expressing cell types, I conditionally deleted the GFP reporter in a Cre-dependent manner. This allowed us to observe the remaining GFP-positive cells more easily with an improved signal to noise ratio. I used these approaches, coupled with double-labeling immunohistochemistry and *in situ* hybridization, to characterize the cell type-specific and spatiotemporal expression of TCF4 in the postnatal mouse brain.

3.3.1 TCF4 expression patterns and their implications in pathology of TCF4-linked disorders

Prefrontal cortex

Rare *TCF4* single nucleotide variants have been described in schizophrenia patients whose symptoms include impairments of attention, memory, social cognition, and executive functions (33, 93). *TCF4* mutations have been found in large-scale

genotyping studies in patients with PTHS and intellectual disability (12, 49). Collectively, these studies implicate TCF4 in a range of brain disorders that are commonly associated with cognitive dysfunction. The prefrontal cortex is linked with a range of cognition including cognitive control, lower-level sensory processing, memory, and motor operations (94). The hippocampus supports learning and memory functions in a spatiotemporal context (95, 96). The prefrontal cortex and hippocampus are thus suspected pathophysiological loci for TCF4-linked disorders. TCF4 is enriched in most cortical and hippocampal cells, including excitatory and inhibitory neurons, as well as astrocytes, and oligodendrocytes, in the juvenile and adult mouse brain. These findings in TCF4-expressing cell groups support the idea that functions of the prefrontal cortex and hippocampus are particularly susceptible to subtle changes in TCF4 expression. TCF4 loss is associated with defects in cortical cell positioning, dendritic spines, and arborizations (24, 41). TCF4 haploinsufficiency results in reduced hippocampal volume and cortical thickness in mice (25). These structural phenotypes are likely linked to functional consequences, including abnormal neuronal excitability and synaptic plasticity in the prefrontal cortex and hippocampus, which are consistently observed across multiple PTHS mouse models (28, 54, 56). These cell physiological defects in turn likely contribute to the impairments in cognition and memory functions in patients with TCF4-linked disorders.

Striatum

Severe motor delay and stereotypic behavior are consistent phenotypes observed in patients with PTHS (19, 45). However, the potential mechanism underlying

motor deficits and stereotypies remains unknown. The striatum is involved in translating cortical activity into adaptive motor actions and controlled movement (97). At the circuit levels, some striatal interneurons receive direct cortical afferents. For example, activity of striatal PV interneurons, known to inhibit MSNs, are enhanced by cortical stimulation. Regardless of cortical projections, SOM interneurons locally target MSNs and ChAT-positive neurons (98). TCF4 is expressed in PV and SOM interneurons, but not in MSNs and ChAT-positive neurons, suggesting that TCF4 loss may alter striatal circuit functions through PV and SOM interneurons. Disruptions in GABAergic circuits of the striatum have been found in neuropsychiatric disorders and autism (99-101). Further experiments will be required to determine whether GABAergic circuit dysfunction occurs with TCF4 loss, and if so, whether it is the direct cause of motor delay and stereotypic behaviors.

Cerebellum

The cerebellum contributes to motor coordination, cognitive processing and emotional control (102). It is structurally and functionally abnormal in patients diagnosed with neurodevelopmental disorders (103). Cognitive functions are impaired in individuals with developmental reductions in cerebellar volume. Also, the degree of volume reduction is correlated with the degree of cognitive impairment (104, 105). Patients with PTHS display reduced volume of the cerebellum (46, 47), which may contribute to severity of cognitive and motor impairment. The adult human cerebellum expresses high levels of TCF4 (25). Similar to the human brain, TCF4 is prominently expressed in the mouse cerebellum during postnatal development and in adulthood. My data thus

suggest that the cerebellum is a candidate brain region that needs to be evaluated to determine whether TCF4 regulates cerebellar structure, and perhaps function. I found that differentiated and migrating granule cells repress TCF4 expression, while post-migratory mature granule cells upregulate TCF4 expression. My findings indicate that TCF4 is positioned to modulate maturation of the granule cells after migration. Future study will need to address whether TCF4 loss or dysfunction alters cerebellar anatomy and local circuit function, and if so, whether changes in cerebellar circuit directly cause motor and cognitive deficits.

Axonal projection

Spatial specificity of axonal projections across different brain regions is important for normal brain development and function (106-108), and TCF4 could be positioned to affect such projections. The TCF4 reporter mouse allowed us to visualize projecting axons, as the GFP reporter was free to diffuse throughout the cytoplasmic compartment. The GFP reporter revealed corticothalamic projections and what appeared to be the corticospinal and corticobulbar tracts. Because corticothalamic neurons are largely localized in layer 6, and the corticospinal and corticobulbar tracts are largely localized to layer 5 (79, 109), my data suggest that TCF4 may be expressed in both layer 5 and 6 projection neurons, although additional experiments will be required to directly confirm this. Several studies demonstrated that TCF4 regulates the laminar pattern and structure of the cortex (24, 41), and my findings suggest that TCF4 may also be critical to the development of corticofugal projections. To test this

possibility, the consequences of TCF4 loss on axonal projections during embryonic development need to be thoroughly examined.

3.4 Materials and Methods

Mice

I generated *Tcf4*$^{LGSL/+}$ mice through the University of North Carolina, Chapel Hill (UNC) Animal Models Core facility. I utilized CRISPR/Cas9-mediated homologous recombination to generate *Tcf4-LoxP-GFP-Stop-LoxP* (*Tcf4*^{LGSL}) knock-in mice on the C57BL/6J background. The *Tcf4*^{LGSL} allele was generated by inserting a cassette, comprised of a LoxP site, adenovirus splice acceptor, porcine teschovirus-1 2A (P2A) site, EGFP coding sequence, 3 copies of SV40 polyadenylation sequence (Stop), FRT site, and another LoxP site (**Fig. 3.1A**). This cassette was inserted into *Tcf4* intron 17. The sequence of the guide RNA (gRNA) was 5'- GTCGTGCCTTACGTAGCTGGG-3'. Mouse embryos were injected with a mixture of 400 nM Cas9 protein, 50 ng/μl *in vitro* transcribed gRNA, and 20 ng/μl supercoiled donor plasmid. The donor plasmid was constructed with 1017 bp 5' homology arm, the LoxP-GFP-Stop-LoxP cassette, and 884 bp 3' homology arm. Potential founder animals were screened for the presence of the insertion event by 5' and 3' polymerase chain reaction (PCR) assays consisting of one primer outside the targeting vector homology arms and one primer unique to the insertion event. The 5' assay primers were Tcf4-5ScF1 (5'-GCACTTCAGGGATCGCTTA-3') and AdSA-R2 (5'-GGGACAGGATAAGTATGACATCATC-3'), which produced a 1224 bp band. The 3' assay primers were SV40pA-F2 (5'-GCTGATCCGGAACCCTTAAGC-3') and Tcf4-

3ScR1 (5'-CCGCCCTAATTGTTCAAAGAG-3'), which produced a 1109 bp band. Two chosen founders were checked for off-target mutations at 10 predicted off-target sites. No mutations were detected at the off-target sites screened in two founder animals. The *Tcf4*$^{LGSL/+}$ knock-in mice were genotyped via PCR. The primer set of Tcf4-5ScF1 and Tcf4-3ScR1 or SV40pA-F2 and Tcf4-3ScR1 was respectively used to amplify the wildtype or LGSL knock-in allele. The female *Tcf4*$^{LGSL/+}$ mice were mated with heterozygous males from one of three Cre-expressing lines: *Nex-Cre* (81), which Klaus-Armin Nave generously provided, and *Gad2-Cre* (RRID:IMSR_JAX:010802). All mice were maintained on a congenic C57BL/6J background. All research procedures using mice were approved by the Institutional Animal Care and Use Committee at the UNC and conformed to National Institutes of Health guidelines.

Western blotting

Embryonic day 16.5-18.5 brains were dissected in ice-cold phosphate-buffered saline (PBS, pH = 7.3) and then immediately frozen with dry ice. Frozen brain samples were homogenized in glass homogenizers with ice-cold RIPA buffer [50 mM Tris-HCl, pH 7.4, 150 mM NaCl, 1% Triton X-100, 0.1% sodium dodecyl sulfate (SDS), and 0.5% Na deoxycholate] supplemented with 2 mM EDTA pH 8.0 and a protease inhibitor cocktail (Sigma, Saint Louis, MO). Tissue homogenates were cleared by centrifugation at 4°C for 20 mins. Protein samples were mixed with 4x protein loading buffer (Li-COR, Lincoln, NE) and 2-mercaptoethanol (Sigma) and incubated in 95°C for 5-7 mins. They were resolved by SDS-polyacrylamide gel electrophoresis and transferred to nitrocellulose membranes. Membranes were blocked for 1 hour at room temperature in

Odyssey blocking buffer (Li-COR) prior to incubation overnight at 4°C with primary antibodies diluted 1:500 with blocking buffer. Membranes were subsequently washed repeatedly with PBS (0.1M Phosphate, 1.5M NaCl) containing 0.1% Tween-20 (PBSTween) prior to incubation for 1 hour at room temperature with secondary antibodies prepared in the dilution of 1:5000 in blocking buffer. The following secondary antibodies were used: donkey anti-mouse 800CW (Li-COR, 926-32212) or donkey anti-rabbit Alexa 680 (Invitrogen, A10043). Finally, blots were washed repeatedly in PBSTween followed by PBS alone prior to imaging with the Odyssey imaging system (Li-COR).

Tissue preparation

Postnatal mice were anesthetized with sodium pentobarbital (60 mg/kg i.p.) before transcranial perfusion with 25 ml of PBS immediately followed by phosphate-buffered 4% paraformaldehyde (pH 7.4). Brains were postfixed overnight at 4°C before 24-hour incubations in PBS with 30% sucrose. Brains were sectioned coronally or sagittally at 40 μm using a freezing sliding microtome (Thermo Scientific, Kalamazoo, MI). Sections were stored at -20°C in a cryopreservative solution (45% PBS, 30% ethylene glycol, and 25% glycerol by volume).

Histology and immunostaining

For chromogenic staining, sections were rinsed several times with PBS, and endogenous peroxidases were quenched by incubating for 5 mins in 1.0% H_2O_2 in MeOH, followed by PBS rinsing. Sections were washed with PBS containing 0.2%

Triton X-100 (PBST) several times. Then sections were blocked with 5% normal goat serum in PBST (NGST) for 1 hour at room temperature. Blocked sections were incubated in primary antibodies diluted in NGST for 24 hours at 4°C. After incubation in primary antibodies, sections were rinsed several times in PBST and incubated for 1 hour at room temperature in biotinylated goat anti-rabbit secondary antibodies (Vector BA-1000, Burlingame, CA) diluted 1:500 in NGST. Sections were then rinsed in PBST prior to tertiary amplification for 1 hour with the ABC elite avidin-biotin-peroxidase system (Vector PK-7100). Further rinsing with PBST preceded a 3-minute incubation at room temperature in 3'3'-diaminobenzidine (DAB) chromogenic substrate (0.02% DAB and 0.01% H_2O_2 in PBST) to visualize immune complexes amplified by avidin-biotin-peroxidase.

For immunofluorescent staining, sections were rinsed several times with PBS and PBST before blocking with NGST or 5% bovine serum albumin (BSA) in PBST for 1 hour at room temperature. Sections were then incubated with primary antibodies diluted in NGST or BSA at 4°C overnight. The list of primary antibodies used is provided in **Table 3.1**. Sections were rinsed several times with PBST and then incubated with secondary antibodies for 1 hour at room temperature. The following secondary antibodies from Invitrogen (Carlsbad, CA) were used at a 1:1000 dilution: goat anti-mouse Alexa 568 (A11031); goat anti-mouse Alexa 647 (A21240); goat anti-rabbit Alexa 568 (A11011); goat anti-chicken Alexa 488 (A11039); or donkey anti-goat Alexa 568 (A11057). In all experiments, 4',6-diamidino-2-phenylindole (DAPI; Invitrogen D1306) was added during the secondary antibody incubation at a concentration of 700 ng/ml for

nuclear counterstaining. Brain sections compared within figures were stained within the same experiment, under identical conditions.

In situ hybridization

RNAscope Fluorescent Multiplex Assay, designed to visualize multiple cellular RNA targets in fresh frozen tissues (110), was used to detect *Tcf4* (Cat No. 423691), EGFP (Cat No. 400281-C2), *vGat* (Cat No. 319191-C3), and *vGlut1* (Cat No. 416631-C2) in mouse brain (Advanced Cell Diagnostics, Newark, CA). The target region of the *Tcf4* probe is 1120-2020 bp of mouse *Tcf4* mRNA (NM_001083967.1). Brains were extracted and frozen in dry ice. Sections were taken at a thickness of 16 μm. Staining procedure was completed to manufacturer's specifications.

Imaging and figure production

Images of brain sections stained with DAB histochemistry were obtained with a Nikon Ti2 Eclipse Color and Widefield Microscope (Nikon, Melville, NY). Images of brain sections stained by using fluorophore-conjugated secondary antibodies were obtained with Zeiss LSM 710 Confocal Microscope, equipped with ZEN imaging software (Zeiss, Jena, Germany). Images compared within the same figures were taken within the same imaging session using identical imaging parameters. Images within figure panels went through identical modification for brightness and contrast by using Fiji Image J software. Figures were prepared using Adobe Illustrator software (Adobe Systems, San Jose, CA).

Data analysis

Images for ISH colocalization analysis were captured from consistent coronal section planes across different mouse brains (PFC, STR: ~ 1.10 mm; CA1, BLA, TH: ~ -2.06 mm; VC: ~ -2.70 mm from bregma). The DAPI image from each brain region (265.69 x 265.69 μm) was converted to 8-bit in black and white, and its threshold was adjusted using the Huang method built into Fiji software. For the image with *Tcf4* or GFP staining, the IsoData threshold method was consistently applied. To identify mean *Tcf4* or GFP fluorescence intensity level for each nucleus (DAPI), I used CellProfiler software, which is a free open-source software that allows one to measure and analyze cell images automatically (111).

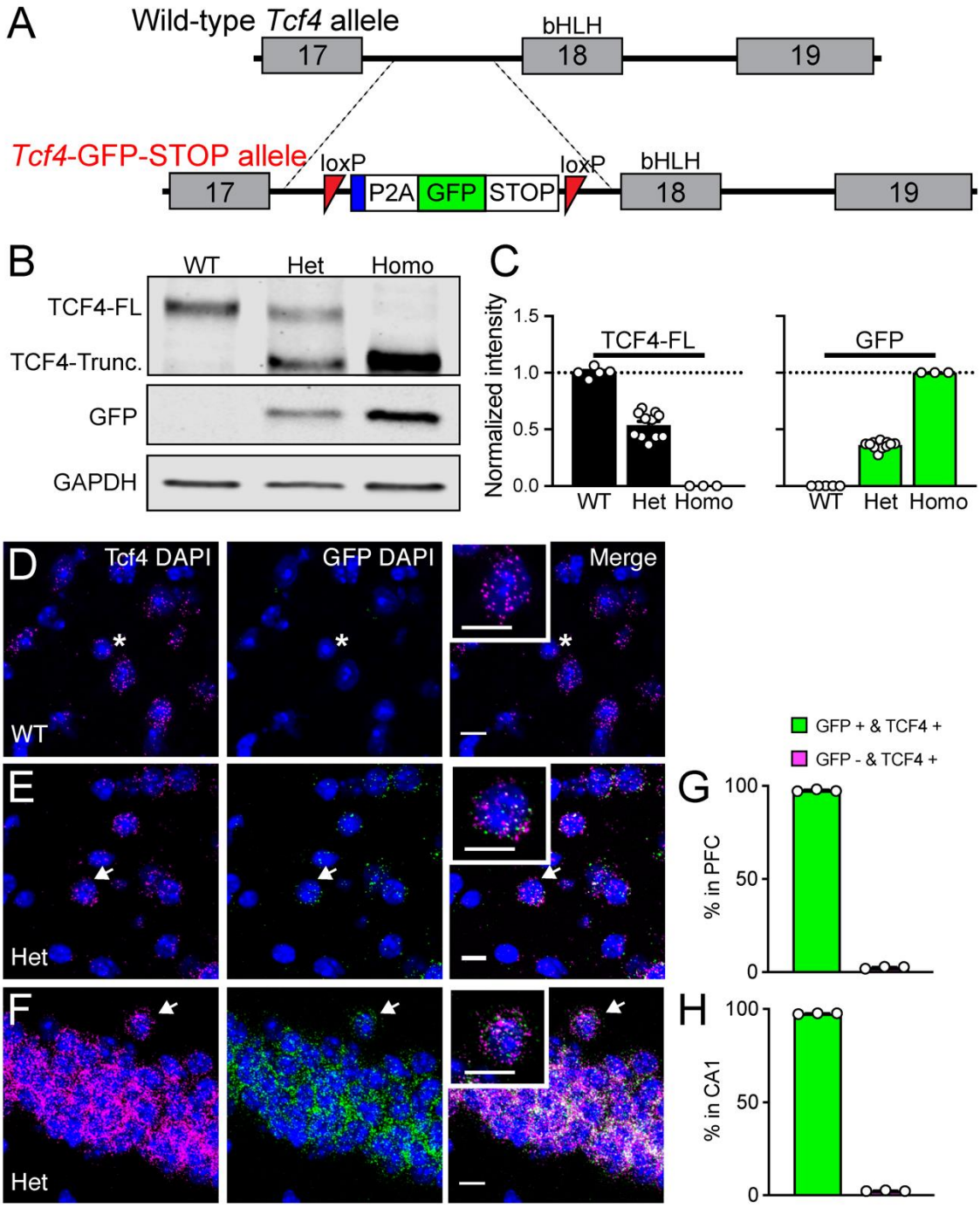

Figure 3. 1: Validation of *Tcf4-LGSL* mice that faithfully report TCF4 expression.

(A) Schematic of the strategy to generate C57BL/6J mice carrying the LoxP-P2A-GFP-STOP-LoxP cassette upstream of the basic helix-loop- helix region. Adenovirus splicing

acceptor is shown by the blue box. **(B)** Representative Western blot for TCF4, GFP, and GAPDH loading control protein in embryonic brain lysates from *Tcf4*$^{+/+}$ (WT), *Tcf4*$^{LGSL/+}$ (Het), and *Tcf4*$^{LGSL/LGSL}$ (Homo) mice. The TCF4 antibody (recognizes mouse TCF4 aa 50-150) is designed to detect a long isoform of TCF4. I detected a TCF4 full length protein (TCF4-FL) band at approximately 76 kDa that corresponds to the long isoform in WT lysates. A TCF4 truncated protein (TCF4-Trunc.) was detected at approximately 65 kDa in Het lysates. A band for GFP or GAPDH protein was detected at approximately 26 or 35 kDa, respectively. **(C)** Quantification of Western blotting for TCF4-FL and for GFP. **(D-F)** Dual fluorescence ISH for *Tcf4* (magenta) and GFP (green) from PFC of P80 WT and *Tcf4*$^{LGSL/+}$, and CA1 of *Tcf4*$^{LGSL/+}$ mice. Asterisk indicates a cell expressing only *Tcf4*, and arrows indicate cells co-expressing *Tcf4* and GFP. Insets are higher magnifications. Scale bars = 10 µm. **(G, H)** Quantification of GFP-positive and -negative cells in *Tcf4*-expressing cells in the PFC and CA1 region (n = 3 mice). Data represent mean ± SEM.

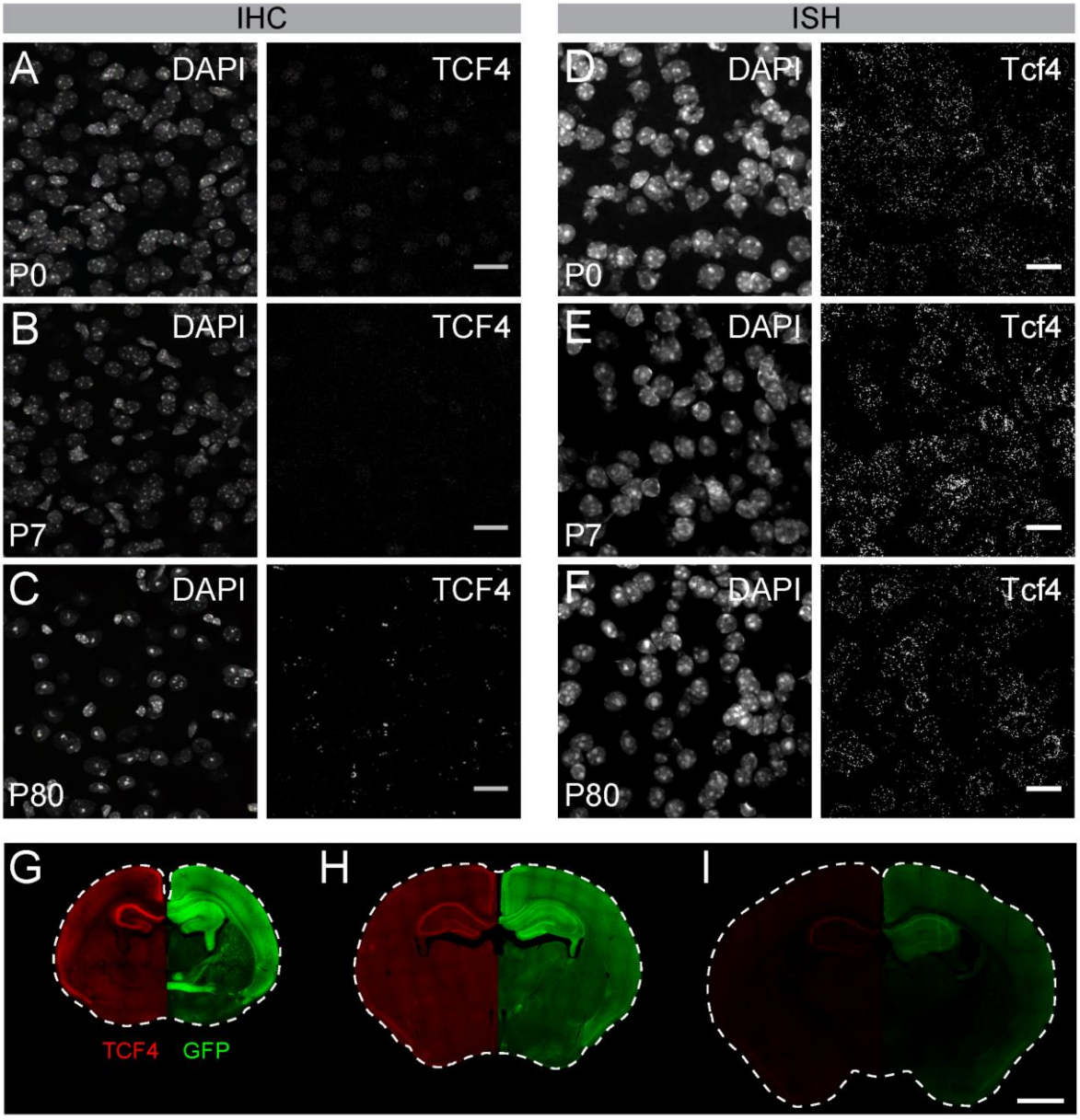

Figure 3. 2: GFP reporter enhances sensitivity to detect TCF4 by immunohistochemistry.

(A-C) Immunostaining and **(D-F)** ISH of TCF4/*Tcf4* and DAPI from P7, P15, and P80 mouse cortex. Immunostaining shows decreased detection of TCF4 protein using TCF4 antibody, whereas ISH shows comparable number of *Tcf4* expressing cells during postnatal development. Scale bars = 20 µm. (**G-I)** Dual immunostaining of P0, P7, and

P80 using TCF4 and GFP antibodies in coronal sections from *Tcf4*$^{LGSL/+}$ mice. Image is taken from the same double-labeled section. Scale bar = 1 mm.

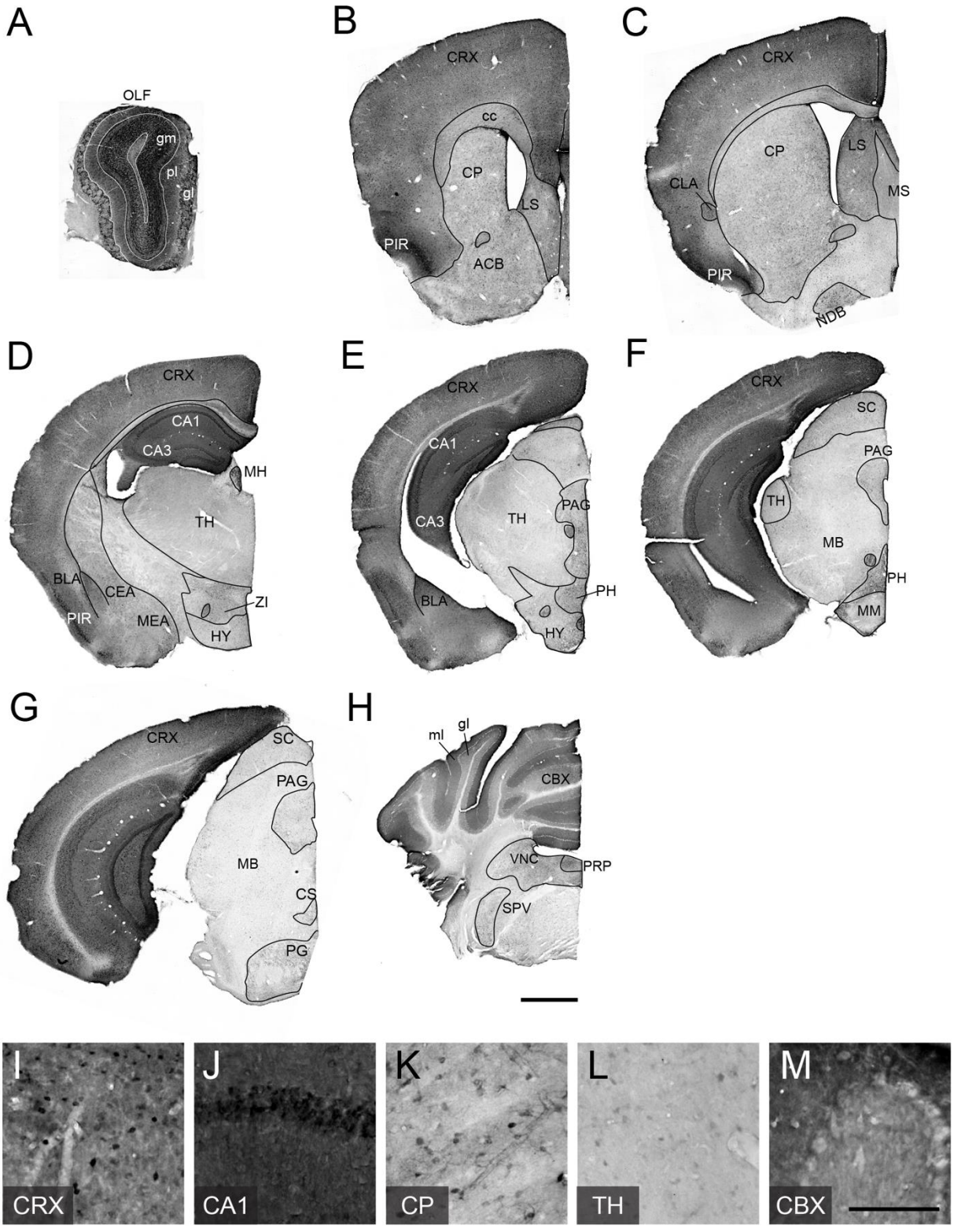

Figure 3. 3: TCF4 expression patterns of adult mouse brain.

(A-H) DAB immunostaining of GFP (for TCF4) in coronal brain sections of adult *Tcf4*$^{LGSL/+}$ mice. **(I-N)** High magnification view of CRX, CA1, CP, TH, and CBX. TCF4-expressing cells are prominently found in CRX, CA1, and CBX. Scale bars = 1 mm and 200 µm for higher magnification insets. The list of abbreviations used is provided in **Table 3.2**.

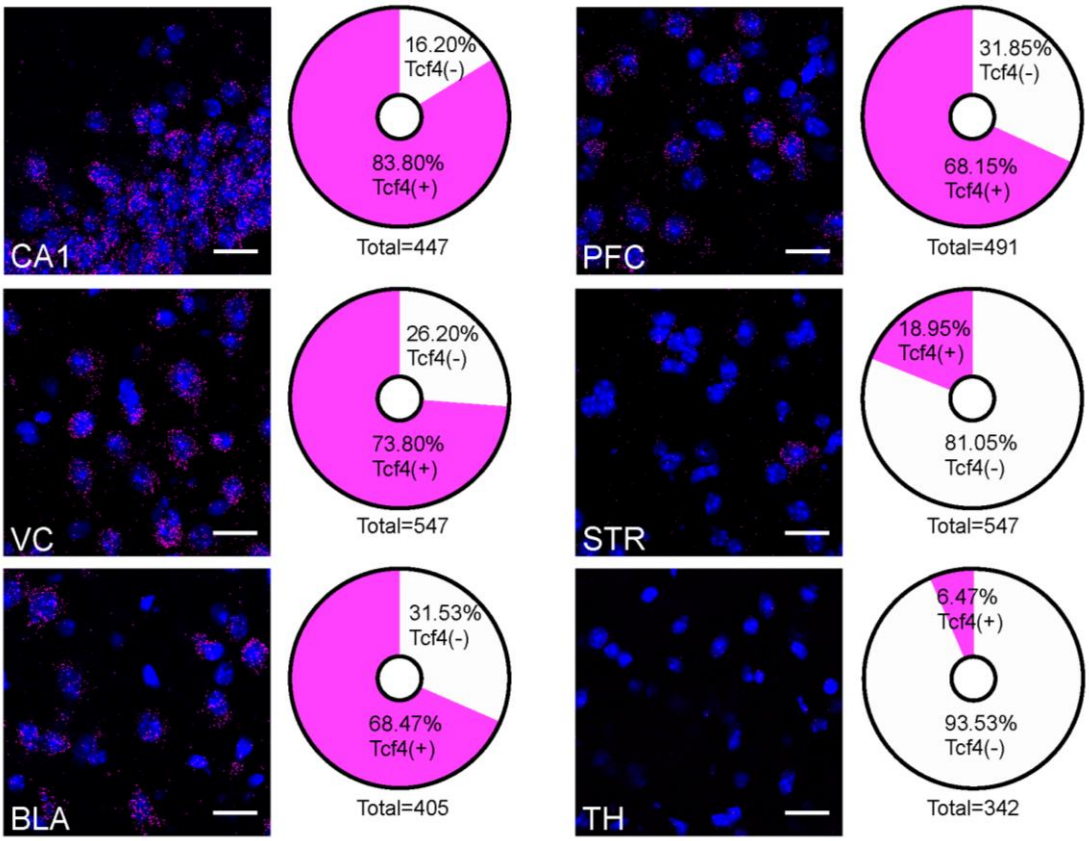

Figure 3. 4: Quantification of *Tcf4*-expressing cells in multiple brain regions of adult WT brain.

Representative ISH images of *Tcf4* and DAPI and proportionality of *Tcf4*-positive (magenta) and -negative (white) cell populations in CA1, VC, BLA, PFC, STR, and TH. *Tcf4* mRNA is present at high levels in the CA1, VC, BLA, and PFC. The total numbers in the pie chart center represent the quantified DAPI cells per brain region. Values represent the mean percentages. n = 3 mice. Scale bars = 20 µm.

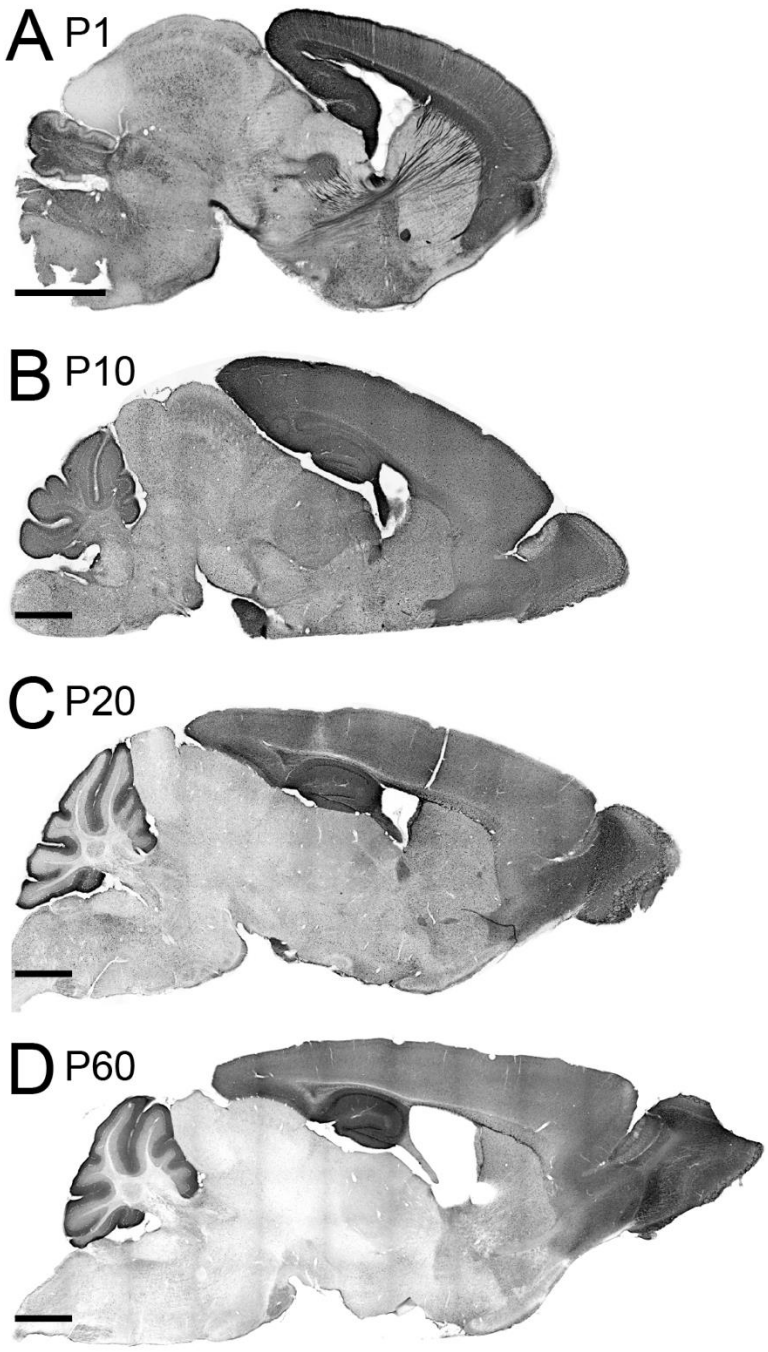

Figure 3. 5: TCF4 expression patterns of the neonatal and juvenile mouse brain.

(**A-D**) DAB immunostaining of GFP (for TCF4) in sagittal brain sections of *Tcf4*$^{LGSL/+}$ mice at P1, P10, P20 and P60. A similar staining pattern largely persists throughout postnatal development. Scale bars = 1 mm.

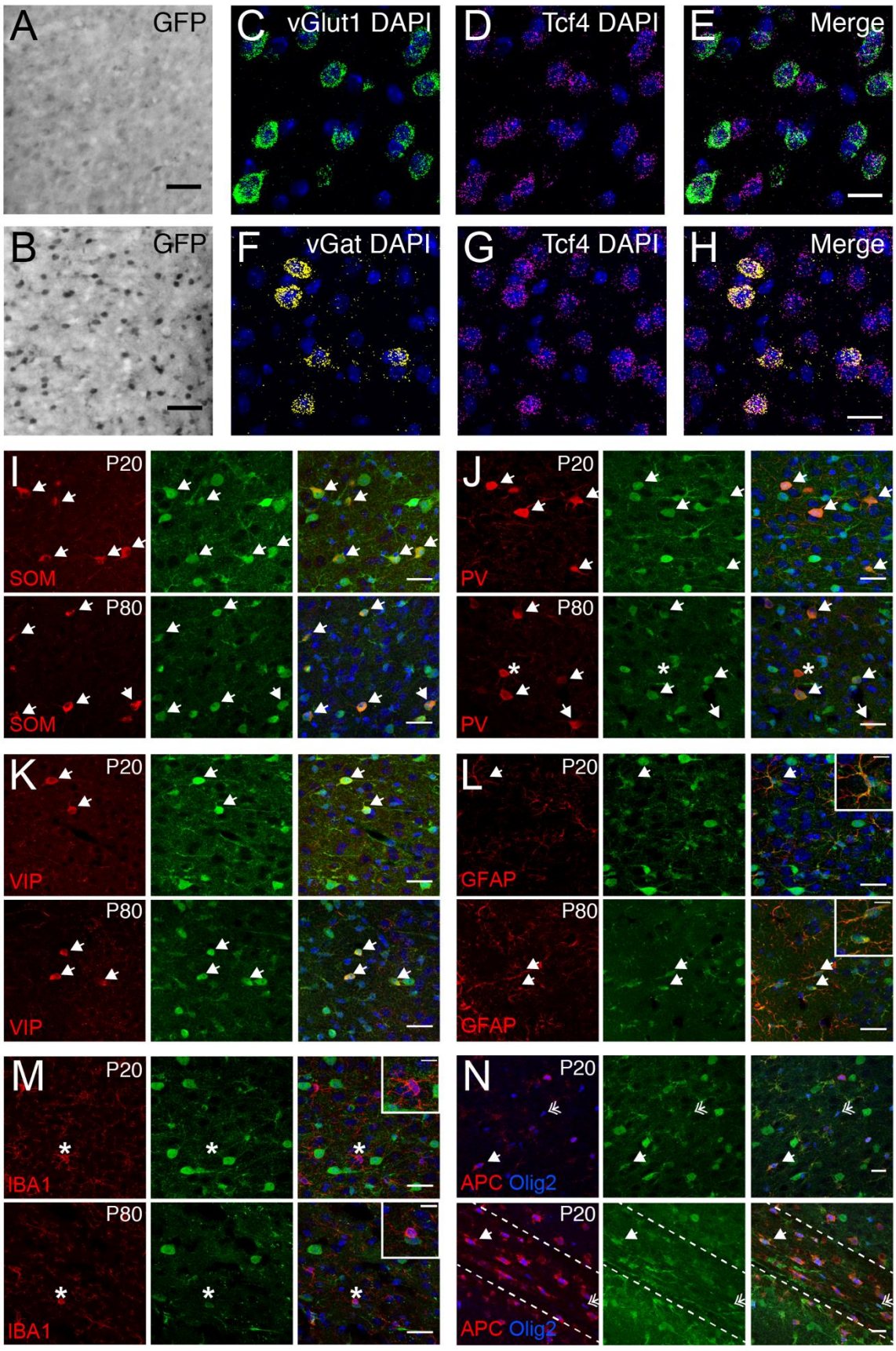
A GFP
C vGlut1 DAPI
D Tcf4 DAPI
E Merge
B GFP
F vGat DAPI
G Tcf4 DAPI
H Merge
I P20
SOM
P80
SOM
J P20
PV
P80
PV
K P20
VIP
P80
VIP
L P20
GFAP
P80
GFAP
M P20
IBA1
P80
IBA1
N P20
APC Olig2
P20
APC Olig2

Figure 3. 6: Glutamatergic, GABAergic cells, astrocytes, and oligodendrocytes express TCF4 in the PFC.

(**A, B**) DAB immunostaining of GFP (for TCF4) in coronal sections of P80 *LGSL::Gad2-cre* or *LGSL::Nex-cre* mice where GFP protein is deleted in inhibitory or excitatory neurons, respectively. Both glutamatergic and GABAergic cells express TCF4. Scale bars = 0.5 mm. (**C-E, F-H**) Dual ISH for *vGult1* and *Tcf4* and for *vGat* and *Tcf4* in P80 WT brain tissue, confirming that *Tcf4* mRNA is present in *vGlut1*- and *vGat*-expressing cells. Scale bars = 20 µm. **(I-K**) Dual immunostaining of interneuron subtype-specific markers, SOM, PV, or VIP, and GFP (for TCF4) in P20 and P80 *LGSL::Nex-cre* mice. TCF4 is expressed in nearly all SOM-, PV-, and VIP-positive interneurons (arrows). Asterisk represents rare interneuron that does not express GFP. Scale bars = 30 µm. (**L, M**): Dual immunostaining of astrocyte marker, GFAP, or microglial marker, IBA1, and GFP (for TCF4) in P20 and P80 *LGSL::Nex-cre* mice. GFAP-labeled cells express GFP (arrows), but IBA1-labeled cells do not express GFP (asterisk). Scale bars = 30 or 10 µm for higher magnification insets. (**N**) Triple immunostaining of APC, Olig2 and GFP (for TCF4) in the PFC (top panel) and corpus callosum (bottom panel) of P20 *LGSL::Nex-cre* mice. TCF4 is expressed in mature (arrow) and immature (double arrow) oligodendrocytes. Scale bars = 20 µm.

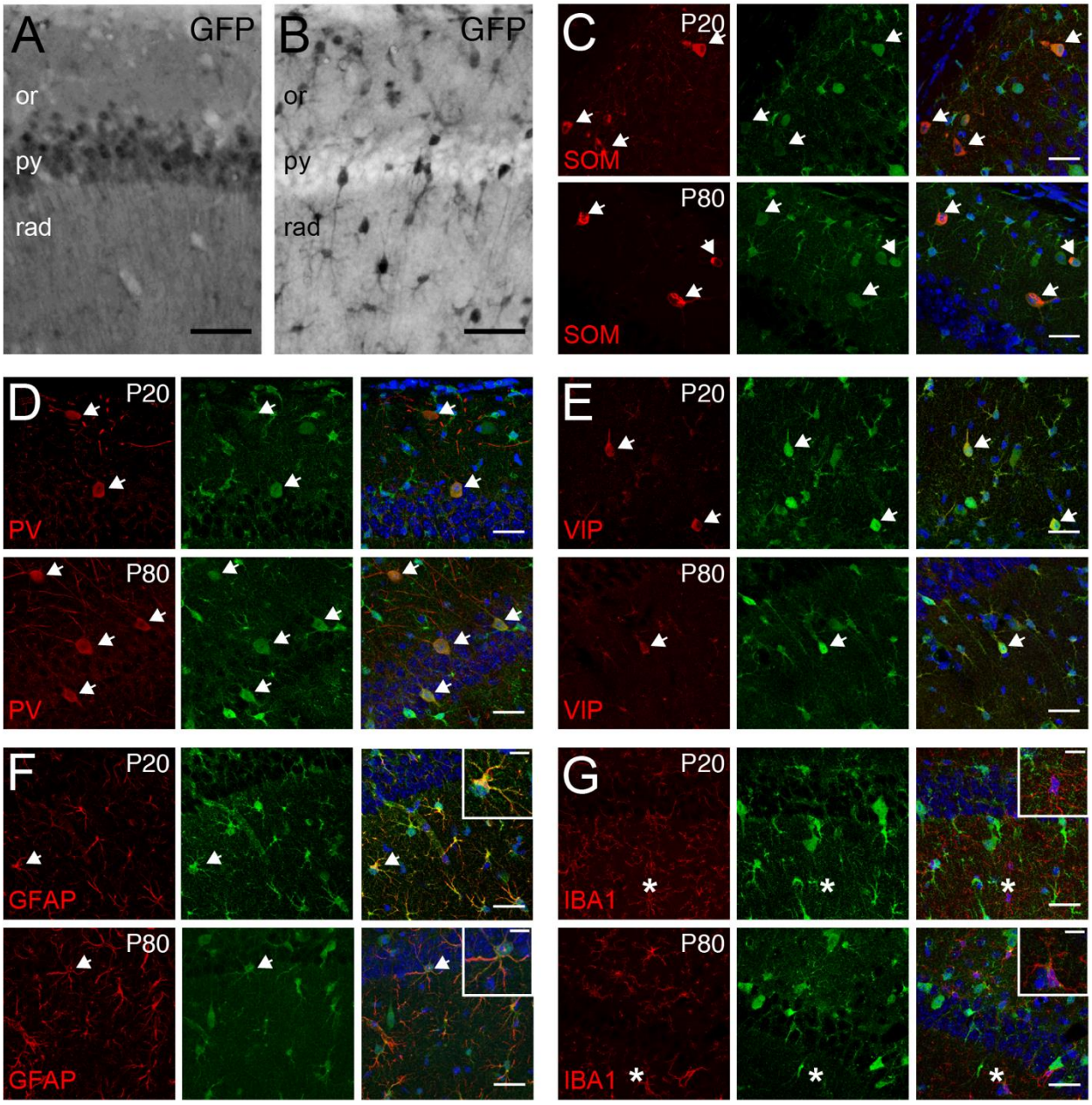

Figure 3. 7: Pyramidal cells, GABAergic interneurons, and astrocytes express TCF4 in the hippocampus.

(**A, B**) DAB immunostaining of GFP (for TCF4) in the CA1 of P80 *LGSL::Gad2-cre* or *LGSL::Nex-cre* mice. Both pyramidal layer cells and GABAergic cells express TCF4. Scale bars = 0.5 mm. (**C-E**) Dual immunostaining of interneuron subtype-specific

markers, SOM, PV, or VIP, and GFP (for TCF4) in P20 and P80 *LGSL::Nex-cre* mice. TCF4 is expressed nearly all SOM-, PV-, or VIP-positive interneurons (arrows). (**F, G**) Dual immunostaining of GFAP or IBA1, and GFP (for TCF4) in P20 and P80 *LGSL::Nex-cre* mice. GFAP-labeled cells express GFP (arrow), but IBA1-labeled cells do not express GFP (asterisks). Scale bars = 30 or 10 μm for higher magnification insets.

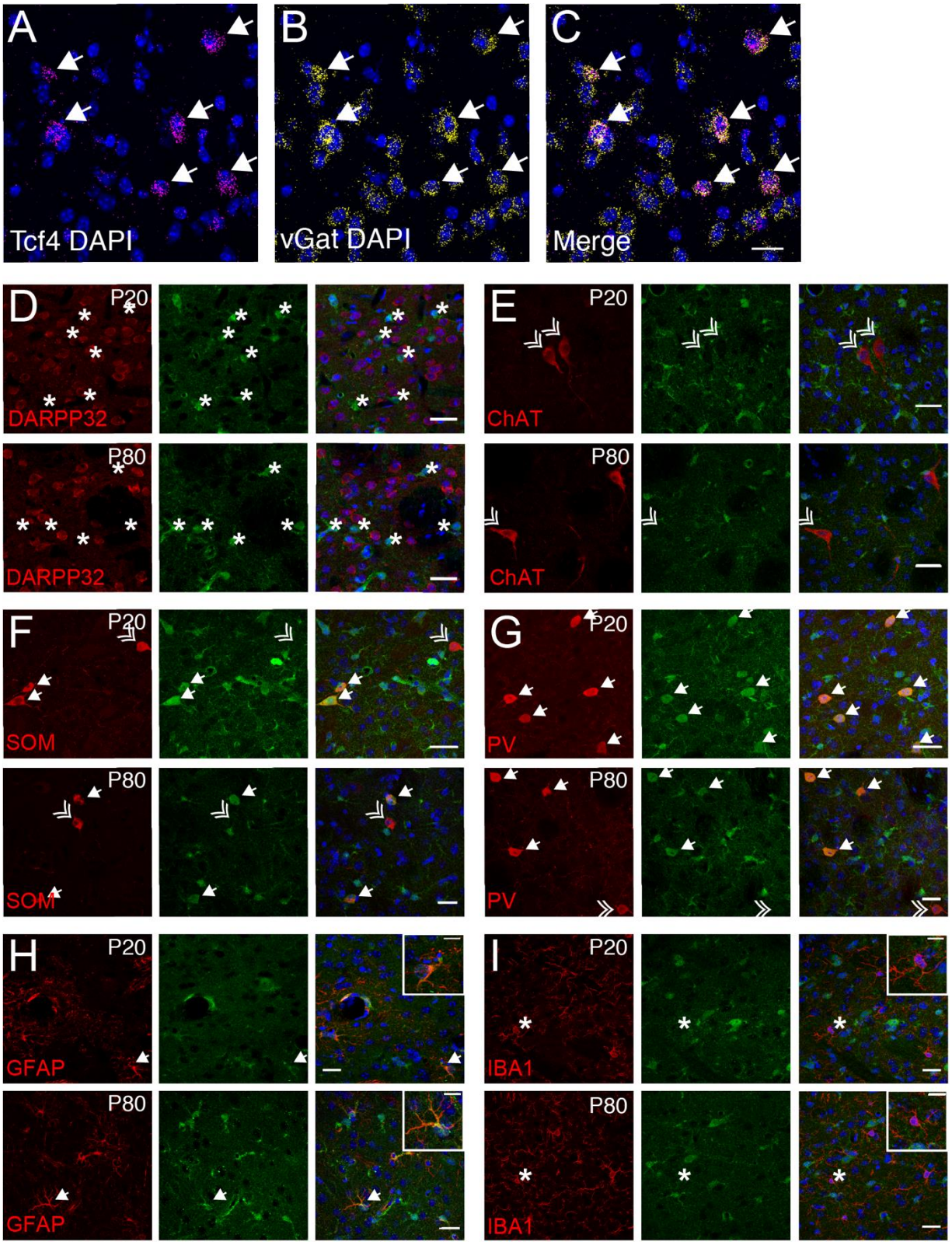

Figure 3. 8: Striatal interneurons, but not medium spiny neurons, express TCF4.

(**A-C**) Representative ISH images for *Tcf4* and *vGat* from adult WT striatum, showing that specific subtypes of interneurons express *Tcf4* (arrows). Scale bar = 20 µm. (**D-G**) Dual immunostaining of DARPP32, ChAT, SOM, or PV and GFP (for TCF4) in P20 and P80 *Tcf4*$^{LGSL/+}$ mice. The representative staining images reveal that SOM- and PV-positive subtype interneurons express TCF4 (arrow). Asterisks represent only GFP-positive neurons. Double arrows represent interneuron subtypes that do not express GFP. Scale bars = 20 µm. (**H, I**) Dual immunostaining of GFAP or IBA1, and GFP (for TCF4) in P20 and P80 Tcf4$^{LGSL/+}$ mice. GFAP-labeled cells express GFP (arrow), but IBA1-labeled cells do not express GFP (asterisk). Scale bars = 30 or 10 µm for higher magnification insets.

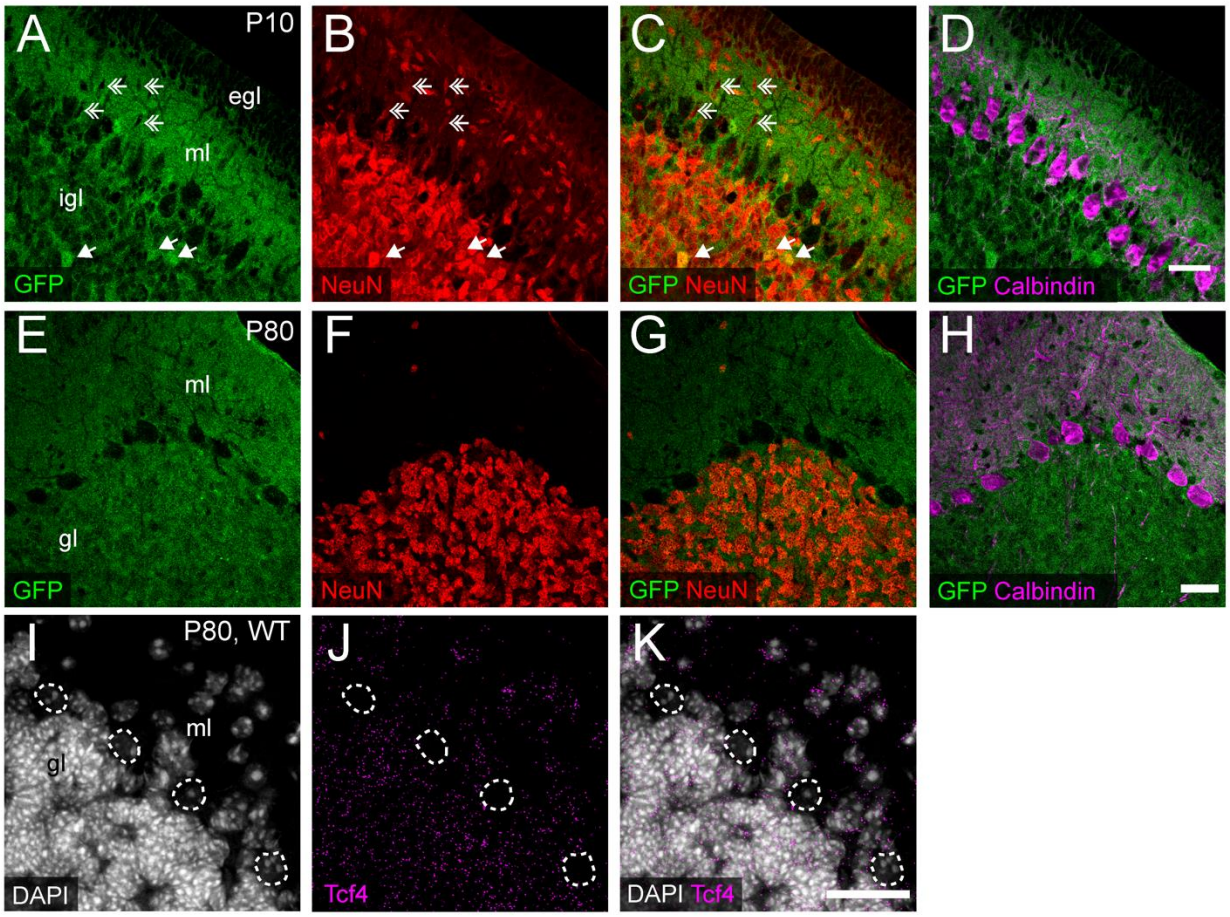

Figure 3. 9: Cerebellar granule and molecular layer cells, but not Purkinje cells, express TCF4.

(**A-H**) Triple immunostaining of GFP (for TCF4), NeuN, and Purkinje cell marker, calbindin, in P20 and P80 *Tcf4*$^{LGSL/+}$ mouse cerebellum. The representative images confirm that migrating NeuN-positive granule cells in the molecular layer (ml) lack TCF4 (double arrows), and post-migratory granule cells in the inner granule layer (igl) express TCF4 (arrows). Purkinje cells do not express TCF4. egl = External granule layer. (**I-K**) Representative ISH images for *Tcf4* and DAPI in WT adult cerebellum, showing that *Tcf4* mRNA is present in granule and molecular layer (gl and ml) cell nuclei, but it is absent in Purkinje cell nuclei (dashed line). Scale bars = 30 µm.

Antigen	Immunogen	Manufacturer	Dilution
APC	Recombinant peptide corresponding to a.a. 1-226 of APC	Millipore (Bilerica, MA), mouse monoclonal, clone CC-1, OP80	1:500
Calbindin	Peptide corresponding to C-terminus of Calbindin D28K of human origin	Santa Cruz (Dallas, TX), goat polyclonal, sc-7691	1:500
ChAT	Human placental enzyme	Millipore, goat polyclonal, AB144P	1:1,000
DARPP-32	Peptide corresponding to a.a. 20-40 of mouse DARPP-32	Millipore, rabbit polyclonal, AB10518	1:1,000
GAPDH	GAPDH purified from rabbit muscle	Millipore, mouse monoclonal, clone 6C5, MAB374	1:5,000
GFAP	GFAP purified from cow spinal cord	Dako (Glostrup, Denmark), rabbit polyclonal, Z0334	1:1,000
GFP	The full length a.a. 246 from the jellyfish Aequorea victoria	Novus (Centennial, CO), rabbit polyclonal, NB600-308	1:1,000
GFP	Purified recombinant GFP	Aves Labs (Tigard, OR), chicken polyclonal, GFP-1020	1:10,000
IBA1	Synthetic peptide corresponding to the C-terminus of rat Iba1 (aa 134-147)	Wako (Osaka, Japan), rabbit polyclonal, 019-19741	1:500
NeuN	Purified nuclei from mouse brain	Millipore, mouse monoclonal, clone A60, MAB377	1:1,000
Olig2	Recombinant mouse Olig2	Millipore, rabbit polyclonal, AB9610	1:1,000
PV	Parvalbumin purified from mouse carp muscles	Swant (Marly, Switzerland), mouse monoclonal, PV235	1:1,000
SOM	Synthetic peptide corresponding to somatostatin	Peninsula Laboratories (San Carlos, CA), rabbit polyclonal, T-4103	1:1,000
TCF4	Mouse TCF-4 a.a. 50-150 conjugated to keyhole limpet haemocyanin	Abcam (Cambridge, United Kingdom), rabbit polyclonal, ab130014	1:500 or 1,000
VIP	Synthetic VIP coupled to bovine thyroglobulin with carbodiimide linker	Immunostar (Hudson, WI), rabbit polyclonal, 20077	1:1,000

Table 3. 1 Primary antibodies used in this chapter.

Abbreviation	Full name
ACB	Nucleus accumbens
BLA	Basolateral amygdalar nucleus
CA1	Cornu ammonis1
CA3	Cornu ammonis3
CBX	Cerebellum
CC	Corpus callosum
CEA	Central amygdalar nucleus
CLA	Claustrum
CP	Caudate putamen
CRX	Cortex
CS	Superior central nucleus raphe
egl	External granule layer of cerebellum
gl	Granule layer of cerebellum
gm	Glomerular layer of olfactory bulb
gr	Granule layer of olfactory bulb
HY	Hypothalamus
igl	Inner granule layer of cerebellum
MB	Midbrain
MEA	Medial amygdalar nucleus
MH	Meidal habenula
ml	Molecular layer of cerebellum
MM	Medial mammillary nucleus
MS	Medial septal nucleus
NDB	Diagonal band nucleus
OLF	Olfactory bulb
PAG	Periaqueductal gray
PFC	Prefrontal cortex
PG	Pontine gray
PIR	Piriform area
pl	Plexiform layer of olfactory bulb
PRP	Nucleus prepositus
SC	Superior colliculus
SPV	Spinal nucleus of the trigeminal
STR	Striatum
TH	Thalamus
VNC	Vestibular nuclei
ZI	Zona incerta

Table 3. 2 Abbreviation list of the mouse brain areas

CHAPTER 4: CELL-TYPE SPECIFIC RESTORATION OF *TCF4* REVEALS CELL TYPES THAT HAVE THE LARGEST IMPACT ON BEHAVIORAL RECOVERY

4.1 Introduction

Any *Tcf4* gene normalization strategy requires an understanding of the cell types relevant to pathophysiology that underlies PTHS. For example, viral-mediated gene delivery can target discrete cell types by promoter choice (68, 71), providing a capacity to adjust *Tcf4* expression in a cell type-specific manner. TCF4 is present in excitatory and inhibitory neurons of the forebrain. Moreover, single-cell transcriptomic studies in the neonatal and adult mouse brain indicate that *Tcf4* transcript levels are higher in excitatory and inhibitory neurons than most other cell types (**Fig. 4.1**) (112, 113). The electrophysiological experiments reveal abnormal intrinsic excitability in *Tcf4* deficient excitatory neurons of the prefrontal cortex and hippocampus (28, 56), suggesting that PTHS-associated pathology could benefit from reactivating *Tcf4* expression in excitatory or inhibitory neurons. Here I explored whether embryonic *Tcf4* reinstatement selectively in excitatory or inhibitory neurons rescued behavioral phenotypes in PTHS model mice. Before exploring this possibility, I first validated my approach by demonstrating that embryonic pan-cellular reinstatement of *Tcf4* expression could fully prevent PTHS-associated phenotypes. Then I reactivated *Tcf4* expression selectively in forebrain glutamatergic neurons or GABAergic neurons to analyze behavioral outcomes of cell type-specific *Tcf4* reinstatement.

4.2 Results

4.2.1 Pan-cellular embryonic reinstatement of *Tcf4* fully rescues behavioral phenotypes in a PTHS mouse model

I used the *Tcf4* conditional mouse model of PTHS (*Tcf4*$^{LGSL/+}$ is now indicated as *Tcf4*$^{STOP/+}$ in this and following chapter) in which a STOP cassette and GFP reporter, flanked by loxP sites, were inserted upstream of the critical bHLH DNA binding domain in exon 18 of *Tcf4* (**Fig. 4.2A**). As predicted from my design, the level of exon 18-containing *Tcf4* mRNA was reduced by half in *Tcf4*$^{STOP/+}$ mouse brain compared to *Tcf4*$^{+/+}$ (wildtype control) mouse brain (**Fig. 4.2B**, *Tcf4*$^{+/+}$: 1.0 ± 0.06, n = 4; *Tcf4*$^{STOP/+}$: 0.56 ± 0.05, n = 4). To produce embryonic, pan-cellular reinstatement of *Tcf4*, I crossed *Tcf4*$^{STOP/+}$ mice to transgenic mice expressing Cre under the β-Actin promoter (*Tcf4*$^{STOP/+}$*::Actin-Cre*). As an initial validation, I stained for the GFP reporter in sagittal brain sections from *Tcf4*$^{+/+}$, *Tcf4*$^{STOP/+}$, and *Tcf4*$^{STOP/+}$*::Actin-Cre* mice. GFP signal, a proxy for presence of the STOP cassette, was detected throughout the sagittal sections of *Tcf4*$^{STOP/+}$ mouse brain. However, GFP was not detected in brain sections from *Tcf4*$^{+/+}$ or *Tcf4*$^{STOP/+}$*::Actin-Cre* mice, indicating efficient excision of the GFP-STOP cassette in these mice (**Fig. 4.2C**). To demonstrate the consequences of pan-cellular embryonic *Tcf4* reinstatement in PTHS model mice, I studied a variety of physiological and behavioral phenotypes in control (*Tcf4*$^{+/+}$ and *Tcf4*$^{+/+}$*::Actin-Cre*), PTHS model (*Tcf4*$^{STOP/+}$), and reinstatement model (*Tcf4*$^{STOP/+}$*::Actin-Cre*) mice. Male and female *Tcf4*$^{STOP/+}$ mice had reduced body and brain weights, whereas *Tcf4*$^{STOP/+}$*::Actin-Cre* mice had similar body and brain weights as their littermate controls (**Fig. 4.3A-B**). This suggests that embryonic reinstatement of *Tcf4* expression could prevent microcephaly

in PTHS model mice. To study whether long-term memory deficits could be prevented, I examined interaction time of identical objects, with one object located in the familiar position and the other in a novel position. I found that *Tcf4*$^{STOP/+}$ mice had similar interaction time with objects located in the familiar and novel positions, suggesting the inability to remember the previously-presented location of the object and suggestive of long-term memory deficits (**Fig. 4.2D**). In contrast, *Tcf4*$^{STOP/+}$*::Actin-Cre* and control mice interacted with the object located in the novel position more than the object located in the familiar position, suggesting normal long-term memory function (**Fig. 4.2D**). I then assessed locomotor and exploration activity by the open field test and found that *Tcf4*$^{STOP/+}$ mice showed increased activity and total distance travelled, while *Tcf4*$^{STOP/+}$*::Actin-Cre* mice showed similar activity levels to controls (**Fig. 4.2E**). I also examined nest building, an innate, goal-directed behavior achieved by pulling, carrying, fraying, push digging, sorting, and fluffing of nest material (114). *Tcf4*$^{STOP/+}$ mice exhibited poor performance in the nest building task over the 4-day testing period, using roughly half the nest material used by control and *Tcf4*$^{STOP/+}$*::Actin-Cre* (**Fig. 4.2F**). To assess anxiety-like behavior, I evaluated mice in the elevated plus maze task and found that *Tcf4*$^{STOP/+}$ mice spent similar time in the closed and open arms, while control and *Tcf4*$^{STOP/+}$*::Actin-Cre* mice spent proportionally more time in the closed arms (**Fig. 4.2G**). Collectively, my results confirm that *Tcf4*$^{STOP/+}$ mice exhibit physiological and behavioral deficits like those observed in other mouse models of PTHS (54, 56), demonstrating the efficacy of the transcriptional STOP cassette in blocking TCF4 function. Moreover, these data show that *Tcf4* reinstatement upon embryonic Cre-

mediated excision of the STOP cassette can fully prevent the emergence of physiological and behavioral deficits associated with *Tcf4* haploinsufficiency.

4.2.2 *Tcf4* reinstatement in glutamatergic or GABAergic neurons rescues selective behavioral phenotypes in PTHS model mice

PTHS-associated pathologies might be effectively treated by preferentially reactivating Tcf4 expression in excitatory and inhibitory neurons. To explore this possibility, and whether these broad neuronal subclasses contribute to PTHS phenotypes in a modular or cooperative fashion (or both) in the case of Tcf4 haploinsufficiency, we crossed *Tcf4*$^{STOP/+}$ mice to *Nex-Cre*$^{+/-}$ or *Gad2-Cre*$^{+/-}$ to reactivate Tcf4 expression selectively in forebrain glutamatergic neurons (*Tcf4*$^{STOP/+}$*::Nex-Cre*) or GABAergic neurons (*Tcf4*$^{STOP/+}$*::Gad2-Cre* mice) (**Fig. 4.4A**). Then I analyzed behavioral performance in these mice. In the open field test, I found that *Tcf4*$^{STOP/+}$*::Nex-Cre* mice exhibited significantly higher activity levels than control mice (*Tcf4*$^{+/+}$ and *Tcf4*$^{+/+}$*::Nex-Cre*), indicating that embryonic reinstatement of *Tcf4* in forebrain glutamatergic neurons failed to rescue the hyperactivity phenotype (**Fig. 4.4B**). Activity levels in *Tcf4*$^{STOP/+}$*::Gad2-Cre* mice were statistically indistinguishable from either control mice (*Tcf4*$^{+/+}$ and *Tcf4*$^{+/+}$*::Gad2-Cre)* or *Tcf4*$^{STOP/+}$ mice (**Fig. 4.4B**), suggesting that embryonic *Tcf4* reinstatement in GABAergic neurons is also insufficient to fully prevent the hyperactivity phenotype. *Tcf4* reinstatement in glutamatergic neurons improved object location memory functions, whereas *Tcf4* reinstatement in GABAergic neurons failed to fully prevent location memory impairments (**Fig. 4.4C**). Lack of improvement in activity level and object location memory function from

Tcf4$^{STOP/+}$*::Gad2-Cre* mice was reproduced by an independent investigator (**Fig. 4.5**), which increases reliability of the study. In the elevated plus maze task, I found that *Tcf4*$^{STOP/+}$*::Nex-Cre* and control mice exhibited increased closed arm activity compared to *Tcf4*$^{STOP/+}$ mice, showing that reinstating *Tcf4* in glutamatergic neurons restored normal anxiety-like behavior (**Fig. 4.4D**). In contrast, *Tcf4*$^{STOP/+}$*::Gad2-Cre* and *Tcf4*$^{STOP/+}$ mice exhibited reduced closed arm activity compared to controls (**Fig. 4.4D**), suggesting that the reduced anxiety-like phenotype persisted despite reinstatement of *Tcf4* in GABAergic neurons. Finally, I observed that both *Tcf4*$^{STOP/+}$*::Nex-Cre* and *Tcf4*$^{STOP/+}$*::Gad2-Cre* mice used the similar amount of nest materials as their respective controls (**Fig. 4.4E**), demonstrating that embryonic reinstatement in either glutamatergic or GABAergic neurons was sufficient to prevent the impaired nest building phenotype in PTHS model mice. My findings suggest that normalizing *Tcf4* expression from both glutamatergic and GABAergic neurons or either of the neuronal classes along with other non-neuronal cell types might be required to rescue all behavioral phenotypes.

4.3 Discussion

An important consideration for eventual genetic therapies is which cell types, if render fully functional, have the impact on rescuing behavioral phenotypes. However, the therapeutic potential of genetic rescue in specific cell types has never been evaluated due to the lack of conditional models for *Tcf4* reinstatement. The conditional restoration model has provided a powerful tool in that I can establish the impact of cell type-specific *Tcf4* restoration on the cellular and behavioral context, which will ultimately inform therapeutic development for PTHS. Because *Tcf4* is particularly expressed at the

high level in glutamatergic and GABAergic neurons during embryonic development and throughout the postnatal period (26), I initially aimed to embryonically reinstate TCF4 function in each neuronal type to establish their relative contribution to behavioral rescue. Reactivating Tcf4 expression in excitatory pyramidal neurons, dentate gyrus mossy cells, and granule cells within the dorsal telencephalon, starting from E11.5, improved memory, anxiety phenotype, and innate behavior, while reactivating Tcf4 expression in almost all GABAergic neurons throughout the brain at ~E13.5 rescued only abnormal innate behavior. Hyperactivity phenotype was not rescued by reinstating *Tcf4* from either of the neuronal classes, indicating that normal TCF4 function from both neuronal classes may be required for locomotor and exploration activity. These data suggest that TCF4 in both neuronal types contribute to behavioral outcomes, and therapeutic strategies should thus target the normalization of *Tcf4* expression in both GABAergic and glutamatergic neurons. However, we cannot rule out the possibility of gaining phenotypic rescue by reinstating *Tcf4* from other cell types such as oligodendrocytes in which the loss of TCF4 has been shown to contribute to PTHS pathophysiology (29).

4.4 Materials and Methods

Mice

The generation of $Tcf4^{STOP/+}$ (= $Tcf4^{LGSL/+}$) knock-in mice has been described in Chapter 3. Mice carrying *loxP-GFP-STOP-loxP* allele were maintained on a congenic C57BL/6J background. The female $Tcf4^{STOP/+}$ mice were mated with heterozygous males from one of three *Cre*-expressing lines: *Nex-Cre*$^{+/-}$ (81), which Klaus-Armin Nave

generously provided, Gad2-Cre$^{+/-}$ (RRID:IMSR_JAX:010802), or Actin-Cre$^{+/-}$ (RRID:IMSR_JAX:019099). All mice were maintained on a 12:12 light-dark cycle with *ad libitum* access to food and water. I used male and female littermates at equivalent genotypic ratios. All research procedures using mice were approved by the Institutional Animal Care and Use Committee at the University of North Carolina at Chapel Hill and conformed to National Institutes of Health guidelines.

Calculation of Tcf4 expression from public single-cell sequencing data

Single-cell transcriptomic data from the neonatal mouse cortex (112) and the adult mouse nervous system (113) were obtained from GEO accession GSE123335 and from http://mousebrain.org/downloads.html, respectively. For the neonatal cortex data, the mean and standard error of *Tcf4* expression values were computed across all cells of a given annotated cell type in R and plotted using ggplot2. For adult data, I focused just on cell types annotated as deriving from cortex, amygdala, telencephalon, CNS, dentate gyrus, hippocampus, olfactory bulb, brain, cerebellum, or striatum. I then grouped similar cell types into broader classifications. For example, all clusters annotated as glutamatergic (GLU) were renamed as “Excitatory neuron”. I then computed the mean and standard error of *Tcf4* expression for each broader cell type within each brain region in R and plotted using ggplot2. All code to reproduce the plots for the figure 2 is provided at https://github.com/jeremymsimon/Kim_TCF4.

Tissue preparation

Mice were anesthetized with sodium pentobarbital (60 mg/kg, intraperitoneal injection) before transcranial perfusion with 25 ml of PBS immediately followed by phosphate-buffered 4% paraformaldehyde (pH 7.4). Brains were postfixed overnight at 4°C before 24-hour incubations in PBS with 30% sucrose. Brains were sectioned coronally or sagittaly at 40 mm using a freezing sliding microtome (Thermo Scientific). Sections were stored at -20°C in a cryo-preservative solution (45% PBS, 30% ethylene glycol, and 25% glycerol by volume).

Immunohistochemistry

For chromogenic staining, sections were rinsed several times with PBS, and endogenous peroxidases were quenched by incubating for 5 mins in 1.0% H_2O_2 in MeOH, followed by PBS rinsing. Sections were washed with PBST several times. Then sections were blocked with 5% NGST for 1 hour at RT. Blocked sections were incubated in primary antibody, rabbit anti-GFP (NB600-308) diluted 1:1000 in NGST for 24 hours at 4°C. After incubation in primary antibodies, sections were rinsed several times in PBST and incubated for 1 hour at RT in biotinylated goat anti-rabbit secondary antibodies (Vector BA-1000, Burlingame, CA) diluted 1:500 in NGST. Sections were then rinsed in PBST prior to tertiary amplification for 1 hour with the ABC elite avidin-biotin-peroxidase system (Vector PK-7100). Further rinsing with PBST preceded a 3-minute incubation at RT in 3’3’-diaminobenzidine (DAB) chromogenic substrate (0.02% DAB and 0.01% H_2O_2 in PBST) to visualize immune complexes amplified by avidin-biotin-peroxidase.

Behavioral testing and analyses

Object location memory: Mice were habituated to an open box, containing a visual cue on one side, without objects for 5 minutes each day for 3 days. In the following day, mice were trained with two identical objects for 10 minutes. After 24 hours, mice were placed in the box where one of the objects was relocated to a novel position for 5 minutes. Video was recorded during each period. Interaction time of a mouse with each object was measured by Ethovision XT 15.0 program (Noldus). A percentage of the exploration time with the object in a novel position (% in novel location) was calculated as follows: (time exploring novel location)/(time exploring novel location + familiar location) * 100. If total exploration time was less than 2 seconds, these mice were excluded from the dataset.

Open field (Fig. 4.2): Mice were given a 30-min trial in an open-field chamber (41 x 41 x 30 cm) that was crossed by a grid of photobeams (VereMax system, Accuscan Instruments). Counts were taken of the number of photobeams broken during the trial in 5-min intervals. Total distance traveled was measured over the course of the 30-min trial.

Open field (Fig. 4.3): Mice were given a 30-min trial in an open-field chamber (40 x 40 x 30 cm). Mouse movements were recorded with a video camera, and the total distance traveled was measured by Ethovision XT 15.0 program.

Elevated plus maze: The elevated plus maze was constructed to have two open arms and two closed arms; all arms are 20 cm in length and 8 cm in width. The maze was elevated 50 cm above the floor. Mice were placed on the center section and allowed to explore the maze for 5 minutes. Mouse movements on the maze were recorded with a

video camera. Activity level (time and entry) in open or closed arms was measured by Ethovision XT 15.0 program.

Nest building: Mice were single-housed for a period of 3 days before the start of the assay. On day 1, 10-11 g of compressed extra-thick blot filter paper (1703966, Bio-Rad), cut into 8 evenly sized rectangles, was placed in a cage. In each day, for 4 consecutive days (**Fig. 4.2**), the amount of paper not incorporated into a nest was weighed. For **Fig. 4.3**, additional measurement of nest material was recorded 72 hours after collecting data for 4 consecutive days.

Statistical analysis

Welch's one-way analysis of variance (ANOVA) followed by Dunnett's *post hoc* test was performed for object location memory task and open field (total distance) (**Fig. 4.2**). One-way ANOVA followed by Bonferroni's *post hoc* was carried out for object location memory task and open field (total distance) (**Fig. 4.3**). Two-way ANOVA followed by Tukey's *post hoc* was conducted for elevated plus maze and nest building (% material used). All values are expressed as means ± standard error of the mean (SEM). Asterisks indicate *P* values: **P* < 0.05, ***P* < 0.005, ****P* < 0.001, *****P* < 0.0001. GraphPad Prism 9.1.1 software (GraphPad Software) was used for all statistical analyses.

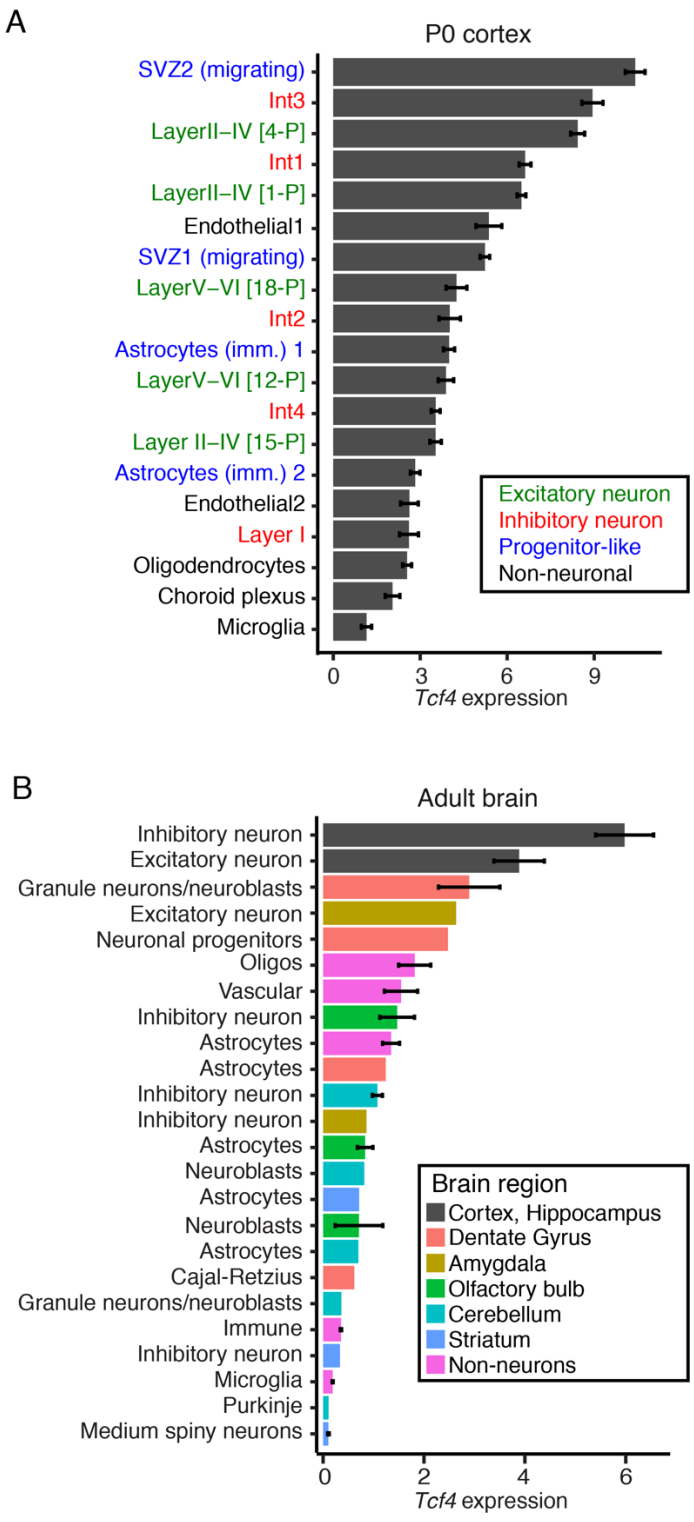

Figure 4. 1: Single-cell RNA sequencing reveals cell type-specific *Tcf4* expression in the neonatal and adult mouse brain.

(**A**) Average expression of *Tcf4* in 19 cell types identified in the P0 cortex [data analyzed from reference (112)]. Cell type names are colored by principal cell classifications. (**B**) Average expression of *Tcf4* in cell types identified in the adult mouse brain [data analyzed from referece (113)]. Bars are colored by brain region, and clusters were aggregated into principal cell types. Values are means ± SEM.

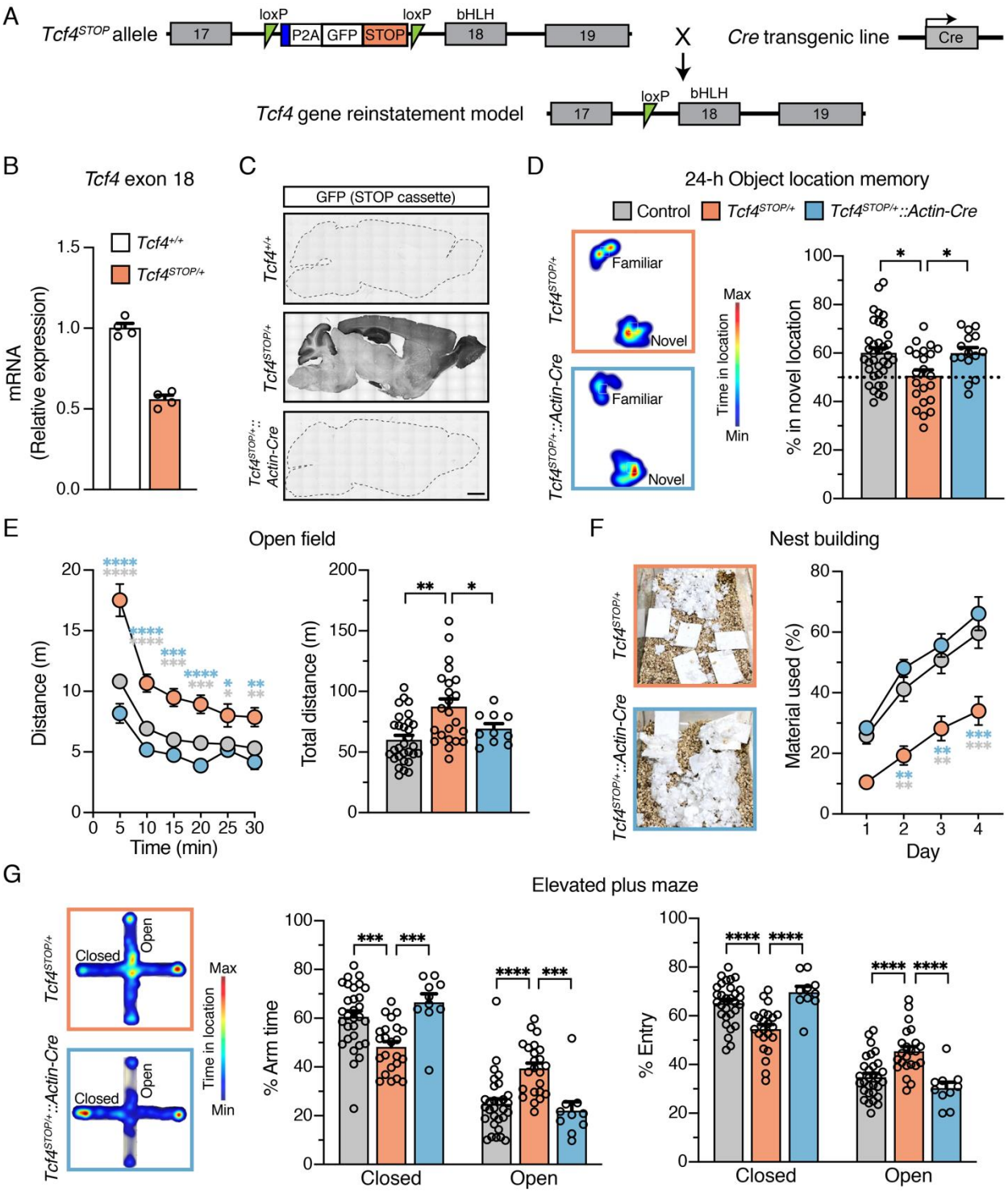

Figure 4. 2: Embryonic, pan-cellular reinstatement of *Tcf4* fully rescues behavioral deficits in a mouse model of Pitt-Hopkins syndrome.

(**A**) Schematic depicting a conditional Pitt-Hopkins syndrome mouse model in which expression of the bHLH region of *Tcf4* is prevented by the insertion of a floxed GFP-STOP cassette into intron 17 of *Tcf4* (*Tcf4*$^{STOP/+}$). Crossing *Tcf4*$^{STOP/+}$ mice with *Actin-Cre*$^{+/-}$ transgenic mice can produce mice with embryonic pan-cellular reinstatement of *Tcf4* expression (*Tcf4*$^{STOP/+}$*::Actin-Cre*). (**B**) Relative *Tcf4* mRNA expression from *Tcf4*$^{+/+}$ and *Tcf4*$^{STOP/+}$ brains. (**C**) DAB immunostaining of GFP (indicating presence of the STOP cassette) in sagittal brain sections of adult *Tcf4*$^{+/+}$, *Tcf4*$^{STOP/+}$, and *Tcf4*$^{STOP/+}$*::Actin-Cre* mice. Scale bar = 1 mm. (**D**) Left panel: Heatmaps indicate time spent in proximity to one object located in the familiar position and the other object relocated to the novel position. Right panel: Percent time interacting with the novel location object. (**E**) Left panel: Distance traveled per 5 min. Right panel: Total distance traveled for the 30-min testing period. (**F**) Left panel: Representative images of nests built by *Tcf4*$^{STOP/+}$ and *Tcf4*$^{STOP/+}$*::Actin-Cre* mice. Right panel: Percentage of nest material used during the 4-day nest building period. (**G**) Left panel: Heatmaps reveal relative time spent on the elevated plus maze. Right panels: Percent time spent in the closed and open arms and percent of entries made into the closed and open arms. All behavioral data were analyzed by Welch's ANOVA followed by Dunnett's *post hoc* or two-way ANOVA followed by Tukey's *post hoc*. Values are means ± SEM. *$p < 0.05$, **$p < 0.005$, ***$p < 0.001$, ****$p < 0.0001$.

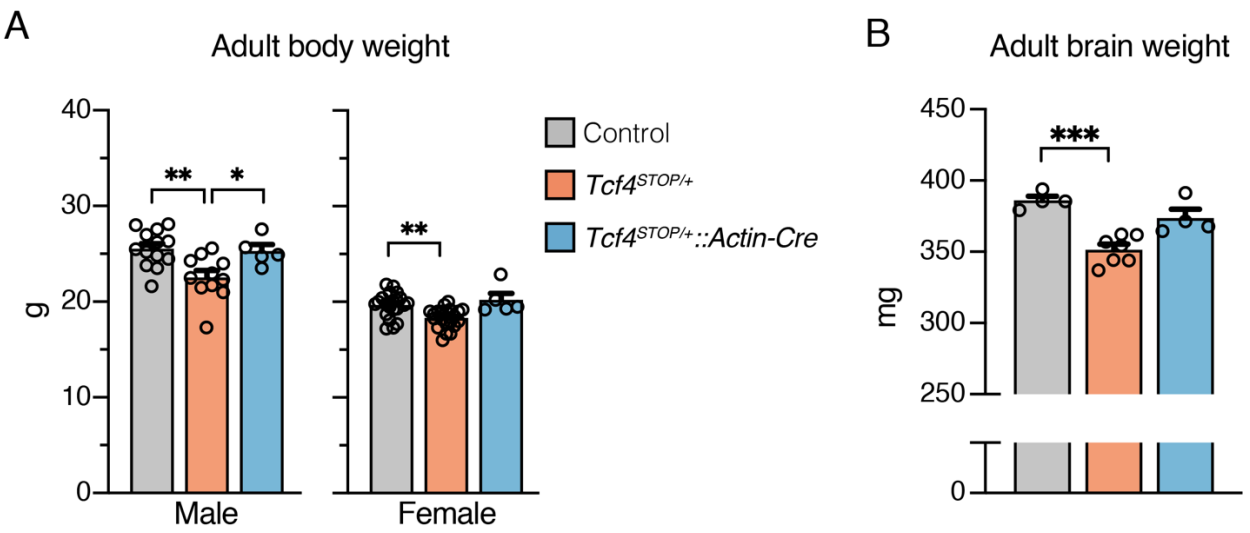

Figure 4. 3: Body and brain weight analysis.

(**A**) Adult male and female body weights of each genotypic group. (**B**) Adult brain weight measured from dissected brains. All data were analyzed by Welch's ANOVA followed by Dunnett's *post hoc*. Values are means ± SEM. *p < 0.05, **p < 0.005, ***p < 0.001.

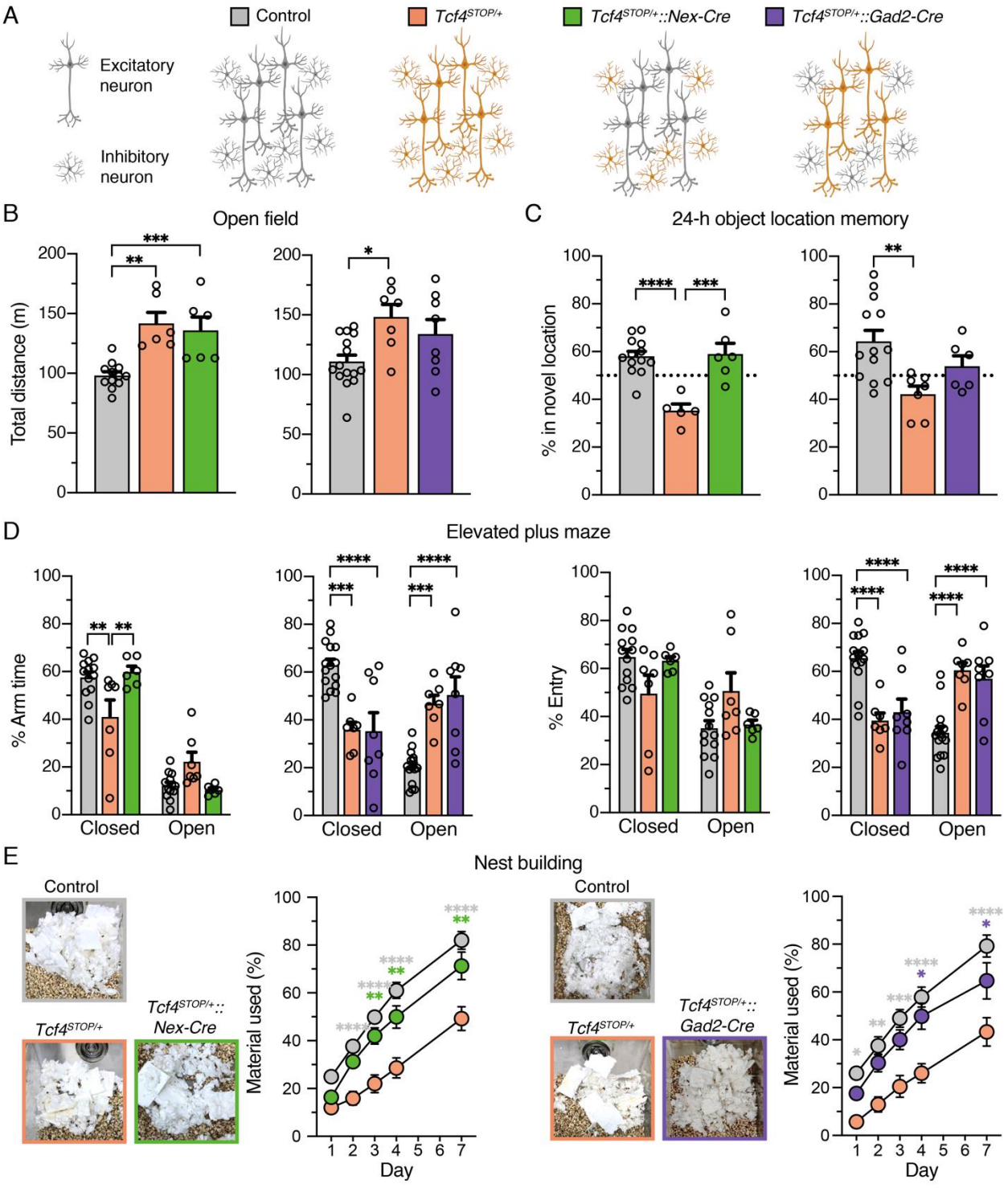

Figure 4. 4: Embryonic reinstatement of *Tcf4* expression in glutamatergic or GABAergic neurons rescues selective behavioral deficits in a mouse model of PTHS.

(**A**) Schematic representation of cell type-specific *Tcf4* reinstatement strategy. *Tcf4*$^{STOP/+}$*::Nex-Cre* or *Tcf4*$^{STOP/+}$*::Gad2-Cre* mice normalize *Tcf4* expression in glutamatergic or GABAergic neurons, respectively, while controls (*Tcf4*$^{+/+}$, *Nex-Cre*$^{+/-}$, or *Gad2-Cre*$^{+/-}$ mice) have normal *Tcf4* expression. (**B**) Total distance traveled for the 30-min testing period. (**C**) Percent time interacting with the novel location object. (**D**) Percent time spent in closed and open arms and percent entries made into the closed and open arms. (**E**) Representative images of nests built by mice and percentage of nest material used during the 7-day nest building period. All behavioral data were analyzed by one-way ANOVA followed by Bonferroni's *post hoc* or two-way ANOVA followed by Tukey's *post hoc*. Values are means ± SEM. *$p < 0.05$, **$p < 0.005$, ***$p < 0.001$, ****$p < 0.0001$.

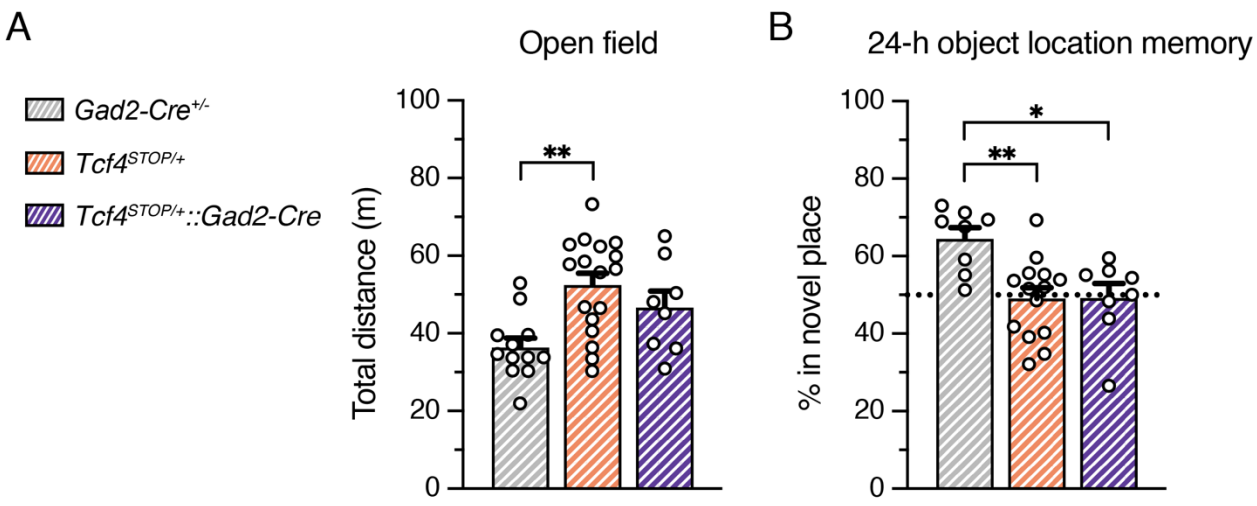

Figure 4. 5: Behavioral outcomes of *Tcf4$^{STOP/+}$::Gad2-Cre* mice were replicated by another investigator using independent data.

(**A**) Total distance traveled for the 30-min testing period. (**B**) Percent time interacting with the novel location object. Reinstating *Tcf4* from GABAergic neurons did not rescue hyperactivity and memory function deficit. All behavioral data were analyzed by one-way ANOVA followed by Bonferroni's *post hoc*. Values are means ± SEM. *$p < 0.05$, **$p < 0.005$

CHAPTER 5: POSTNATAL RESTORATION OF *TCF4* EXPRESSION RESCUES BEHAVIORAL AND ELECTROPHYSIOLOGICAL PHENOTYPES IN A MOUSE MODEL OF PITT-HOPKINS SYNDROME

5.1 Introduction

In principle, PTHS phenotypes could be prevented or corrected by normalizing *TCF4* gene expression levels, with the degree of efficacy likely impacted by the age and specificity of the intervention. A critical question that must be addressed prior to developing genetic normalization approaches for PTHS is whether behavioral phenotypes can be rescued if TCF4 expression is restored during postnatal development. This question is particularly intriguing given observations that TCF4/Tcf4 expression in the human/mouse brain peaks perinatally, before subsequently declining to basal levels that are sustained throughout adulthood (28, 29). Accordingly, I hypothesize that earlier interventions have a larger therapeutic impact on TCF4-linked disorders. Accordingly, I leveraged a conditional mouse model to establish the extent to which conditional reinstatement of Tcf4 expression could rescue behavioral phenotypes in a mouse model of PTHS. To accomplish postnatal reinstatement of *Tcf4* in the conditional PTHS model mice, I used an approach that modeled viral gene therapy, delivering Cre to neonates using the PHP.eB virus. After reinstating *Tcf4*, I tested for recovery using behavioral, electrophysiological, and biochemical assays. My data show that postnatal neuronal reinstatement of *Tcf4* expression fully or partially rescues behavioral and electrophysiological phenotypes in a mouse model of PTHS, providing evidence that genetic therapies might be feasible in individuals with PTHS.

5.2 Results

5.2.1 Neonatal ICV administration of PHP.eB-hSyn-Cre produces widespread Cre expression during postnatal brain development

I conducted experiments designed to mimic an eventual viral-mediated gene therapy for PTHS in an idealistic manner with respect to reintroducing wildtype *Tcf4* isoforms and expression levels. To this end, I packaged the Cre transgene expression cassette into a recombinant AAV9-derived PHP.eB vector and bilaterally delivered this viral vector to the cerebral ventricles of neonates (**Fig. 5.1A**). I expressed the Cre cassette under control of the human synapsin promoter (hSyn) for selective expression in neurons (**Fig. 5.2A**). I first examined expression of the Cre cassette as a proxy for the temporal and spatial biodistribution of *Tcf4* reinstatement following ICV injection of 1 µl of ~3.2 x 10^{10} vg AAV9/PHP.eB-hSyn-Cre on P1 (**Fig. 5.1A**). I failed to detect significant Cre signals from relatively medial sagittal sections of P4 and P7 mouse brain, despite being able to observe a local distribution of Cre-expressing cells in brain regions near the lateral ventricle injection site (**Fig. 5.1B-C** and **5-2B-C**). I detected a sparse distribution of Cre mRNA and protein across the forebrain by P10 (**Fig. 5.1B-C** and **5.2D**). Cre was visibly and more broadly expressed throughout all cortical layers by P17 (**Fig. 5.1B-C** and **5.2E**). The biodistribution of Cre protein at P60 was widespread in the brain, with particularly prominent expression in the forebrain compared to subcortical regions (**Fig. 5.1D-F**). My observation confirms that ICV injection is a suitable route of delivery for these studies, as it produces a viral biodistribution similar to pattern of endogenous TCF4 distribution (compare **Fig. 5.1D** and **4.2C**). To test whether Cre expression coincides with *Tcf4* reinstatement in *Tcf4*$^{STOP/+}$ mice, I examined the quantity

of full-length *Tcf4* mRNA transcripts upon delivery of PHP.eB/Cre to *Tcf4*$^{STOP/+}$ neonates. The RT-qPCR results confirmed increased relative expression of *Tcf4* transcripts from P10 and P17 *Tcf4*$^{STOP/+}$ brains treated with PHP.eB/Cre (**Fig. 5.1G**, *Tcf4*$^{STOP/+}$ + Vehicle at P10: 1.0 ± 0.0, n = 2; *Tcf4*$^{STOP/+}$ + PHP.eB/Cre at P10: 1.18 ± 0.03, n = 2, *Tcf4*$^{STOP/+}$ + Vehicle at P19: 1.0 ± 0.04, n = 3; *Tcf4*$^{STOP/+}$ + PHP.eB/Cre at P10: 1.37 ± 0.16, n = 2). Taken together, these findings establish the suitability of neonatal ICV injection of PHP.eB/Cre to examine the behavioral consequences of postnatal *Tcf4* reinstatement in a subset of neurons.

5.2.2 Postnatal reinstatement of *Tcf4* expression ameliorates behavioral performance in PTHS model mice

I analyzed the behavioral performance of adult (P60 - P110) *Tcf4*$^{+/+}$ and *Tcf4*$^{STOP/+}$ mice after delivering vehicle or PHP.eB/Cre at P1 (**Fig. 5.3A**). Similar to vehicle- or virally-treated *Tcf4*$^{+/+}$ mice, *Tcf4*$^{STOP/+}$ mice treated with PHP.eB/Cre exhibited normal activity levels in the open field test, whereas vehicle-treated *Tcf4*$^{STOP/+}$ mice were hyperactive (**Fig. 5.3B**). In addition to normalizing activity levels, treating PHP.eB/Cre improved long-term memory performance in *Tcf4*$^{STOP/+}$ mice compared to vehicle-treated *Tcf4*$^{STOP/+}$ mice (**Fig. 5.3C**). In the elevated plus maze, PHP.eB/Cre-treated *Tcf4*$^{STOP/+}$ mice spent relatively more time in the closed arms than the open arms, similar to vehicle- and PHP.eB/Cre-treated *Tcf4*$^{+/+}$ mice. In contrast, vehicle-treated *Tcf4*$^{STOP/+}$ mice spent similar time in the open and closed arms as a sign of their abnormally low anxiety levels (**Fig. 5.3D**). Lastly, I found that PHP.eB/Cre treatment progressively improved behavioral performance of *Tcf4*$^{STOP/+}$ mice in the nest building

task compared to vehicle-treated *Tcf4*$^{STOP/+}$ mice. Specifically, PHP.eB/Cre-treated *Tcf4*$^{STOP/+}$ mice incorporated nest materials at a similar level as vehicle- or virally-treated *Tcf4*$^{+/+}$ mice (**Fig. 5.3E**). While PHP.eB/Cre-mediated postnatal reinstatement of *Tcf4* recovered performance on a variety of behavioral phenotypes in PTHS model mice, I found that small body and brain sizes were not corrected by postnatally treating *Tcf4*$^{STOP/+}$ mice with PHP.eB/Cre (**Fig. 5.3F-G**). Collectively, a virally-mediated postnatal normalization of *Tcf4* expression can rescue behavioral phenotypes, while an earlier intervention and/or improved pan-cellular biodistribution might be necessary to recover certain physiological phenotypes.

5.2.3 Postnatal *Tcf4* reinstatement partially corrects local field potential abnormalities in PTHS model mice

Several clinical observations have reported electroencephalography (EEG) abnormalities, such as altered slow waves, in individuals with PTHS (9, 46, 115), yet these phenotypes have not yet been examined in PTHS model mice. Here I performed local field potential (LFP) recordings in the mouse model, which provide more accurate indication of local neuronal activity than traditional scalp EEG recordings (116). I implanted recording electrodes in the hippocampus, a site of high *Tcf4* expression (26), and recorded LFP from freely moving mice (**Fig. 5.4A** and **5.5A**). I observed a trend for reduced total power in *Tcf4*$^{STOP/+}$ mice, but the total power between *Tcf4*$^{+/+}$ and *Tcf4*$^{STOP/+}$ mice was not statistically distinguishable (**Fig. 5.4D**). A significant genotypic difference in LFP power was restricted to the theta (5-8 Hz) band (**Fig. 5.4E**). Spectrogram analysis revealed that a moderate but consistent decrease of power likely

contributed to overall reduction in theta power (**Fig. 5.4F**). Having established that *Tcf4* haploinsufficiency resulted in LFP abnormalities in mice, I sought to determine whether LFP power can be normalized by postnatal *Tcf4* reinstatement. I analyzed LFP recordings in vehicle- and virus-treated groups (**Fig. 5.5B-C**). Total LFP power was partially normalized in PHP.eB/Cre-treated *Tcf4*$^{STOP/+}$ mice, while it was significantly reduced in vehicle-treated *Tcf4*$^{STOP/+}$ mice compared to vehicle- and virally-treated *Tcf4*$^{+/+}$ mice (**Fig. 5.5D**). This effect appeared to be largely driven by a normalization of theta band activity (**Fig. 5.5E**), which is evident over time in a spectrographic analysis (**Fig. 5.5F**). Collectively, these data indicate that postnatal reinstatement of *Tcf4* can partially correct abnormal low frequency LFP activity observed in a PTHS mouse model.

5.2.4 Postmortem evaluation of *Cre* biodistribution and overall expression of *Tcf4* and *Tcf4*-regulated genes

The postmortem analysis could inform parameters for future preclinical studies. Accordingly, after completing behavioral and LFP experiments, I subjected the mice for ISH staining to characterize *Cre* distribution and for RT-qPCR to examine effectiveness of PHP.eB/Cre treatment on expression levels of *Tcf4* and *Tcf4*-regulated genes. ISH experiment revealed that *Cre* mRNA, delivered at P1, was still present in a 6-month-old mouse (**Fig. 5.6A-D**). In the cortex and olfactory bulb, *Cre* was observed in most cells, but certainly not all, throughout the layers (**Fig. 5.6C-D**). Similarly, I found the majority of cells expressing *Cre* in hippocampal pyramidal cells (**Fig. 5.6B**). This observation suggests that reinstating *Tcf4* in a subset of neurons can provide therapeutic benefit. To ensure that all treated *Tcf4*$^{STOP/+}$ mice had similar transduction efficiency with one

another, I analyzed *Cre* fluorescence levels in the neocortex and pyramidal cell layer of CA1 and found fluorescence levels to be comparable across treated mice except for one mouse whose levels were almost ~3-4 times higher than the group medians (**Fig. 5.6E**). To determine effectiveness of PHP.eB/Cre treatment on *Tcf4* mRNA expression, I analyzed *Tcf4* mRNA expression from the forebrain of the PHP.eB/Cre-treated *Tcf4*$^{STOP/+}$ mice. On average, *Tcf4* mRNA expression was approximately 1.3-fold higher in virally-treated *Tcf4*$^{STOP/+}$ mouse forebrain than vehicle-treated *Tcf4*$^{STOP/+}$ mouse forebrain at P150-P200 (**Fig. 5.6F**, *Tcf4*$^{+/+}$ + Vehicle: 1.0 ± 0.18, n = 15; *Tcf4*$^{STOP/+}$ + Vehicle: 0.56 ± 0.09, n = 14, *Tcf4*$^{STOP/+}$ + PHP.eB/Cre: 0.72 ± 0.12, n = 15). Recent RNA-sequencing studies revealed genes whose expression levels were altered by heterozygous *Tcf4* disruption (29, 54). To analyze the impact of PHP.eB/Cre treatment on the expression of *Tcf4*-regulated genes, I examined expression levels of the following genes: *Grin2a* (encoding for NMDA receptor subunit epsilon-1), *Mal* (encoding for myelin and lymphocyte protein), *Glra3* (encoding for glycine receptor subunit alpha-3), and *Lpar1* (lysophosphatidic acid receptor 1). Expression levels of those genes were noticeably downregulated in vehicle-treated *Tcf4*$^{STOP/+}$ mice, but partially normalized by treating *Tcf4*$^{STOP/+}$ mice with PHP.eB/Cre (**Fig. 5.6G**). My postmortem analyses confirm that neonatal PHP.eB/Cre treatment in *Tcf4*$^{STOP/+}$ mice partially normalized overall expression levels of the *Tcf4* transcripts and targeted genes. These expression data suggest that modestly increased *Tcf4* expression was sufficient to rescue behavioral phenotypes in *Tcf4*$^{STOP/+}$ mice.

5.3 Discussion

In this study, genetic reinstatement of *Tcf4* during early postnatal development achieved correction of multiple behavioral phenotypes in PTHS model mice, including hyperactivity, reduced anxiety-like behavior, memory function deficit, and abnormal innate behavior. Furthermore, early postnatal *Tcf4* reinstatement partially rescued hippocampal theta rhythm amplitude and, at the molecular level, expression levels of receptor genes (*Grin2a*, *Glra3*, and *Lpar1*) and a myelin gene (*Mal*). My results suggest that postnatal therapeutic efforts to compensate for loss-of-function of TCF4 can offer effective treatment strategy for PTHS.

One of the key parameters to optimize for genetic normalization strategies is the age at time of intervention. I likely accomplished widespread *Tcf4* normalization throughout the brain by P10-P17, which is equivalent to the first two years of human life (117). Individuals with PTHS have global developmental delay, often coming to attention in the first year of life (45). Thus, my study indicates that genetic normalization approaches could provide a viable early life treatment opportunity.

While it is important to intervene within a therapeutic window, eventual ASO or AAV-mediated genetic therapy will need to produce an appropriate biodistribution to be efficacious. Previous studies have shown that *Tcf4* expression levels are particularly high in the forebrain (26). Accordingly, my study employed a strategy to reinstate *Tcf4* expression more prominently in the forebrain than the subcortical region. Given the ability to recover behavioral phenotypes, future efforts to test the feasibility of ASOs or AAV-mediated gene transfer should target *Tcf4* reinstatement to the forebrain to provide therapeutic benefit.

A *TCF4* genetic normalization treatment strategy has the advantage in that it addresses the core genetic defect in PTHS, and therefore should restore transcriptional targets of TCF4. *Tcf4* haploinsufficiency altered the expression of genes that are involved in synaptic plasticity and neuronal excitability such as *Grin2a* and *Glra3* and neuronal development such as *Mal* and *Lpar1* (29, 54). My data show that upregulating *Tcf4* can correct the expression of these *Tcf4*-regulated genes. The effect of *Tcf4* normalization on its downstream genes might help to guide future preclinical studies. For example, therapeutic agent choice and dosing could be optimized both by testing behavioral recovery and by measuring expression of *Tcf4*-regulated genes, such as those validated in this study.

My study has four important limitations. First, I normalized *Tcf4* expression only in neurons. *Tcf4* is expressed in nearly all neurons, astrocytes, and oligodendrocytes (25, 26). Ideally, *Tcf4* should be reinstated in both neuronal and non-neuronal cells to accomplish maximum therapeutic outcomes. Unfortunately, my preliminary data indicated that injecting AAV containing a broadly active promoter, CAG, reinstated *Tcf4* in all cell types, but induced severe weight loss and abnormal glial activation in mice (data not shown), similar toxicity observed in another study (118). To avoid toxicity in my experimental paradigm while still achieving efficient transduction, I was limited to using a neuron-selective promoter (hSyn) in the viral construct. Nonetheless, my data provide compelling evidence that reinstating *Tcf4* only in neurons is sufficient to reverse behavioral and LFP phenotypes in PTHS model mice. Second, my study does not inform therapeutic threshold that must be achieved by genetic normalization approaches. TCF4 is a dosage-sensitive protein: too little expression causes

neurodevelopmental disorders, and too much expression appears to be linked to schizophrenia (14, 16, 23, 30, 119, 120). The conditional model allowed us to establish the best-case treatment scenario by reinstating *Tcf4* to wildtype levels. Future proof-of-concept preclinical studies to upregulate *Tcf4* through ASOs or eventual genetic therapy approaches in PTHS model mice must take considerable care to recapitulate optimal levels of *Tcf4* expression. Third, my study does not guide appropriate isoforms to deliver to the brain through AAV-mediated genetic therapy. The *TCF4* gene produces at least 18 isoforms, some of which may be expressed in the brain at a given developmental stage (20). Characterizing isoform expression will be critical to guide design of the viral vector that has the proper isoform representation. Lastly, ICV injection may not be a feasible route in clinical setting due to invasiveness and limited clinical experience to date. IV has been used more often for clinical trials than ICV injection, thus may offer better administration option to mimic eventual AAV-mediated gene therapy. Given that my goal of the study is to test the feasibility of treating PTHS with postnatal genetic normalization, ICV injection was my primary choice as a route of delivery because it resulted in higher transduction efficiency in the forebrain than IV injection.

5.4 Methods and Materials

Study design

Wildtype females were crossed to $Tcf4^{STOP/+}$ males to generate wildtype and $Tcf4^{STOP/+}$ mice (PTHS model mice). Neonatal (P1-2) $Tcf4^{STOP/+}$ and $Tcf4^{+/+}$ mice were randomly assigned to treatment with vehicle or AAV9/PHP.eB-hSyn-Cre at a dose of 3.2×10^{10} vg delivered bilaterally to the cerebral ventricles. All injected mice performed

a battery of behavioral tests beginning 2 months of age, spanning a period of 6-7 weeks, in the following order: object location memory, open field, elevated plus maze, and nest building. All the treated mice underwent electrode implantation surgery 2 weeks after the last behavioral test and recovered from the surgery for at least 7 days. Mice with intact electrode headcap were subjected to LFP recording. LFP data were acquired for 3 days, 1 hour each day. Upon the completion of LFP recording, mice were sacrificed for ISH and qPCR analyses. Half a brain was used for ISH staining, and the other half was used for qPCR experiments. All investigators who conducted experiments and analyzed data were blinded to genotype and treatment until completion of the study.

Adeno-associated viral vector production

To produce AAV9/PHP.eB capsids, a PEI triple transfection protocol was first performed. Then the product was grown under serum-free conditions and purified through three rounds of CsCl density gradient centrifugation. Purified product was exchanged into storage buffer containing 1 x PBS, 5% D-Sorbitol, and 350mM NaCl. Virus titers (GC/ml) were determined by qPCR targeting the AAV ITRs. A codon-optimized *Cre* cDNA was packaged into AAV9/PHP.eB capsids.

AAV delivery

P1-2 mouse pups were cryo-anesthetized on ice for about 3 minutes, then transferred to a chilled stage equipped with a fiber optic light source for transillumination of the lateral ventricles. A 10 ml syringe fitted with a 32-gauge, 0.4-inch-long sterile

syringe needle (7803-04, Hamilton) was used to bilaterally deliver 0.5 ml of AAV9/PHP.eB-hSyn-Cre or vehicle (PBS supplemented with 5% D-Sorbitol and additional 212 mM NaCl) to the ventricles. The addition of Fast Green dye (1 mg/mL) to the virus solution visualized injection area. Following injection, pups were warmed on an isothermal heating pad with home-cage nesting material before being returned to the home cage.

Behavioral testing and analyses

Behavioral testing and analyses are described in Chapter 4 Methods and Material.

Surgery and *in vivo* LFP recording

Mice were anaesthetized by inhalation of 1-1.5% isoflurane (Piramal) in pure O_2 during surgery, with 0.25% bupivacaine injected under the scalp for local analgesia and meloxicam (10 mg/kg) subcutaneously administered. Stainless steel bipolar recording electrodes (P1 Technologies) were implanted in the hippocampus (coordinates from bregma: AP = -1.82 mm; ML= 1.5 mm; and DV = -1.2 mm), and ground electrodes were fastened to a stainless-steel screw positioned on the skull above the cerebellum. Dental cement was applied to secure electrode positions. Mice recovered for at least 7 days prior to LFP recording. A tethered system with a commutator (P1 Technologies) was used for recordings, while mice freely moved in their home cages. LFP recordings were amplified (1000x) using single-channel amplifiers (Grass Technologies), sampled at a

rate of 1000 Hz, and filtered at 0.3 Hz high-pass and 100 Hz low-pass filters. All electrical data were digitized with CED Micro1401 (Cambridge Electronic Design Ltd.).

LFP analysis

Data acquired in Spike2 software (Cambridge Electronic Design Ltd.) were read into Python and further processed with a bandpass filter from 1-100 Hz to focus on frequencies of my interest. Frequency bands were defined as delta 1-4 Hz, theta 5-8 Hz, beta 13-30 Hz, and gamma 30-50 Hz. Spectral power was analyzed using the Welch's Method (length of each segment: 2048, and number of points to overlap: 1024m), where the power spectral density is estimated by dividing the data into overlapping segments. Sample size ("n") represents the number of mice. For each mouse, I selected the longest continuous period with no movement artifacts for analysis. I averaged processed data obtained across three days. I wrote custom Python scripts to analyze LFP data.

Immunohistochemistry

Sections were rinsed several times with PBS (pH = 7.3) and PBS containing 0.2% Triton X-100 (PBST) before blocking with 5% normal goat serum in PBST (NGST) for 1 hour at room temperature. Sections were then incubated with primary antibodies diluted in NGST at 4°C for 48 hours. Sections were rinsed several times with PBST and then incubated with secondary antibodies for 1 hour at room temperature. In all experiments, 4',6-diamidino-2-phenylindole (DAPI; Invitrogen D1306) was added during the secondary antibody incubation at a concentration of 700 ng/ml. Primary antibodies

used included 1:1000 mouse anti-Cre (Millipore, MAB3120), 1:1000 guinea pig anti-NeuN (Millipore, ABN90P), and 1:1000 rabbit anti-GFAP (Dako, Z0334). The following secondary antibodies from Invitrogen (Carlsbad, CA) were used at 1:1000 dilution: goat anti-mouse Alexa 647 (A21240), goat anti-guinea pig Alexa 594 (A11076), and goat anti-rabbit Alexa 568 (A11011).

In situ hybridization

Brains were extracted and frozen in dry ice. Sections were taken at a thickness of 16 mm. Staining procedure was completed to manufacturer's specifications. RNAscope Fluorescent Multiplex Assay (Advanced Cell Diagnostics), designed to visualize multiple cellular RNA targets in fresh frozen tissues (110), was used to detect Cre (Cat No. 423321-C3) in mouse sections.

Imaging

Images of brain sections stained by using fluorophore-conjugated secondary antibodies were obtained with Zeiss LSM 710 Confocal Microscope, equipped with ZEN imaging software (Zeiss) and a Nikon Ti2 Eclipse Color and Widefield Microscope (Nikon). Images compared within the same figures were taken within the same imaging session using identical imaging parameters. Images within figure panels went through identical modification for brightness and contrast by using Fiji Image J software. Figures were prepared using Adobe Illustrator software (Adobe Systems).

RT-qPCR

The neocortical and hippocampal hemispheres were rapidly dissected, snap-frozen with dry ice-ethanol bath, and stored at -80°C. Total RNAs were extracted using the RNeasy Mini Kit (74106, Qiagen), and reverse transcribed via qScript cDNA SuperMix (101414-106, QuantaBio). The resulting cDNAs constituted the input, and RT-qPCR was performed in a QuantStudio Real-Time PCR system using SYBR green master mix (A25742, Thermofisher). The specificity of the amplification products was verified by melting curve analysis. All RT-qPCRs were conducted in technical triplicates, and the results were averaged for each sample, normalized to *Actin* expression, and analyzed using the comparative ΔΔCt method. The triplicates are valid only when the standard deviation is smaller than 0.25. The following primers were used in the RT-qPCRs: m*Tcf4* (forward: 5'-GGGAGGAAGAGAAGGTGT-3', reverse: 5'-CATCTGTCCCATGTGATTCGC-3'), *Grin2a* (forward: 5'-TTCATGATCCAGGAGGAGTTTG-3', reverse: 5'-AATCGGAAAGGCGGAGAATAG-3'), *Mal* (forward: 5'-CTGGCCACCATCTCAATGT-3', reverse: 5'-TGGACCACGTAGATCAGAGT-3'), *Glra3* (forward: 5'-GGGCATCACCACTGTACTTA-3', reverse: 5'-CCGCCATCCAAATGTCAATAG-3'), *Npy2r* (forward: 5'-GAAGTGAAAGTGGAGCCCTATG-3', reverse: 5'- ATCTTGCTCTCCAGGTGGTA-3'), *Npar1* (forward: 5'- CCCTCTACAGTGACTCCTACTT-3', reverse: 5'-GCCAAAGATGTGAGCGTAGA-3'), and *Actin* (forward: 5'-GGCACCACACCTTCTACAATG-3', reverse: 5'-GGGGTGTTGAAGGTCTCAAAC-3').

Statistical analysis

Welch's one-way ANOVA followed by Dunnett's *post hoc* test was performed for LFP power analysis and qPCR results (**Fig. 5.4**, **5.5**, and **5.6**). One-way ANOVA followed by Bonferroni's *post hoc* was carried out for body and brain weight, object location memory task, and open field (total distance) (**Fig. 5.3**). Two-way ANOVA followed by Tukey's *post hoc* was conducted for elevated plus maze, open field (distance for every 5-min), and nest building (material used). Nest building analysis to access % material used per day used two-way ANOVA followed by Bonferroni's *post hoc* (**Fig. 5.3**). In the figures, all values are expressed as means ± standard error of the mean (SEM). Asterisks indicate *P* values: **P* < 0.05, ***P* < 0.005, ****P* < 0.001, *****P* < 0.0001. GraphPad Prism 9.1.1 software was used for all statistical analyses.

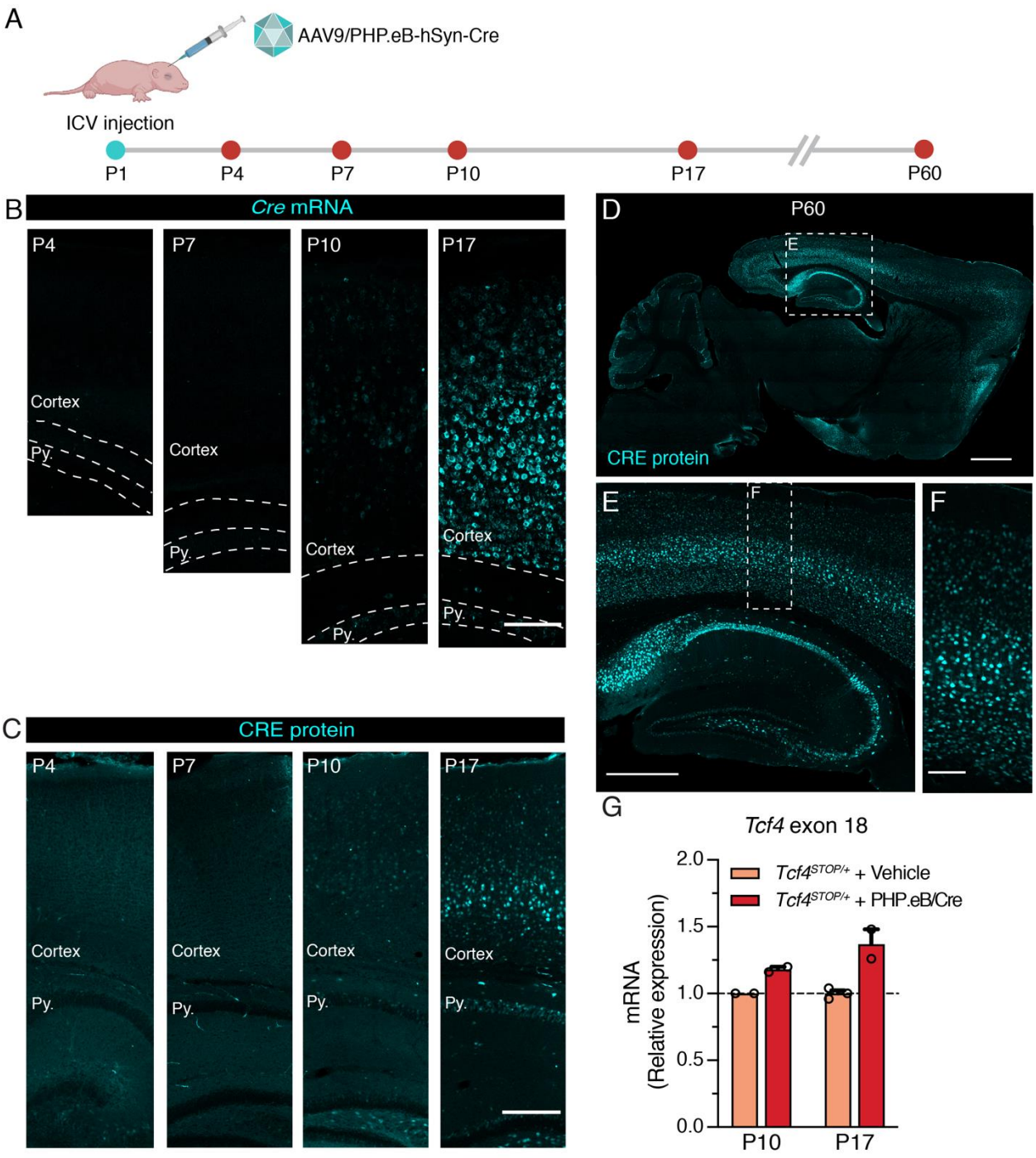

Figure 5. 1: Neonatal ICV delivery of PHP.eB/Cre yields Cre expression by approximately P10-P17.

(**A**) A timeline of experiment to evaluate timing of Cre biodistribution following ICV injection of 1 µl of 3.2 x 10^{13} vg/ml AAV9/PHP.eB-hSyn-Cre to P1 mice. (**B**) *In situ*

hybridization for *Cre* mRNA, and (**C**) immunofluorescence staining for CRE protein in the cortex and hippocampus of P4, P7, P10, and P17 wildtype mouse neonatally treated with PHP.eB/Cre. Py. = Stratum pyramidale. Scale bars = 100 µm (B) and 250 µm (C). (**D-F**) CRE immunofluorescence staining in sagittal section of a P60 wildtype mouse that had ICV injection of PHP.eB/Cre at P1. Scale bars = 1 mm (D), 500 mm (E), and 100 mm (F). (**G**) Relative *Tcf4* transcript levels detected in the brains of P10 and P17 $Tcf4^{STOP/+}$ mice treated with vehicle or PHP.eB/Cre.

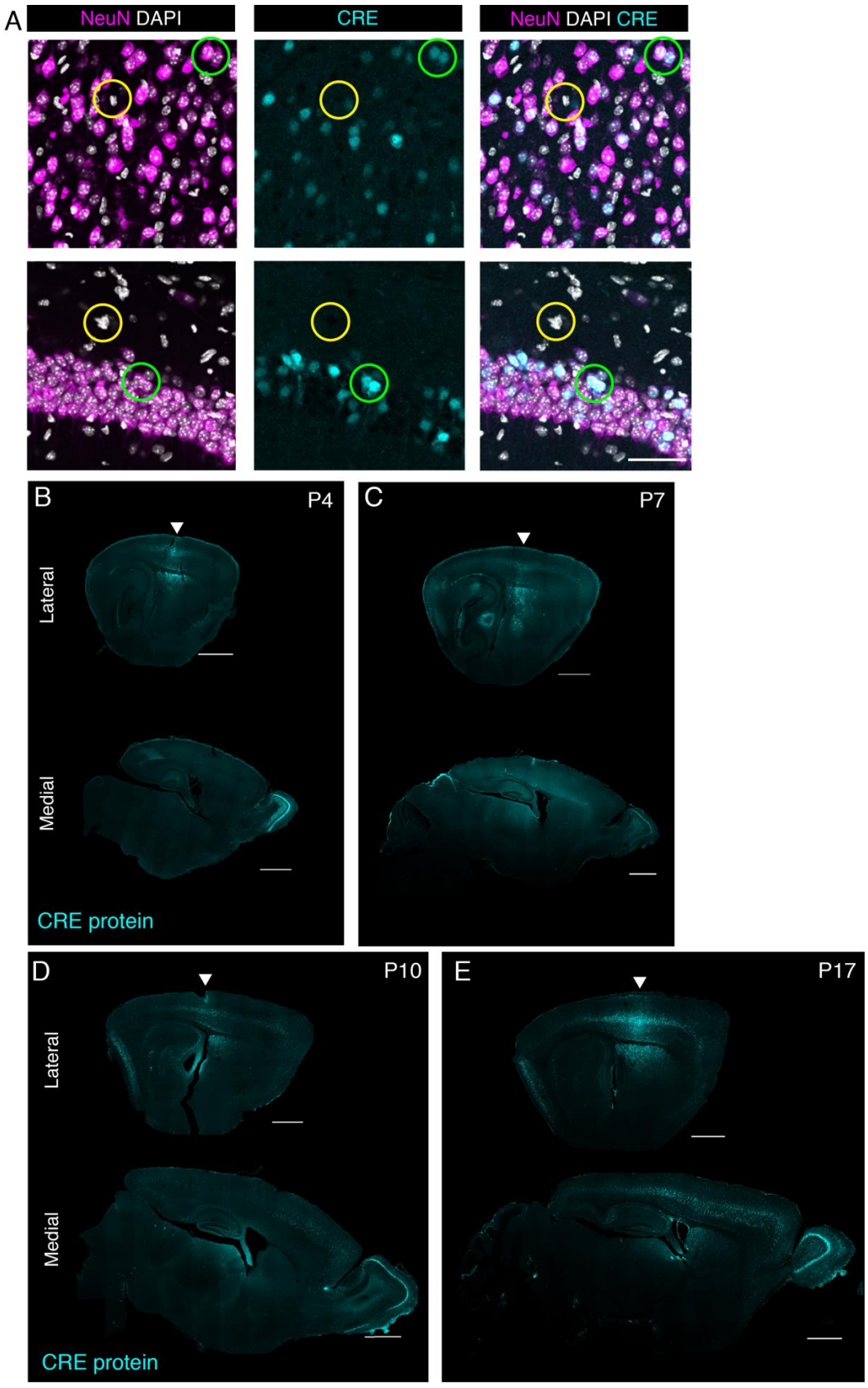
A
NeuN DAPI
CRE
NeuN DAPI CRE
B
P4
Lateral
Medial
CRE protein
C
P7
D
P10
Lateral
Medial
CRE protein
E
P17

Figure 5. 2: Cre immunofluorescence staining in sagittal sections of P4, P7, P10, and P17 mice.

(**A**) Dual immunostaining of NeuN and Cre in P17 brain of a mouse treated with PHP.eB/Cre. CRE protein was detected in NeuN-positive cells (green circle), but absent in NeuN-negative cells (yellow circle). Scale bars = 100 µm. (**B-E**) CRE protein spatial pattern in lateral (top row) and medial (bottom row) sagittal sections at different postnatal time points. Arrows indicate the brain area close to the injection site. Scale bars = 1 mm.

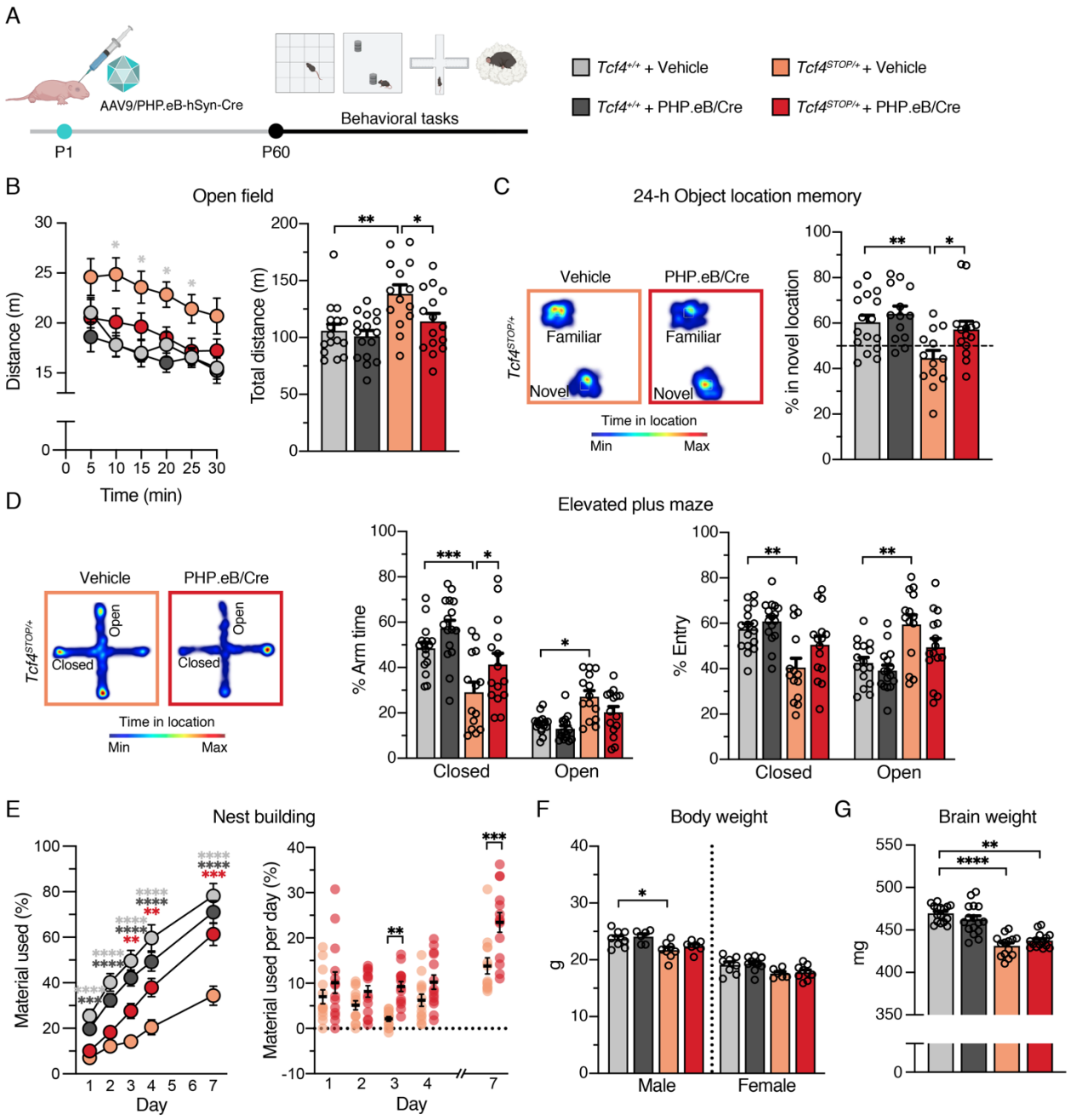

Figure 5. 3: Neonatal ICV injection of PHP.eB/Cre improves behavioral performance in *Tcf4*$^{STOP/+}$ mice.

(**A**) Experimental timeline for evaluation of behavioral phenotypes in *Tcf4*$^{+/+}$ and *Tcf4*$^{STOP/+}$ mice treated with vehicle or PHP.eB/Cre. (**B**) Left panel: Distance traveled per 5 min. Right panel: Total distance traveled for the 30-min testing period. (**C**) Left

panel: Heatmaps indicate time spent in proximity to one object located in the familiar position and the other object relocated to a novel position. Right panel: Percent time interacting with the novel location object. (**D**) Left panel: Heatmaps reveal time spent in elevated plus maze. Right panels: Percent time spent in the closed and open arms and percent entries made into the closed and open arms. (**E**) Left panel: Percentage of nest material used during the 7-day nest building period. Right panel: Percentage of nest material used per day (**F**) Body weight analysis of P65-69 male and female mice. (**G**) Adult brain weight analysis. The behavioral data were analyzed by one-way ANOVA followed by Bonferroni's *post hoc* or two-way ANOVA followed by Tukey's *post hoc* or Bonferroni's *post hoc*. Values are means ± SEM. *$p < 0.05$, **$p < 0.005$, ***$p < 0.001$, ****$p < 0.0001$.

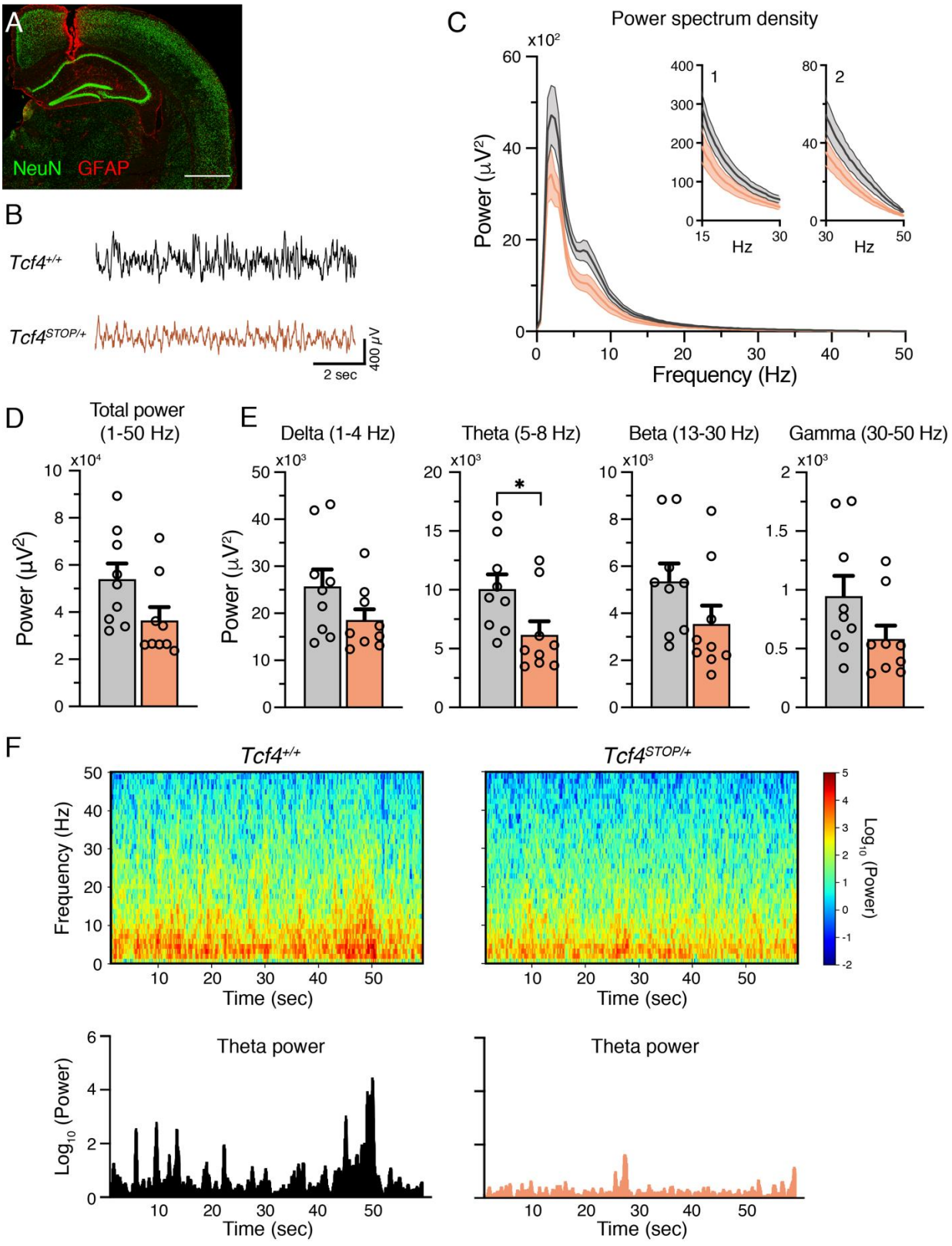

Figure 5. 4: *Tcf4* haploinsufficiency alters LFP spectral power in the theta band.

(**A**) Example electrode location (red, GFAP; green, NeuN). Scale bar = 100 mm. (**B**) Representative examples of LFP in *Tcf4*$^{+/+}$ and *Tcf4*$^{STOP/+}$ mice. (**C**) Power spectrum density of hippocampal LFP analyzed from *Tcf4*$^{+/+}$ and *Tcf4*$^{STOP/+}$ mice. Inset 1 spans from 15 to 30 Hz and inset 2 spans from 30 to 50 Hz on x-axis. (**D**) LFP power analyses of frequency bands ranging from 1 to 50 Hz, (**E**) delta (1-4 Hz), theta (5-8 Hz), beta (13-30 Hz), and gamma (30-50 Hz) bands. Unpaired t-test. (**F**) Top panel: Spectrograms in a single LFP session of representative experimental groups. Bottom panel: Representative theta power extracted from spectrogram in the top panel. Values are means ± SEM. *$p < 0.05$.

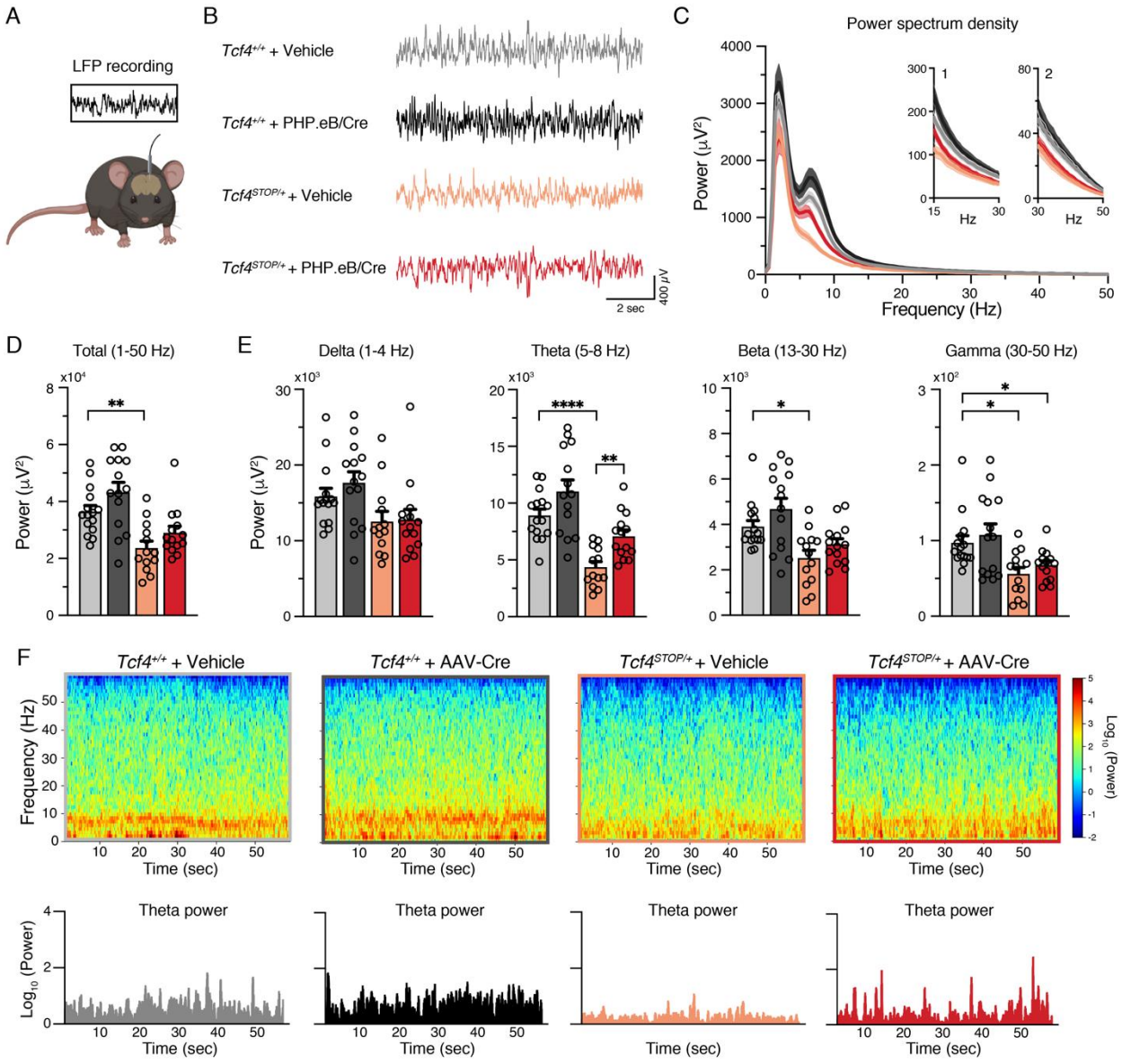

Figure 5. 5: Neonatal ICV injection of PHP.eB/Cre partially rescues LFP spectral power in *Tcf4*$^{STOP/+}$ mice.

(**A**) Schematic of LFP recording from the hippocampus of a freely moving mouse. (**B**) Representative examples of LFP in each experimental group. (**C**) Power spectrum density of hippocampal LFP analyzed from *Tcf4*$^{+/+}$ and *Tcf4*$^{STOP/+}$ mice treated with vehicle or PHP.eB/Cre. Inset 1 spans from 15 to 30 Hz and inset 2 spans from 30 to 50 Hz on x-axis. (**D**) LFP power analyses of frequency bands ranging from 1 to 50 Hz, (**E**)

delta (1-4 Hz), theta (5-8 Hz), beta (13-30 Hz), and gamma (30-50 Hz) bands. Welch's ANOVA followed by Dunnett's *post hoc*. (**F**) Top panel: Spectrograms in single LFP sessions of representative experimental groups. Bottom panel: Representative theta power extracted from spectrogram in the top panel. Values are means ± SEM. *p < 0.05, **p < 0.005, ****p < 0.0001.

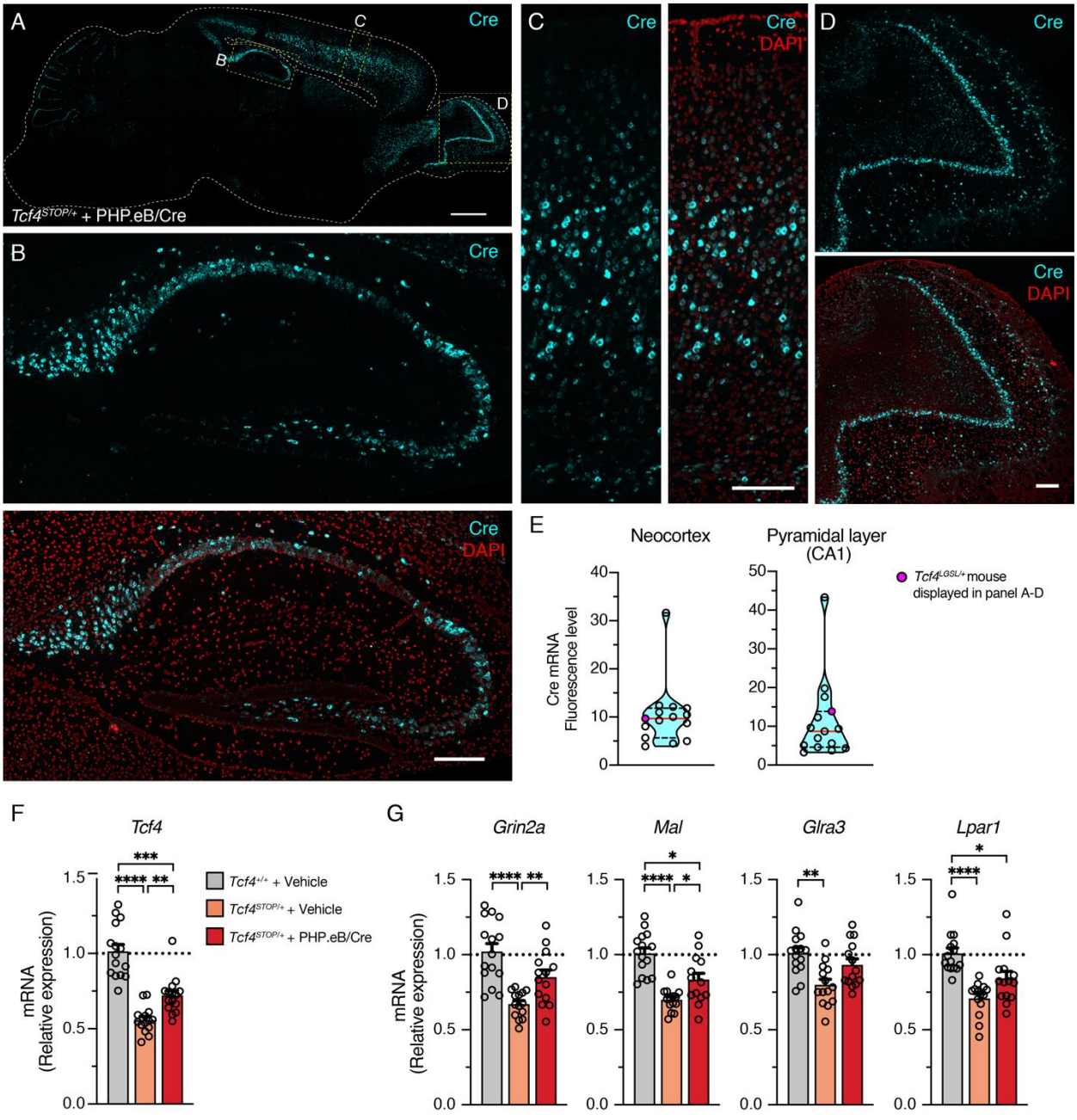

Figure 5. 6: Widespread *Cre* expression of the forebrain leads to partial upregulation of *Tcf4* and partial recovery of selected *Tcf4*-regulated gene expression.

(**A**)Representative image of ISH for *Cre* mRNA in sagittal section of six-month-old *Tcf4*$^{STOP/+}$ mouse that was treated at P1 with PHP.eB/Cre. Scale bar = 1 mm (**B-D**)

Higher magnification images of boxed regions in panel A. Scale bars = 200 mm. (**E**) *Cre* mRNA fluorescence levels of neocortex and CA1 pyramidal cell layer analyzed from individual *Tcf4*$^{STOP/+}$ + PHP.eB/Cre mice. The red line and black dotted lines of the violin plot represent median and interquartile ranges of the data, respectively. (**F**) Relative *Tcf4* mRNA expression of the forebrain from *Tcf4*$^{+/+}$ mice treated with vehicle and *Tcf4*$^{STOP/+}$ mice treated with vehicle and PHP.eB/Cre. *Tcf4* mRNA expression levels of PHP.eB/Cre treating *Tcf4*$^{STOP/+}$ mice are relatively higher than vehicle treating *Tcf4*$^{STOP/+}$ mice. (**G**) Relative mRNA expressions of selected *Tcf4*-regulated genes. Transcript levels of *Grin2a* (encoding for NMDA receptor subunit epsilon-1), *Mal* (encoding for myelin and lymphocyte protein), *Glra3* (encoding for glycine receptor subunit alpha-3), and *Lpar1* (lysophosphatidic acid receptor 1), which are known to be dysregulated by *Tcf4* haploinsufficiency, were partially rescued by *Tcf4* reinstatement. The data were analyzed by one-way ANOVA followed by Bonferroni's *post hoc*. Values are means ± SEM. ***$p < 0.001$, ****$p < 0.0001$.

CHAPTER 6: DISCUSSION

The genetic normalization approach offers a promising therapeutic intervention for PTHS because it directly overcomes the core genetic defect of PTHS. The idea underlying this approach is boosting TCF4 protein level to compensate for loss-of-function TCF4. The expression of hundreds of genes is dysregulated by the loss of TCF4. Therefore, in theory, normalizing TCF4 concentration should be able to adjust the dosage of *Tcf4*-regulated genes. To test the feasibility of treating PTHS by genetic therapy, I developed AAV9/*hTCF4* and delivered it to the brains of the *Tcf4* null mice. However, this gene transfer approach did not rescue behavioral phenotypes in PTHS model mice. Among several factors that might have contributed to negative results in my proof-of-concept study, I prioritized two key factors to improve future preclinical studies in genetic therapy for PTHS. First, I characterized the brain region and cell types that should be targeted by therapeutic agents such as AAV vectors or ASOs. Second, I defined the therapeutic window for behavioral recovery. My findings will inform the rational design of genetic normalization approaches such as gene therapy, ASOs and small molecule drugs.

6.1 The parameters to be optimized for genetic normalization strategies

6.1.1 AAV cassette and vector design for the AAV-mediated gene transfer therapy

Knowledge of the regional and cell type-specific expression of TCF4 guides the optimal design of the AAV cassette and vector. The AAV cassette consists of two inverted terminal repeats (ITRs), promoter, therapeutic transgene, and Poly(A) (71). ITRs can be modified so that the transgene is expressed without the need for second-strand DNA synthesis. This modified version of the ITRs, known as an scAAV vector, provides faster gene expression at a higher level than a conventional ssAAV vector, at the cost of reduced packaging capacity (72). scAAV vectors are an integral component of Zolgensma, which was recently approved by the FDA to treat spinal muscular atrophy (121), proving the clinical efficacy of scAAV. Therefore, future designs of the AAV cassette should consider using scAAV, notwithstanding packaging limitations arising from vector size.

Gene normalization strategies have the challenge of trying to avoid gene delivery to cells not normally expressing TCF4. Transgene expression is regulated by changing the promoter to provide either cell-specific or ubiquitous expression. My findings show that *Tcf4* is expressed in nearly all neurons, astrocytes, and oligodendrocytes, which should be targeted by the gene therapy approach. JeT is the synthetic promoter that ubiquitously drives moderate transgene expression, which is currently being used in a clinical trial of GAN gene transfer for giant axonal neuropathy (122). AAVs with some ubiquitous promoters such as CAG and CMV are reported to be toxic in mice (118), while no toxicity has not been reported with the JeT promoter (123), suggesting that the

JeT promoter could be used for an AAV cassette design. Alternatively, the hSyn promoter could be an option, as my work demonstrated that neuron-specific reinstatement of *Tcf4* was sufficient to prevent abnormal behavioral phenotypes in PTHS model mice.

My initial choice of the therapeutic transgene for the AAV-mediated *TCF4* gene therapy was human *TCF4B* because this isoform contains all functional domains (20). A Myc tag was added to its C-terminus so that I could reliably trace virally-delivered *hTCF4B* in recipient tissues. The particular concern for such design is the functionality of Myc-tagged TCF4B protein. It is possible that adding a tag to the C-terminus may interfere the normal activity of TCF4. Future designs of AAV vectors should not include C-terminus tags to avoid this possibility. Delivering appropriate isoforms to the brain is the key factor that contributes to the successful outcome of the gene therapy. My collaborator, Dr. Timmusk, has been characterizing isoform expression in human and mouse brains during postnatal development. His data show that developing human brains express *TCF4A*, *TCF4B*, and *TCFD* isoforms at a ratio of 3:1:1. TCF4A is one of the short isoforms that contains only AD2 and bHLH domain, and TCF4D is a midsize isoform that includes NLS, AD2, and bHLH domain. Similarly, mouse brains express *Tcf4A*, *Tcf4B*, and *Tcf4D*, but at a ratio of 1.7:1:1. Other isoforms such as *TCF4C*, *TCF4H*, and *TCF4I* are expressed, but at low levels (Timmusk's lab data). These observations suggest that TCF4A, TCF4B, and TCF4D isoform proteins should be delivered to the brain in an ideal gene therapy approach. Accordingly, considerable efforts should be made to focus on developing a codon-optimized transgene that expresses these isoforms at a near-endogenous ratio.

An AAV9 capsid provides the best vector spread and highest efficiency of transduction in the CNS, thus it became the popular choice for preclinical proof-of-concept experiments to target the CNS (122, 124, 125). AAV9 can penetrate the blood-brain barrier (BBB) following IV administration in neonatal mice, adult mice, cats, and nonhuman primates, but its transduction efficiency is significantly decreased following systemic administration in juvenile and adult mice (126, 127), which could be a challenge for preclinically testing the efficacy of AAV vectors in old mice. To overcome such issues, the AAV cassette can be packaged by AAV-PHP.B or AAV-PHP.eB capsids in order to efficiently transduce the CNS at a low dose (73). However, the ability of AAV-PHP.B or AAV-PHP.eB in penetrating the BBB is species-specific with the highest transduction rate in the C57BL/6J mice and a very low brain transduction in non-human primates (128). Considering the unsuitability of AAV-PHP.B or PHP.eB for clinical testing, the finalized AAV cassette should be packaged first within the AAV9 capsid to test it in neonates. If the TCF4 gene transfer approach needs to be validated in juvenile or adult mice, packaging the AAV cassette into AAV-PHP.B or AAV-PHP.eB capsids could be an option.

After finalizing the design of the AAV cassette, the critical step that must be performed prior to packaging it into the AAV9 capsid is validating the functionality of the AAV cassette containing *hTCF4* (AAV-hTCF4) through *in vitro* experiment. TCF4 promotes transcription through homodimerization or heterodimerization to other E-proteins, including ASCL1. This transcriptional activity can be measured by luciferase assays (20, 56), which requires the transfection of HEK293T cells with luciferase reporter constructs, which contain a promoter targeted by TCF4 and a luciferase

reporter, along with AAV-hTCF4, ASCL1, or AAV-hTCF4 combined with ASCL1 constructs. If AAV-hTCF4 constructs have the ability to activate transcription either alone or through heterodimerization with ASCL1, luciferase signals should be detected from transfected cells. Confirmation of the normal activity of AAV-hTCF4 in the luciferase assays will be an important step prior to *in vivo* experiments.

6.1.2 Routes of administration

Along with the AAV capsid and genome elements, the route of administration dictates levels and homogeneity of expression. Eventual ASO- or AAV-mediated genetic therapy will need to produce an appropriate biodistribution to be efficacious. *Tcf4* expression levels are particularly high in the forebrain (26). Accordingly, my *Tcf4* reinstatement study employed ICV administration to reinstate *Tcf4* expression more prominently in the forebrain than subcortical regions. Targeting *Tcf4* reinstatement to the forebrain recovered behavioral phenotypes in PTHS model mice, demonstrating that genetic delivery strategies that best recapitulate the expression patterns of TCF4 can provide therapeutic benefit. ICV route is a relatively straightforward administration method for neonates compared to juvenile and adult mice because the large volume of the lateral ventricles of newborn mice makes it easy to target for injection. In contrast, achieving widespread transduction through ICV administration to juvenile and adult mice might be more challenging than neonatal ICV administration. Therefore, alternative routes of administration such as systemic injection (e.g. retro-orbital or tail injection) could be optional for AAV delivery in juvenile and adult mice.

Delivery of ASOs for CNS disorders requires direct injection to the CNS, as these molecules do not readily cross the BBB. An intrathecal route of administration offers a relatively straightforward solution for bypassing the BBB and delivering drugs, viral vectors, or other therapeutic agents directly to the CNS. Use of this route has recently led to the successful development of the ASO drug, Spinraza, the first treatment to slow down neurodegeneration in spinal muscular atrophy (66). In human patients and in non-human primates, IT-delivered ASOs resulted in distribution favoring the forebrain (129), remarkably similar to the endogenous *Tcf4* expression pattern. Thus, ASO-based genetic therapy might have the potential to provide therapeutic benefit in PTHS. Future efforts will need to focus on identifying ASOs that promote generation of TCF4 protein.

6.1.3 Critical periods for the ability to rescue PTHS-relevant phenotypes

Successful treatment of PTHS will require an understanding of the optimal treatment window, as well as understanding the extent to which adult reinstatement provides therapeutic benefit. *Tcf4* reinstatement during early postnatal life prevented the emergence of PTHS phenotypes, indicating that genetic normalization approaches could provide a viable early life treatment opportunity. Late onset therapies may not exert as dramatic a phenotypic improvement compared to early intervention, yet partial improvement of some phenotypes in adults or prevention of disease progression would be significant achievements. To address the extent to which juvenile and adult *Tcf4* reinstatement correct behavioral phenotypes, the same viral vectors used for the neonatal *Tcf4* reinstatement study can be delivered to mice during the critical period (P21-P35) or in adulthood (P60). Because ICV injection is a challenging delivery route

for juvenile and adult mice, retro-orbital or tail injection should be optimized to achieve high transduction efficiency. My preliminary data show that retro-orbital injection of AAV9/PHP.eB-CAG-Cre to P33 mice can produce similar transduction efficiency as neonatal ICV injection and achieve broad Cre biodistribution throughout the mouse brain (**Fig. 6.1**), supporting that retro-orbital injection could be a promising route of delivery. If transduction efficiency is not consistent across mice, or toxicity is detected, reinstating *Tcf4* with tamoxifen in *Tcf4*$^{STOP/+}$*::CAG-CreERT* mice could be an alternative strategy.

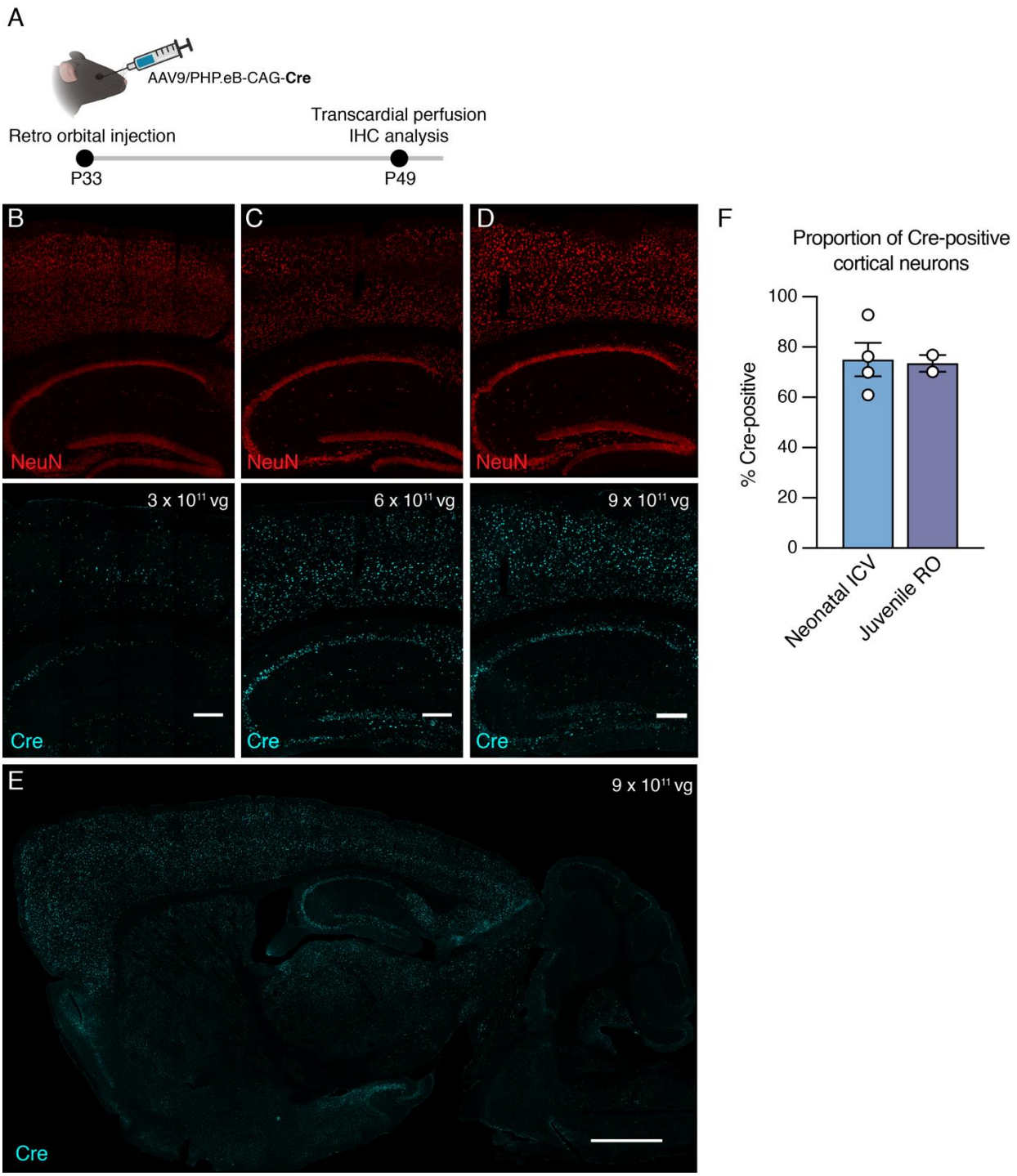

Figure 6. 1: Dose-dependent biodistribution of Cre following bilateral retro-orbital injection of PHP.eB/Cre to juvenile mice.

(**A**) Schematic of experiment to evaluate Cre biodistribution 16 days after bilateral retro-orbital injection of PHP.eB-CAG-Cre to P33 mice. (**B-D**) NeuN and Cre immunofluorescence staining in the cortex and hippocampus of the mice treated with PHP.eB/Cre at different doses: 10 µl of 3 x 10^{13} vg/ml for (**B**), 20 µl of 3 x 10^{13} vg/ml for (**C**), and 30 µl of 3 x 10^{13} vg/ml for (**D**). The number of Cre-expressing cells appears to be higher in the mice treated with 6 x 10^{11} vg and 9 x 10^{11} vg, compared to the mouse treated with 3 x 10^{11} vg. Scale bars = 200 µm. (**E**) Cre immunofluorescence staining in a sagittal brain section after injection with 9 x 10^{11} vg. Cre-expressing cells are evenly distributed across different brain regions. Scale bar = 1 mm. (**F**) Quantification of Cre-positive cortical neurons from mice ICV-injected as neonates (3 x 10^{10} vg) and mice RO (retro orbital)-injected as juveniles (6 x 10^{11} vg).

REFERENCES

1. Budday S, Steinmann P, and Kuhl E. Physical biology of human brain development. *Front Cell Neurosci.* 2015;9:257.

2. Merkle FT, and Alvarez-Buylla A. Neural stem cells in mammalian development. *Curr Opin Cell Biol.* 2006;18(6):704-9.

3. Bystron I, Blakemore C, and Rakic P. Development of the human cerebral cortex: Boulder Committee revisited. *Nat Rev Neurosci.* 2008;9(2):110-22.

4. Dennis DJ, Han S, and Schuurmans C. bHLH transcription factors in neural development, disease, and reprogramming. *Brain Res.* 2019;1705:48-65.

5. Bertrand N, Castro DS, and Guillemot F. Proneural genes and the specification of neural cell types. *Nat Rev Neurosci.* 2002;3(7):517-30.

6. Massari ME, and Murre C. Helix-loop-helix proteins: regulators of transcription in eucaryotic organisms. *Mol Cell Biol.* 2000;20(2):429-40.

7. Cho EA, and Dressler GR. TCF-4 binds beta-catenin and is expressed in distinct regions of the embryonic brain and limbs. *Mech Dev.* 1998;77(1):9-18.

8. de Pontual L, Mathieu Y, Golzio C, Rio M, Malan V, Boddaert N, et al. Mutational, functional, and expression studies of the TCF4 gene in Pitt-Hopkins syndrome. *Hum Mutat.* 2009;30(4):669-76.

9. Amiel J, Rio M, de Pontual L, Redon R, Malan V, Boddaert N, et al. Mutations in TCF4, encoding a class I basic helix-loop-helix transcription factor, are responsible for Pitt-Hopkins syndrome, a severe epileptic encephalopathy associated with autonomic dysfunction. *Am J Hum Genet.* 2007;80(5):988-93.

10. Zweier C, Peippo MM, Hoyer J, Sousa S, Bottani A, Clayton-Smith J, et al. Haploinsufficiency of TCF4 causes syndromal mental retardation with intermittent hyperventilation (Pitt-Hopkins syndrome). *Am J Hum Genet.* 2007;80(5):994-1001.

11. Hamdan FF, Daoud H, Patry L, Dionne-Laporte A, Spiegelman D, Dobrzeniecka S, et al. Parent-child exome sequencing identifies a de novo truncating mutation in TCF4 in non-syndromic intellectual disability. *Clin Genet.* 2013;83(2):198-200.

12. Maduro V, Pusey BN, Cherukuri PF, Atkins P, du Souich C, Rupps R, et al. Complex translocation disrupting TCF4 and altering TCF4 isoform expression segregates as mild autosomal dominant intellectual disability. *Orphanet J Rare Dis.* 2016;11(1):62.

13. Mary L, Piton A, Schaefer E, Mattioli F, Nourisson E, Feger C, et al. Disease-causing variants in TCF4 are a frequent cause of intellectual disability: lessons from large-scale sequencing approaches in diagnosis. *Eur J Hum Genet.* 2018;26(7):996-1006.

14. Brzozka MM, Radyushkin K, Wichert SP, Ehrenreich H, and Rossner MJ. Cognitive and sensorimotor gating impairments in transgenic mice overexpressing the schizophrenia susceptibility gene Tcf4 in the brain. *Biol Psychiatry.* 2010;68(1):33-40.

15. Quednow BB, Ettinger U, Mossner R, Rujescu D, Giegling I, Collier DA, et al. The schizophrenia risk allele C of the TCF4 rs9960767 polymorphism disrupts sensorimotor gating in schizophrenia spectrum and healthy volunteers. *J Neurosci.* 2011;31(18):6684-91.

16. Quednow BB, Brzozka MM, and Rossner MJ. Transcription factor 4 (TCF4) and schizophrenia: integrating the animal and the human perspective. *Cell Mol Life Sci.* 2014;71(15):2815-35.

17. Pickard BS, Malloy MP, Clark L, Lehellard S, Ewald HL, Mors O, et al. Candidate psychiatric illness genes identified in patients with pericentric inversions of chromosome 18. *Psychiatr Genet.* 2005;15(1):37-44.

18. Gelernter J, Sun N, Polimanti R, Pietrzak R, Levey DF, Bryois J, et al. Genome-wide association study of post-traumatic stress disorder reexperiencing symptoms in >165,000 US veterans. *Nat Neurosci.* 2019;22(9):1394-401.

19. Goodspeed K, Newsom C, Morris MA, Powell C, Evans P, and Golla S. Pitt-Hopkins Syndrome: A Review of Current Literature, Clinical Approach, and 23-Patient Case Series. *J Child Neurol.* 2018;33(3):233-44.

20. Sepp M, Kannike K, Eesmaa A, Urb M, and Timmusk T. Functional diversity of human basic helix-loop-helix transcription factor TCF4 isoforms generated by alternative 5' exon usage and splicing. *PLoS One.* 2011;6(7):e22138.

21. Persson P, Jogi A, Grynfeld A, Pahlman S, and Axelson H. HASH-1 and E2-2 are expressed in human neuroblastoma cells and form a functional complex. *Biochem Biophys Res Commun.* 2000;274(1):22-31.

22. Flora A, Garcia JJ, Thaller C, and Zoghbi HY. The E-protein Tcf4 interacts with Math1 to regulate differentiation of a specific subset of neuronal progenitors. *Proc Natl Acad Sci U S A.* 2007;104(39):15382-7.

23. Forrest M, Chapman RM, Doyle AM, Tinsley CL, Waite A, and Blake DJ. Functional analysis of TCF4 missense mutations that cause Pitt-Hopkins syndrome. *Hum Mutat.* 2012;33(12):1676-86.

24. Chen T, Wu Q, Zhang Y, Lu T, Yue W, and Zhang D. Tcf4 Controls Neuronal Migration of the Cerebral Cortex through Regulation of Bmp7. *Front Mol Neurosci.* 2016;9:94.

25. Jung M, Haberle BM, Tschaikowsky T, Wittmann MT, Balta EA, Stadler VC, et al. Analysis of the expression pattern of the schizophrenia-risk and intellectual disability gene TCF4 in the developing and adult brain suggests a role in development and plasticity of cortical and hippocampal neurons. *Mol Autism.* 2018;9:20.

26. Kim H, Berens NC, Ochandarena NE, and Philpot BD. Region and Cell Type Distribution of TCF4 in the Postnatal Mouse Brain. *Front Neuroanat.* 2020;14:42.

27. Fu H, Cai J, Clevers H, Fast E, Gray S, Greenberg R, et al. A genome-wide screen for spatially restricted expression patterns identifies transcription factors that regulate glial development. *J Neurosci.* 2009;29(36):11399-408.

28. Rannals MD, Hamersky GR, Page SC, Campbell MN, Briley A, Gallo RA, et al. Psychiatric Risk Gene Transcription Factor 4 Regulates Intrinsic Excitability of Prefrontal Neurons via Repression of SCN10a and KCNQ1. *Neuron.* 2016;90(1):43-55.

29. Phan BN, Bohlen JF, Davis BA, Ye Z, Chen HY, Mayfield B, et al. A myelin-related transcriptomic profile is shared by Pitt-Hopkins syndrome models and human autism spectrum disorder. *Nat Neurosci.* 2020.

30. Sepp M, Pruunsild P, and Timmusk T. Pitt-Hopkins syndrome-associated mutations in TCF4 lead to variable impairment of the transcription factor function ranging from hypomorphic to dominant-negative effects. *Hum Mol Genet.* 2012;21(13):2873-88.

31. Shively CA, Liu J, Chen X, Loell K, and Mitra RD. Homotypic cooperativity and collective binding are determinants of bHLH specificity and function. *Proc Natl Acad Sci U S A.* 2019;116(32):16143-52.

32. Corneliussen B, Holm M, Waltersson Y, Onions J, Hallberg B, Thornell A, et al. Calcium/calmodulin inhibition of basic-helix-loop-helix transcription factor domains. *Nature.* 1994;368(6473):760-4.

33. Forrest MP, Hill MJ, Kavanagh DH, Tansey KE, Waite AJ, and Blake DJ. The Psychiatric Risk Gene Transcription Factor 4 (TCF4) Regulates Neurodevelopmental Pathways Associated With Schizophrenia, Autism, and Intellectual Disability. *Schizophr Bull.* 2018;44(5):1100-10.

34. Xia H, Jahr FM, Kim NK, Xie L, Shabalin AA, Bryois J, et al. Building a schizophrenia genetic network: transcription factor 4 regulates genes involved in neuronal development and schizophrenia risk. *Hum Mol Genet.* 2018;27(18):3246-56.

35. Forrest MP, Waite AJ, Martin-Rendon E, and Blake DJ. Knockdown of human TCF4 affects multiple signaling pathways involved in cell survival, epithelial to mesenchymal transition and neuronal differentiation. *PLoS One.* 2013;8(8):e73169.

36. Chen ES, Gigek CO, Rosenfeld JA, Diallo AB, Maussion G, Chen GG, et al. Molecular convergence of neurodevelopmental disorders. *Am J Hum Genet.* 2014;95(5):490-508.

37. Hill MJ, Killick R, Navarrete K, Maruszak A, McLaughlin GM, Williams BP, et al. Knockdown of the schizophrenia susceptibility gene TCF4 alters gene expression and proliferation of progenitor cells from the developing human neocortex. *J Psychiatry Neurosci.* 2017;42(3):181-8.

38. Doostparast Torshizi A, Armoskus C, Zhang H, Forrest MP, Zhang S, Souaiaia T, et al. Deconvolution of transcriptional networks identifies TCF4 as a master regulator in schizophrenia. *Sci Adv.* 2019;5(9):eaau4139.

39. Rakic P. Specification of cerebral cortical areas. *Science.* 1988;241(4862):170-6.

40. Rakic P, Ayoub AE, Breunig JJ, and Dominguez MH. Decision by division: making cortical maps. *Trends Neurosci.* 2009;32(5):291-301.

41. Li H, Zhu Y, Morozov YM, Chen X, Page SC, Rannals MD, et al. Disruption of TCF4 regulatory networks leads to abnormal cortical development and mental disabilities. *Mol Psychiatry.* 2019.

42. Page SC, Hamersky GR, Gallo RA, Rannals MD, Calcaterra NE, Campbell MN, et al. The schizophrenia- and autism-associated gene, transcription factor 4 regulates the columnar distribution of layer 2/3 prefrontal pyramidal neurons in an activity-dependent manner. *Mol Psychiatry.* 2018;23(2):304-15.

43. Crux S, Herms J, and Dorostkar MM. Tcf4 regulates dendritic spine density and morphology in the adult brain. *PLoS One.* 2018;13(6):e0199359.

44. Wang Y, Lu Z, Zhang Y, Cai Y, Yun D, Tang T, et al. Transcription Factor 4 Safeguards Hippocampal Dentate Gyrus Development by Regulating Neural Progenitor Migration. *Cereb Cortex.* 2020;30(5):3102-15.

45. Zollino M, Zweier C, Van Balkom ID, Sweetser DA, Alaimo J, Bijlsma EK, et al. Diagnosis and management in Pitt-Hopkins syndrome: First international consensus statement. *Clin Genet.* 2019.

46. Peippo MM, Simola KO, Valanne LK, Larsen AT, Kahkonen M, Auranen MP, et al. Pitt-Hopkins syndrome in two patients and further definition of the phenotype. *Clin Dysmorphol.* 2006;15(2):47-54.

47. Whalen S, Heron D, Gaillon T, Moldovan O, Rossi M, Devillard F, et al. Novel comprehensive diagnostic strategy in Pitt-Hopkins syndrome: clinical score and further delineation of the TCF4 mutational spectrum. *Hum Mutat.* 2012;33(1):64-72.

48. Giurgea I, Missirian C, Cacciagli P, Whalen S, Fredriksen T, Gaillon T, et al. TCF4 deletions in Pitt-Hopkins Syndrome. *Hum Mutat.* 2008;29(11):E242-51.

49. Kharbanda M, Kannike K, Lampe A, Berg J, Timmusk T, and Sepp M. Partial deletion of TCF4 in three generation family with non-syndromic intellectual disability, without features of Pitt-Hopkins syndrome. *Eur J Med Genet.* 2016;59(6-7):310-4.

50. Bedeschi MF, Marangi G, Calvello MR, Ricciardi S, Leone FPC, Baccarin M, et al. Impairment of different protein domains causes variable clinical presentation within Pitt-Hopkins syndrome and suggests intragenic molecular syndromology of TCF4. *Eur J Med Genet.* 2017;60(11):565-71.

51. Mailman RB, and Murthy V. Third generation antipsychotic drugs: partial agonism or receptor functional selectivity? *Curr Pharm Des.* 2010;16(5):488-501.

52. Lambrechts S, Devriendt K, and Vogels A. Low-Dose Aripiprazole and Risperidone for Treating Problem Behavior in Children With Pitt-Hopkins Syndrome. *J Clin Psychopharmacol.* 2018;38(3):260-1.

53. de Winter CF, Baas M, Bijlsma EK, van Heukelingen J, Routledge S, and Hennekam RC. Phenotype and natural history in 101 individuals with Pitt-Hopkins syndrome through an internet questionnaire system. *Orphanet J Rare Dis.* 2016;11:37.

54. Kennedy AJ, Rahn EJ, Paulukaitis BS, Savell KE, Kordasiewicz HB, Wang J, et al. Tcf4 Regulates Synaptic Plasticity, DNA Methylation, and Memory Function. *Cell Rep.* 2016;16(10):2666-85.

55. Zhuang Y, Cheng P, and Weintraub H. B-lymphocyte development is regulated by the combined dosage of three basic helix-loop-helix genes, E2A, E2-2, and HEB. *Mol Cell Biol.* 1996;16(6):2898-905.

56. Thaxton C, Kloth AD, Clark EP, Moy SS, Chitwood RA, and Philpot BD. Common Pathophysiology in Multiple Mouse Models of Pitt-Hopkins Syndrome. *J Neurosci.* 2018;38(4):918-36.

57. Kullmann DM. Amplitude fluctuations of dual-component EPSCs in hippocampal pyramidal cells: implications for long-term potentiation. *Neuron.* 1994;12(5):1111-20.

58. Gu Y, McIlwain KL, Weeber EJ, Yamagata T, Xu B, Antalffy BA, et al. Impaired conditioned fear and enhanced long-term potentiation in Fmr2 knock-out mice. *J Neurosci.* 2002;22(7):2753-63.

59. Meng Y, Zhang Y, Tregoubov V, Janus C, Cruz L, Jackson M, et al. Abnormal spine morphology and enhanced LTP in LIMK-1 knockout mice. *Neuron.* 2002;35(1):121-33.

60. Migaud M, Charlesworth P, Dempster M, Webster LC, Watabe AM, Makhinson M, et al. Enhanced long-term potentiation and impaired learning in mice with mutant postsynaptic density-95 protein. *Nature.* 1998;396(6710):433-9.

61. Graff J, Joseph NF, Horn ME, Samiei A, Meng J, Seo J, et al. Epigenetic priming of memory updating during reconsolidation to attenuate remote fear memories. *Cell.* 2014;156(1-2):261-76.

62. Gryder BE, Sodji QH, and Oyelere AK. Targeted cancer therapy: giving histone deacetylase inhibitors all they need to succeed. *Future Med Chem.* 2012;4(4):505-24.

63. Ekins S, Puhl AC, and Davidow A. Repurposing the Dihydropyridine Calcium Channel Inhibitor Nicardipine as a Nav1.8 Inhibitor In Vivo for Pitt Hopkins Syndrome. *Pharm Res.* 2020;37(7):127.

64. Silva-Santos S, van Woerden GM, Bruinsma CF, Mientjes E, Jolfaei MA, Distel B, et al. Ube3a reinstatement identifies distinct developmental windows in a murine Angelman syndrome model. *J Clin Invest.* 2015;125(5):2069-76.

65. Guy J, Gan J, Selfridge J, Cobb S, and Bird A. Reversal of neurological defects in a mouse model of Rett syndrome. *Science.* 2007;315(5815):1143-7.

66. Wurster CD, Winter B, Wollinsky K, Ludolph AC, Uzelac Z, Witzel S, et al. Intrathecal administration of nusinersen in adolescent and adult SMA type 2 and 3 patients. *J Neurol.* 2019;266(1):183-94.

67. Wang D, Tai PWL, and Gao G. Adeno-associated virus vector as a platform for gene therapy delivery. *Nat Rev Drug Discov.* 2019;18(5):358-78.

68. Deverman BE, Ravina BM, Bankiewicz KS, Paul SM, and Sah DWY. Gene therapy for neurological disorders: progress and prospects. *Nat Rev Drug Discov.* 2018;17(10):767.

69. Hoy SM. Onasemnogene Abeparvovec: First Global Approval. *Drugs.* 2019;79(11):1255-62.

70. Goncalves MA. Adeno-associated virus: from defective virus to effective vector. *Virol J.* 2005;2:43.

71. Li C, and Samulski RJ. Engineering adeno-associated virus vectors for gene therapy. *Nat Rev Genet.* 2020;21(4):255-72.

72. McCarty DM, Fu H, Monahan PE, Toulson CE, Naik P, and Samulski RJ. Adeno-associated virus terminal repeat (TR) mutant generates self-complementary vectors to overcome the rate-limiting step to transduction in vivo. *Gene Ther.* 2003;10(26):2112-8.

73. Chan KY, Jang MJ, Yoo BB, Greenbaum A, Ravi N, Wu WL, et al. Engineered AAVs for efficient noninvasive gene delivery to the central and peripheral nervous systems. *Nat Neurosci.* 2017;20(8):1172-9.

74. Simonato M, Bennett J, Boulis NM, Castro MG, Fink DJ, Goins WF, et al. Progress in gene therapy for neurological disorders. *Nat Rev Neurol.* 2013;9(5):277-91.

75. Gray SJ, Nagabhushan Kalburgi S, McCown TJ, and Jude Samulski R. Global CNS gene delivery and evasion of anti-AAV-neutralizing antibodies by intrathecal AAV administration in non-human primates. *Gene Ther.* 2013;20(4):450-9.

76. Arsenault J, Gholizadeh S, Niibori Y, Pacey LK, Halder SK, Koxhioni E, et al. FMRP Expression Levels in Mouse Central Nervous System Neurons Determine Behavioral Phenotype. *Hum Gene Ther.* 2016;27(12):982-96.

77. Gadalla KK, Bailey ME, Spike RC, Ross PD, Woodard KT, Kalburgi SN, et al. Improved survival and reduced phenotypic severity following AAV9/MECP2 gene transfer to neonatal and juvenile male Mecp2 knockout mice. *Mol Ther.* 2013;21(1):18-30.

78. Sinnett SE, Hector RD, Gadalla KKE, Heindel C, Chen D, Zaric V, et al. Improved MECP2 Gene Therapy Extends the Survival of MeCP2-Null Mice without Apparent Toxicity after Intracisternal Delivery. *Mol Ther Methods Clin Dev.* 2017;5:106-15.

79. Jacobs EC, Campagnoni C, Kampf K, Reyes SD, Kalra V, Handley V, et al. Visualization of corticofugal projections during early cortical development in a tau-GFP-transgenic mouse. *Eur J Neurosci.* 2007;25(1):17-30.

80. Taniguchi H, He M, Wu P, Kim S, Paik R, Sugino K, et al. A resource of Cre driver lines for genetic targeting of GABAergic neurons in cerebral cortex. *Neuron.* 2011;71(6):995-1013.

81. Goebbels S, Bormuth I, Bode U, Hermanson O, Schwab MH, and Nave KA. Genetic targeting of principal neurons in neocortex and hippocampus of NEX-Cre mice. *Genesis.* 2006;44(12):611-21.

82. Rudy B, Fishell G, Lee S, and Hjerling-Leffler J. Three groups of interneurons account for nearly 100% of neocortical GABAergic neurons. *Dev Neurobiol.* 2011;71(1):45-61.

83. DeFelipe J. Neocortical neuronal diversity: chemical heterogeneity revealed by colocalization studies of classic neurotransmitters, neuropeptides, calcium-binding proteins, and cell surface molecules. *Cereb Cortex.* 1993;3(4):273-89.

84. Gonchar Y, and Burkhalter A. Three distinct families of GABAergic neurons in rat visual cortex. *Cereb Cortex.* 1997;7(4):347-58.

85. Markram H, Toledo-Rodriguez M, Wang Y, Gupta A, Silberberg G, and Wu C. Interneurons of the neocortical inhibitory system. *Nat Rev Neurosci.* 2004;5(10):793-807.

86. Lee S, Hjerling-Leffler J, Zagha E, Fishell G, and Rudy B. The largest group of superficial neocortical GABAergic interneurons expresses ionotropic serotonin receptors. *J Neurosci.* 2010;30(50):16796-808.

87. Bhat RV, Axt KJ, Fosnaugh JS, Smith KJ, Johnson KA, Hill DE, et al. Expression of the APC tumor suppressor protein in oligodendroglia. *Glia.* 1996;17(2):169-74.

88. Pelkey KA, Chittajallu R, Craig MT, Tricoire L, Wester JC, and McBain CJ. Hippocampal GABAergic Inhibitory Interneurons. *Physiol Rev.* 2017;97(4):1619-747.

89. Koos T, and Tepper JM. Inhibitory control of neostriatal projection neurons by GABAergic interneurons. *Nat Neurosci.* 1999;2(5):467-72.

90. Gittis AH, Nelson AB, Thwin MT, Palop JJ, and Kreitzer AC. Distinct roles of GABAergic interneurons in the regulation of striatal output pathways. *J Neurosci.* 2010;30(6):2223-34.

91. Munoz-Manchado AB, Bengtsson Gonzales C, Zeisel A, Munguba H, Bekkouche B, Skene NG, et al. Diversity of Interneurons in the Dorsal Striatum Revealed by Single-Cell RNA Sequencing and PatchSeq. *Cell Rep.* 2018;24(8):2179-90 e7.

92. Altman J. Autoradiographic and histological studies of postnatal neurogenesis. IV. Cell proliferation and migration in the anterior forebrain, with special reference to persisting neurogenesis in the olfactory bulb. *J Comp Neurol.* 1969;137(4):433-57.

93. Basmanav FB, Forstner AJ, Fier H, Herms S, Meier S, Degenhardt F, et al. Investigation of the role of TCF4 rare sequence variants in schizophrenia. *Am J Med Genet B Neuropsychiatr Genet.* 2015;168B(5):354-62.

94. Miller EK. The prefrontal cortex and cognitive control. *Nat Rev Neurosci.* 2000;1(1):59-65.

95. Rubin RD, Watson PD, Duff MC, and Cohen NJ. The role of the hippocampus in flexible cognition and social behavior. *Front Hum Neurosci.* 2014;8:742.

96. Dupret D, O'Neill J, Pleydell-Bouverie B, and Csicsvari J. The reorganization and reactivation of hippocampal maps predict spatial memory performance. *Nat Neurosci.* 2010;13(8):995-1002.

97. Kreitzer AC, and Malenka RC. Striatal plasticity and basal ganglia circuit function. *Neuron.* 2008;60(4):543-54.

98. Straub C, Saulnier JL, Begue A, Feng DD, Huang KW, and Sabatini BL. Principles of Synaptic Organization of GABAergic Interneurons in the Striatum. *Neuron.* 2016;92(1):84-92.

99. Skene NG, Bryois J, Bakken TE, Breen G, Crowley JJ, Gaspar HA, et al. Genetic identification of brain cell types underlying schizophrenia. *Nat Genet.* 2018;50(6):825-33.

100. Rapanelli M, Frick LR, and Pittenger C. The Role of Interneurons in Autism and Tourette Syndrome. *Trends Neurosci.* 2017;40(7):397-407.

101. Maia TV, and Frank MJ. From reinforcement learning models to psychiatric and neurological disorders. *Nat Neurosci.* 2011;14(2):154-62.

102. Schmahmann JD, and Caplan D. Cognition, emotion and the cerebellum. *Brain.* 2006;129(Pt 2):290-2.

103. Rogers TD, McKimm E, Dickson PE, Goldowitz D, Blaha CD, and Mittleman G. Is autism a disease of the cerebellum? An integration of clinical and pre-clinical research. *Front Syst Neurosci.* 2013;7:15.

104. Steinlin M. Cerebellar disorders in childhood: cognitive problems. *Cerebellum.* 2008;7(4):607-10.

105. Bolduc ME, du Plessis AJ, Sullivan N, Guizard N, Zhang X, Robertson RL, et al. Regional cerebellar volumes predict functional outcome in children with cerebellar malformations. *Cerebellum.* 2012;11(2):531-42.

106. Abelson JF, Kwan KY, O'Roak BJ, Baek DY, Stillman AA, Morgan TM, et al. Sequence variants in SLITRK1 are associated with Tourette's syndrome. *Science.* 2005;310(5746):317-20.

107. Matsuda T, and Cepko CL. Controlled expression of transgenes introduced by in vivo electroporation. *Proc Natl Acad Sci U S A.* 2007;104(3):1027-32.

108. Mortazavi A, Williams BA, McCue K, Schaeffer L, and Wold B. Mapping and quantifying mammalian transcriptomes by RNA-Seq. *Nat Methods.* 2008;5(7):621-8.

109. Chen B, Schaevitz LR, and McConnell SK. Fezl regulates the differentiation and axon targeting of layer 5 subcortical projection neurons in cerebral cortex. *Proc Natl Acad Sci U S A.* 2005;102(47):17184-9.

110. Wang F, Flanagan J, Su N, Wang LC, Bui S, Nielson A, et al. RNAscope: a novel in situ RNA analysis platform for formalin-fixed, paraffin-embedded tissues. *J Mol Diagn.* 2012;14(1):22-9.

111. Kamentsky L, Jones TR, Fraser A, Bray MA, Logan DJ, Madden KL, et al. Improved structure, function and compatibility for CellProfiler: modular high-throughput image analysis software. *Bioinformatics.* 2011;27(8):1179-80.

112. Loo L, Simon JM, Xing L, McCoy ES, Niehaus JK, Guo J, et al. Single-cell transcriptomic analysis of mouse neocortical development. *Nat Commun.* 2019;10(1):134.

113. Zeisel A, Munoz-Manchado AB, Codeluppi S, Lonnerberg P, La Manno G, Jureus A, et al. Brain structure. Cell types in the mouse cortex and hippocampus revealed by single-cell RNA-seq. *Science.* 2015;347(6226):1138-42.

114. Deacon RM. Assessing nest building in mice. *Nat Protoc.* 2006;1(3):1117-9.

115. Takano K, Lyons M, Moyes C, Jones J, and Schwartz CE. Two percent of patients suspected of having Angelman syndrome have TCF4 mutations. *Clin Genet.* 2010;78(3):282-8.

116. Buzsaki G, Anastassiou CA, and Koch C. The origin of extracellular fields and currents--EEG, ECoG, LFP and spikes. *Nat Rev Neurosci.* 2012;13(6):407-20.

117. Wang S, Lai X, Deng Y, and Song Y. Correlation between mouse age and human age in anti-tumor research: Significance and method establishment. *Life Sci.* 2020;242:117242.

118. Xiong W, Wu DM, Xue Y, Wang SK, Chung MJ, Ji X, et al. AAV cis-regulatory sequences are correlated with ocular toxicity. *Proc Natl Acad Sci U S A.* 2019;116(12):5785-94.

119. Brennand KJ, Simone A, Jou J, Gelboin-Burkhart C, Tran N, Sangar S, et al. Modelling schizophrenia using human induced pluripotent stem cells. *Nature.* 2011;473(7346):221-5.

120. Wirgenes KV, Sonderby IE, Haukvik UK, Mattingsdal M, Tesli M, Athanasiu L, et al. TCF4 sequence variants and mRNA levels are associated with neurodevelopmental characteristics in psychotic disorders. *Transl Psychiatry.* 2012;2:e112.

121. Mendell JR, Al-Zaidy S, Shell R, Arnold WD, Rodino-Klapac LR, Prior TW, et al. Single-Dose Gene-Replacement Therapy for Spinal Muscular Atrophy. *N Engl J Med.* 2017;377(18):1713-22.

122. Bailey RM, Armao D, Nagabhushan Kalburgi S, and Gray SJ. Development of Intrathecal AAV9 Gene Therapy for Giant Axonal Neuropathy. *Mol Ther Methods Clin Dev.* 2018;9:160-71.

123. Tornoe J, Kusk P, Johansen TE, and Jensen PR. Generation of a synthetic mammalian promoter library by modification of sequences spacing transcription factor binding sites. *Gene.* 2002;297(1-2):21-32.

124. Gray SJ, Matagne V, Bachaboina L, Yadav S, Ojeda SR, and Samulski RJ. Preclinical differences of intravascular AAV9 delivery to neurons and glia: a comparative study of adult mice and nonhuman primates. *Mol Ther.* 2011;19(6):1058-69.

125. Ruzo A, Marco S, Garcia M, Villacampa P, Ribera A, Ayuso E, et al. Correction of pathological accumulation of glycosaminoglycans in central nervous system and peripheral tissues of MPSIIIA mice through systemic AAV9 gene transfer. *Hum Gene Ther.* 2012;23(12):1237-46.

126. Duque S, Joussemet B, Riviere C, Marais T, Dubreil L, Douar AM, et al. Intravenous administration of self-complementary AAV9 enables transgene delivery to adult motor neurons. *Mol Ther.* 2009;17(7):1187-96.

127. Foust KD, Nurre E, Montgomery CL, Hernandez A, Chan CM, and Kaspar BK. Intravascular AAV9 preferentially targets neonatal neurons and adult astrocytes. *Nat Biotechnol.* 2009;27(1):59-65.

128. Liguore WA, Domire JS, Button D, Wang Y, Dufour BD, Srinivasan S, et al. AAV-PHP.B Administration Results in a Differential Pattern of CNS Biodistribution in Non-human Primates Compared with Mice. *Mol Ther.* 2019;27(11):2018-37.

129. Mazur C, Powers B, Zasadny K, Sullivan JM, Dimant H, Kamme F, et al. Brain pharmacology of intrathecal antisense oligonucleotides revealed through multimodal imaging. *JCI Insight.* 2019;4(20).